Electromagnetic Signatures of Supermassive Black Hole Binaries

by

Kevin Whitley

A dissertation submitted in partial fulfillment
of the requirements for the degree of
Doctor of Philosophy
(Astronomy and Astrophysics)
in The University of Michigan
2024

Doctoral Committee:

Assistant Professor Kayhan Gültekin, Co-Chair
Professor Mateusz Ruszkowski, Co-Chair
Professor Fred Adams
Professor Philip Armitage, Stony Brook University
Professor Emeritus Lee Hartmann

Kevin Whitley

kwhitle@umich.edu

ORCID iD: 0000-0001-9379-6519

© Kevin Whitley 2024

For my friends — who made the journey worthwhile.

ACKNOWLEDGEMENTS

Earning a PhD has been, perhaps, the most challenging thing I've ever done. There have been many serious hurdles along the way and I could not have overcome them without the guidance, camaraderie, and kindness of those around me these past seven years. I cannot express enough how grateful I am to everyone who has supported me throughout this journey or all the years of my life before, but I will try my best here.

I would like to thank my advisors, Kayhan Gültekin and Mateusz Ruszkowski for their mentorship and encouragement as we chipped away at the science presented here. Many of these years were spent pushing against the edge of what is possible, and I appreciate them for remaining optimistic that those endeavors would work out, even when my own morale abandoned me. Imposter syndrome is an easy hole to fall into in academia. I am grateful that my advisors took my scientific input seriously and treated me as a subject expert long before I felt I was myself.

I am also indebted to my other scientific mentor and coauthor, Aleksandra Kuznetsova. Aleksandra is a brilliant scientist and was a valued source of disk simulation wisdom as early as my first year of graduate school. Working more actively with her in the last few years of my PhD has been a highlight of my time in astronomy and the latter chapters of this dissertation would not have been possible without her support and scientific insight.

I am thankful to the other graduate students here, facing their own parallel challenges. Graduate school is hard, and I am lucky to have gone through it alongside so many brilliant, hardworking, and, most of all, kind people. These past seven years would not have been the same without the community, commiseration, and mutual support we provide one another. My heartfelt thanks to those organizing weekly trivia and intramural sports my first year, for giving me a place to belong

when I moved to a city where I didn't know anyone. And thanks to the grad students I now leave behind, especially Cayenne, Thomas, Brandon, Vai, and Mayura, for giving me a place to belong when those I knew before had all graduated and moved away.

My deepest thanks to Nic, Larissa, Kori, Aleksandra, Jim, and Kamber. You know and see me more clearly than anyone and I am so grateful to live in a time where we are able to still see each other every week, despite being scattered across the globe as we are. You are my best friends and I could not have accomplished this without your love and companionship throughout these past seven years. Whatever regrets I have about the path I've taken to get here, I'd retrace every step to know you'd be a part of my life at the end.

Thank you to the non-astronomers in my life, who have kept me grounded and reminded me that there is more to life than science. Thanks to my family, who has cheered me from afar and never doubted that I would succeed. And thanks to my lifelong friends, especially Andy, Zack, Paige, and Allison. You have seen so many different versions of me over the years, and I am grateful that we have remained close throughout all those times and changes. I look forward to being back in Maryland and seeing more of you as I figure out what comes next for me.

And, finally, thanks to all those who have been my friends throughout my life, both named and unnamed. It has been the great blessing of my life to know and be known by so many incredible and kindhearted people. Whatever distance or time now separates us, I would not be where I am or who I am now without your life touching my own. From the bottom of my heart, thanks to all of you.

TABLE OF CONTENTS

DEDICATION ii

ACKNOWLEDGEMENTS iii

LIST OF FIGURES viii

LIST OF APPENDICES x

ABSTRACT xi

CHAPTER

1. Introduction 1

1.1 Formation and Evolution of Supermassive Black Hole Binaries 3
1.2 Observational Identification of SMBHB Candidates 6
1.2.1 Spatially Resolving Dual AGN 8
1.2.2 Mass Deficits in Cored Ellipticals 8
1.2.3 Spectroscopic Inferences 9
1.2.4 Twisted and Wiggling Jet Structures 10
1.2.5 Gravitational Waves 11
1.2.6 Periodic Photometric Variability 13
1.3 Numerical Predictions of SMBHB Signatures and Evolution 17
1.3.1 Accretion Rates 17
1.3.2 Orbital Evolution 20
1.3.3 Reality is 3D and Other Considerations 21
1.4 Dissertation Overview 23

2. Multiwavelength Correlated Variability From a Thermally-Evolving Supermassive Black Hole Binary 25

2.1 Abstract 25
2.2 Introduction 26
2.3 Methods 28

2.3.1 Simulation Setup . . . 29
2.3.1.1 FARGO3D . . . 31
2.3.1.2 Gravity . . . 31
2.3.1.3 Gas Accretion . . . 33
2.3.1.4 Heating . . . 34
2.3.1.5 Cooling . . . 35
2.3.2 Analysis Routines . . . 36
2.4 Analysis & Results . . . 39
2.4.1 Disk Morphology . . . 39
2.4.1.1 Surface Density . . . 39
2.4.1.2 Surface Temperature . . . 40
2.4.2 Accretion onto the Black Holes . . . 40
2.4.3 Electromagnetic Emission . . . 41
2.5 Discussion . . . 45
2.5.1 Origins of Electromagnetic Variability . . . 45
2.5.2 Observational Consequences . . . 45
2.5.2.1 Variability . . . 46
2.5.2.2 Continuum Features . . . 46
2.5.3 Additional Considerations . . . 47
2.6 Conclusion . . . 48
2.7 Acknowledgements . . . 49

3. Shock-Driven Periodic Variability in a Low-Mass-Ratio Supermassive Black Hole Binary . . . 51

3.1 Abstract . . . 51
3.2 Introduction . . . 52
3.3 Methods . . . 55
3.3.1 FARGO3D . . . 55
3.3.2 Disk Setup . . . 55
3.3.3 Gravity . . . 58
3.3.4 Accretion Model . . . 59
3.3.5 Shock Capturing . . . 60
3.4 Results . . . 61
3.4.1 Disk Morphology and Dynamics . . . 61
3.4.2 Electromagnetic Emission . . . 67
3.4.2.1 Shocks . . . 68
3.4.2.2 Accretion . . . 69
3.5 Discussion . . . 69
3.5.1 Disk Dynamics . . . 70
3.5.2 Variability . . . 71
3.5.3 Binary Orbital Evolution . . . 73
3.6 Summary . . . 74
3.7 Acknowledgements . . . 76

4. Prospects for Gravitational Wave Detection of Gas-Dominated Supermassive Black Hole Binary Interactions . . . 77

4.1 Abstract . . . 77
4.2 Introduction . . . 78
4.3 Methods . . . 81
4.3.1 Observational constraints . . . 84
4.3.2 Model constraints . . . 85
4.3.3 Multi-zone α-disk . . . 88
4.3.3.1 Disk zones . . . 88
4.3.3.2 Migration . . . 89
4.3.4 Constant aspect ratio disk . . . 92
4.4 Results & Discussion . . . 96
4.4.1 Multi-zone α-disk . . . 96
4.4.2 Constant aspect-ratio disk . . . 99
4.4.3 Comparison to Existing Numerical Works . . . 99
4.4.4 Caveats and Additional Considerations . . . 102
4.5 Conclusions . . . 103
4.6 Acknowledgements . . . 105

5. Conclusion . . . 106

5.1 Summary of Findings . . . 107
5.1.1 Simulation Predictions of EM Signatures from Supermassive Black Hole Binaries . . . 107
5.1.2 Applicability of Simulation Predictions to the Observable Parameter Space . . . 108
5.2 Future Directions . . . 108
5.2.1 Final Remarks . . . 109

APPENDICES . . . 111
A.1 2D Pressureless Accretion . . . 112
A.2 Cooling of a Uniform Gas . . . 116
B.1 Derivation of Disk Model used for Chapter 2 . . . 118
C.1 An Alternative View of Our Constraints . . . 123

BIBLIOGRAPHY . . . 126

LIST OF FIGURES

Figure

1.1 Lai & Muñoz (2023) illustration of the morphological features of an equal-mass SMBHB embedded in a circumbinary accretion disk. 6
1.2 D'Orazio & Charisi (2023) overview of different SMBHB observational signatures across the binary parameter space. 7
1.3 Agazie et al. (2023c) plot of the NANOGrav 15-year dataset analysis of interpulsar correlations (blue) compared to the Hellings & Downs prediction for an isotropic GWB (black dashed). 13
1.4 Charisi et al. (2022) illustration of line-of-sight velocities for each component of a binary with total mass $M = 10^9$ $M_\odot$, mass ratio $q = 0.25$, inclination $i = 60^\circ$, and a period of 1 yr. 15
1.5 Lai & Muñoz (2023) illustration of accretion variability timescales and their dynamical origins for a disk-embedded SMBHB. 19
2.1 Initial radial profiles for disk surface density (*left*) and midplane temperature (*right*) based on the 1D analytic work by Kocsis et al. (2012a) for the quasi steady-state of a SMBH binary with our chosen parameters. 30
2.2 Construction of the system spectral energy distribution from cooling outputs. . . 36
2.3 Evolution of the disk surface density and surface temperature from initial conditions to quasi-steady state. 38
2.4 Azimuthally averaged surface density (*left*) and surface temperature (*right*) of the disk as a function of radius, with radius in units of the binary separation. . . . 39
2.5 Late-time mass accretion rate onto each SMBH, scaled to that SMBH's Eddington accretion rate (assuming a radiative efficiency of 0.1). 41
2.6 Fourier transforms of the accretion rates shown in Fig 2.5. 42
2.7 Variability of the system's spectral energy distribution. 43
2.8 A more detailed look at the system variability at specific photon frequencies. . . . 44
2.9 Comparison of simulation SED (solid purple line) to standard solution for an α-disk around a single SMBH (dashed orange line). 47
3.1 The initial conditions used for the simulation, calculated from the disk model described in Section 3.3.2. 56
3.2 Snapshots of the gas surface density over time. 62
3.3 Total angular momentum deficit between $r = 200\,R_{\rm g}$ and $r = 400\,R_{\rm g}$. 63

3.4 Eccentricity profile of the disk as a function of radial coordinate r (solid purple) and semimajor axis a (dashed orange). 64
3.5 Torque density (purple) and integrated torque (orange) exerted by the binary on the disk. 64
3.6 Azimuthally-averaged surface density $\bar{\Sigma}$ (*top*) and azimuthally-summed shock flux $F_{\rm shock}$ (*bottom*) as functions of time. 65
3.7 *Top*: Shock dissipation rate summed over the disk (left) and accretion rate onto the secondary SMBH (right), shown over the full runtime of the simulation. . . . 67
3.8 Examination of the timing relationship between shocks and accretion. 73
4.1 Model-dependent constraints, for a range of disk parameter values. 93
4.2 Variation of constraints with disk parameters as in Figure 4.1, but for the constant aspect-ratio model. 95
4.3 Illustration of our constraints on the SMBHB parameter space, with the region shaded in soft green being the subset of the parameter space which meets all our constraints. 97
4.4 Illustration of all constraints as in Figure 4.3, but for the constant aspect-ratio model. 100
4.5 Sample of numerical studies which specify M and a overplotted on the $q = 1$ panel of Figure 4.3. 101
A.1 *Top*: Accretion rate as a function of time. 116
A.2 *Top*: Average gas temperature as a function of time. 117
C.1 The same data as in Figure 4.3, but plotted as mass ratio vs separation for example masses rather than mass vs separation for example mass ratios. 124
C.2 The same data as in Figure 4.3, but plotted as mass ratio vs separation for example masses rather than mass vs separation for example mass ratios. 125

LIST OF APPENDICES

Appendix

A. 112

B. 118

C. 123

ABSTRACT

Supermassive black hole binaries (SMBHBs) are, by all means, expected to exist; galaxies contain supermassive black holes, galaxies merge, and, so, there ought to be galaxies containing multiple supermassive black holes which, through a sequence of physical processes, will be drawn together and become bound to one another as a binary. Being able to find these binaries in the real universe requires an understanding of how the light they produce might distinguish them from systems with only one supermassive black hole. There are two main goals of this thesis. The first is to characterize the time-varying electromagnetic emission of supermassive black hole binaries embedded in a circumbinary accretion disk using hydrodynamics simulations. The second is to determine the binary parameter space accurately probed by these simulations and previous simulation works and compare this to the parameter space available to electromagnetic monitoring and gravitational wave detectors. I identify the importance of shocks driven by the binary as a source of hard X-ray variability by monitoring the radiative emissions from a disk-embedded SMBHB with robust thermal evolution (Chapter 2). By monitoring dissipation of energy via shocks in an isothermal SMBHB simulation, I demonstrate that the shock-driven variability can be recovered even without explicit thermal evolution and show that it is anti-correlated with the longer-wavelength variability inferred from accretion rates, a unique time-domain signature which would not appear in a single-SMBH system (Chapter 3). In Chapter 4, I examine the binary parameter space probed by numerical models like those in Chapters 2 and 3 and how they compare to the parameter space that can be accessed by time-domain electromagnetic surveys and gravitational wave observatories. The results of this work motivate future observational efforts via a new multiwavelength time-domain signature for binary candidacy and future numerical efforts by identifying the physics most necessary to better model the SMBHB population accessible to multimessenger study.

CHAPTER 1

Introduction

Supermassive black holes (SMBHs), with masses $\gtrsim 10^6$ $M_\odot$ are thought to occupy the center of most massive galaxies (Richstone et al., 1998; Kormendy & Ho, 2013). As SMBHs do not themselves emit light, most detections are of those which are actively accreting material from a surrounding disk of hot gas made luminous by the viscous dissipation of rotational energy. Such SMBHs are called active galactic nuclei (AGN), while those that are not accreting, like our own Galaxy's Sagittarius A*, are deemed quiescent and are correspondingly more difficult to detect.

The hierarchical merging of galaxies with one another is expected to play a key role in much of AGN behavior. Tidal forces during a gas-rich galaxy merger can funnel significant quantities of gas towards the SMBH, triggering accretion (Volonteri et al., 2003; Hopkins et al., 2005; Barnes & Hernquist, 1991; Anglés-Alcázar et al., 2017), though observational confirmation of a merger-AGN correlation is complicated by relatively short-timescale stochastic AGN variability (Hickox et al., 2014) and obscuration (Kocevski et al., 2015; Weston et al., 2017). At the same time, galaxy mergers can also trigger star formation which in turn produces supernovae which drive strong outflows, quenching the fuel supply of the AGN (Sobral et al., 2015). Similarly, AGN activity also produces feedback in the form of radiation, winds, and jets, which heat surrounding gas and drive it out of the galaxy, quenching star formation (Morganti, 2017). As massive galaxies may each contain a supermassive black hole, mergers can result in a galaxy which contains two SMBHs, which may become bound to one another as a binary and, eventually, merge. These SMBH mergers

constitute a potentially significant channel for the mass and spin evolution of SMBHs (Sanchez et al., 2018) and may be a key mechanism behind observed galaxy-SMBH scaling relations (Jahnke & Macciò, 2011) like the $M_{\rm bh}$–$M_{\rm bulge}$ relation (Magorrian et al., 1998; Marconi & Hunt, 2003; Häring & Rix, 2004).

The supermassive black hole binaries (SMBHBs) which precede mergers are elusive systems, with exactly zero confirmed in observations at sub-parsec separations. However, as precursors to SMBH mergers, they are essential for the identification of mergers and the study of the life and evolution of SMBHs. Further, as the primary channel of SMBHB formation is considered to be galaxy mergers, characterizing SMBHBs may also provide insights on galaxy–SMBH co-evolution. In order to characterize the role of galaxy mergers in supermassive black hole evolution, we must first get an accurate census of the SMBHB occupation fraction and the distribution of properties (e.g., masses, mass ratios, separations, eccentricities, etc.) for that SMBHB population. The critical barrier to overcome is in confidently differentiating systems which contain a SMBHB from those that contain a single SMBH.

SMBHBs are multi-messenger systems. They are expected to produce electromagnetic (EM) emission as they interact with surrounding gas, as well as gravitational waves (GWs) which will be detectable by low-frequency GW observatories like pulsar timing arrays (PTAs) and the upcoming Laser Interferometer Space Antenna (*LISA*) in the coming years and decades. Better understanding the EM signatures of SMBHBs will allow for better candidate identification in survey data of AGN, while GWs will provide direct evidence for individual SMBHBs and tightly constrain their orbital parameters. As the loudest gravitational wave (GW) events in the universe, SMBH mergers and the preceding SMBHB phase provide a unique testing site for the predictions of general relativity. In particular, their nature as EM-GW multi-messenger sources can be used to probe the assumption that EM and GW signals both propagate at the same speed (Cutler et al., 2003; Takahashi, 2017).

In this body of work, I explore the time-varying electromagnetic (EM) signatures of SMBHBs using numerical simulations and examine the applicability of my models, as well as those of other works, to the physical conditions expected for the SMBHBs which will be detectable by

GW observatories.This work aims to inform observational searches for SMBHBs by identifying time-domain variability patterns unique from single-SMBH AGN and to inform future numerical efforts by identifying the modeling advancements most necessary to probe the observable SMBHB parameter space.

1.1 Formation and Evolution of Supermassive Black Hole Binaries

In order to search for SMBHBs, we must first understand where they come from, the environments they live in, and the relevant physics of how they interact with those environments. To this end, let us review the evolution of an SMBHB from the initial unbound state down to merger (Begelman et al., 1980).

The most likely and most explored channel for SMBHB formation starts from the merger of two galaxies that each host a SMBH. The post-merger galaxy then hosts two SMBHs, though they are initially separated by kiloparsecs: too far apart to be bound to one another. At these largest scales, the SMBHs will individually be driven towards the center of the merged galaxy via dynamical friction, in which kinetic energy is dissipated away from each SMBH by cumulative gravitational interactions between the individual SMBHs and the surrounding stars and gas. Over time, the loss of energy will lead the SMBHs to sink towards the bottom of the central gravitational potential. They will become bound to one another, forming a SMBHB, when they reach parsec-scale separations.

At this point, dynamical friction becomes too inefficient to further reduce the binary separation and further evolution becomes driven by orbital energy loss due to three-body interactions of the binary with the stars in its surrounding environment. The SMBHB-to-star energy transfer is ineffective for interactions which last longer than the binary orbital period, so close, short-lived approaches are necessary to efficiently harden the binary orbit (Heggie, 1975). Stars which do make close approaches to the binary can slingshot off of it, taking some of the energy of the binary as they are flung away (Khan et al., 2012a). This loss of energy shrinks the binary separation, but the supply of stars making close enough approaches quickly depletes, stalling the binary's continued

evolution.

Early explorations of these three-body interactions considered a spherical distribution of surrounding stars and found that binaries would stall at a separation of ~ 1 pc (Milosavljević & Merritt, 2003), leading the problem of how to un-stall the evolution to be dubbed the "Final Parsec Problem." While there is yet no confirmation that this stalling does not occur, there are several proposed realistic solutions to the Final Parsec Problem:

1. Non-spherical (e.g., triaxial) stellar distributions can produce torques on individual stars which send them on orbits close to the SMBHB, refilling the population of stars which can carry away angular momentum and energy from the binary (Merritt & Poon, 2004; Khan et al., 2012b; Avramov et al., 2021).

2. Gas funneled into the galactic center following the merger can provide additional material to carry away energy from the binary via dynamical friction (Barnes & Hernquist, 1996; Dotti et al., 2007).

3. An additional massive perturber, such as a third SMBH introduced by a subsequent galaxy merger or a star cluster on an orbit which intersects with the binary, can provide another source of energy loss for the SMBHB via dynamical interactions (Perets et al., 2007; Bortolas et al., 2018; Ryu et al., 2018).

At sub-parsec scales, if the binary is actively accreting, it will be surrounded by or embedded in a gaseous accretion disk. This disk is geometrically thin, optically thick, and produces bright thermal emission in optical–UV wavelengths for typical SMBH masses ($\sim 10^6$–10^9 $M_\odot$). This emission results from viscous dissipation of kinetic energy due to the differential rotation of disk annuli which each orbit at approximately the local Keplerian velocity. The conventional model of such a disk is the α-disk described by Shakura & Sunyaev (1973), which parameterizes the kinematic viscosity of the disk as $\nu = \alpha c_s H$, where c_s is the local sound speed, H is the disk scale height, and α is a constant.

For an accreting binary, orbital evolution at sub-pc separations will initially be driven by dynamical interactions between the SMBHB and the surrounding accretion disk. The typical morphology of an accreting SMBHB is shown in Figure 1.1 and depends on the binary mass ratio $q = m_2/m_1 \leq 1$. For $q << 1$ binaries, the disk is centered on the primary SMBH, with the secondary on an orbit embedded in the disk (right panel of Fig. 1.1). The secondary exerts a gravitational torque on the disk material, perturbing the path of local gas, launching spiral density waves, and exchanging angular momentum between the secondary and the disk. For a sufficiently massive secondary $q \gtrsim 10^{-3}$, this torque is strong enough to open a gap in the disk as the secondary transmits angular momentum to gas outward of it and takes angular momentum from gas inward of it. The secondary's gravity will pull gas off of the edges of this gap, forming accretion streams which feed a small accretion disk or "mini-disk" around the secondary SMBH.

For these gap-opening secondaries, the secondary SMBH migrates inward in a process akin to Type-II planetary migration, where the migration timescale is expected to depend on the local disk mass (the mass interior to the secondary orbit) relative to the mass of the secondary. Thus, at large separations, the local disk may be more massive than the secondary and the secondary will drift inward on the viscous timescale of the disk. At smaller separations or for mass ratios near unity, the secondary will be more massive than the local disk and its inertia will therefore slow down the migration (Syer & Clarke, 1995). For equal mass binaries ($q \sim 1$), the accretion disk becomes circumbinary, with the binary clearing a central cavity rather than a gap and with each binary component accreting from its own mini-disk fed from the cavity edge (left panel of Fig. 1.1). While the Type-II migration analogy broadly holds, the reality of accreting SMBHB migration rates is more complicated than this picture, depending on accretion torques as well as gravitational ones, and is a subject of debate in the simulation literature, discussed in greater detail in 1.3.2.

At the smallest separations ($\lesssim$100 R_g, with $R_g \equiv GM/c^2$ being the gravitational radius of the central object), whether accreting or not, the binary's evolution becomes dominated by gravitational wave emission. Gravitational radiation removes energy from the binary, reducing the

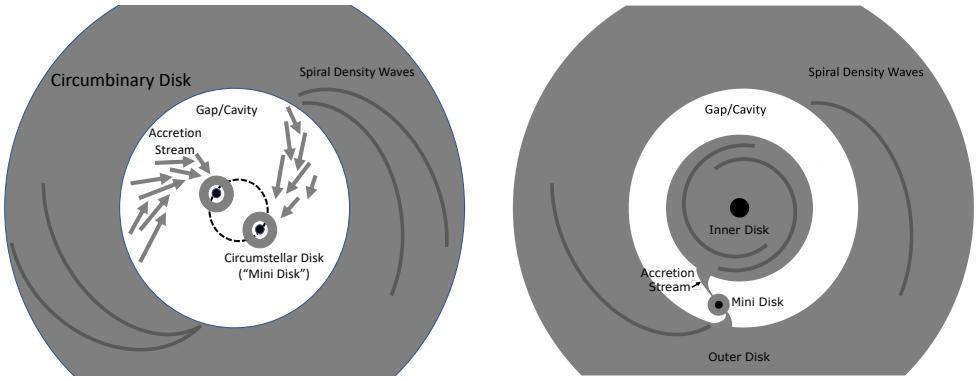


Figure 1.1: *Left*: Lai & Muñoz (2023) illustration of the morphological features of an equal-mass SMBHB embedded in a circumbinary accretion disk. *Right*: Illustration of the morphology of a low-mass-ratio SMBHB embedded in an accretion disk, made in the style of the Lai & Muñoz (2023) equal-mass illustration.

separation and, for initially eccentric binaries, circularizing the orbit. Eventually, the binary will coalesce, producing a GW "chirp" like those observed for stellar-mass BH binaries with LIGO, but at a lower ($\sim$mHz) frequency.

1.2 Observational Identification of SMBHB Candidates

While we have a general theoretical understanding of the life cycle of a SMBHB, there remains the challenge of identifying and studying SMBHBs at different phases in order to constrain the actual physics of their mass growth and the evolution of their orbital separations and eccentricities. Different techniques probe different binary separations, but all are necessary to form a complete picture of SMBHB demographics and evolution. I review here several such techniques (namely, spatial resolution, cored ellipticals, spectroscopic inference, helical jets, gravitational waves, and periodic photometric variability), the subset of the SMBHB parameter space to which they are applicable, and note some studies using these techniques to identify candidate SMBHBs. Figure 1.2 presents an overview of these techniques and candidate SMBHBs identified using them.

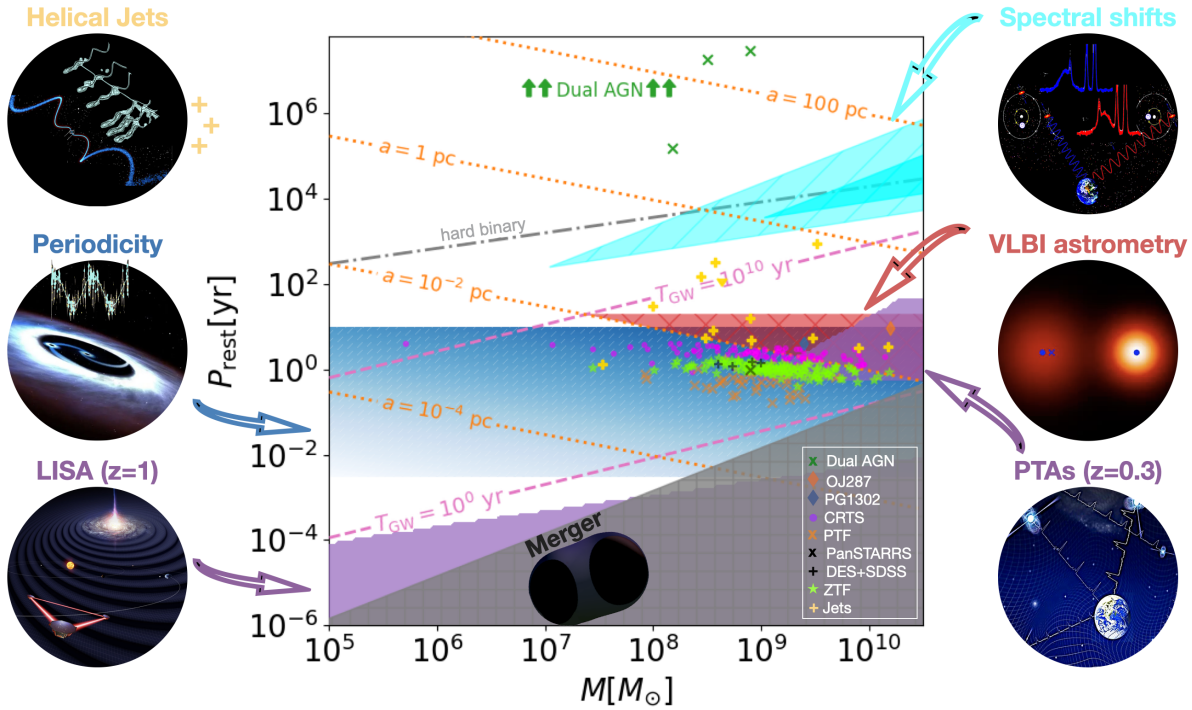


Figure 1.2: D'Orazio & Charisi (2023) overview of different SMBHB observational signatures across the binary parameter space. Binaries below the grey dot-dashed "hard binary" line are considered to be bound, with the green x's above the line representing dual AGN candidates and the Rodriguez et al. (2006) AGN pair. The yellow +'s show candidates with helical jet structures, and all the other symbols denote either specific candidates of promise or candidates identified by periodicity identified in systematic searches of photometric survey data. Shaded regions indicate the subset of the binary parameter space which can be probed with different candidate signatures

1.2.1 Spatially Resolving Dual AGN

In the early post-merger stages, the SMBH pair is separated by kiloparsecs of space, not yet bound into a true binary. On such scales, and even down to a few tens of parsecs, dual AGN, where both SMBHs independently accrete from their respective environments, can be spatially resolved using high-resolution telescopes like *Chandra* or the *Hubble Space Telescope* (*HST*) (Liu et al., 2018) or techniques such as very long baseline interferometry (VLBI) with radio telescopes (e.g., Rodriguez et al., 2006). At a redshift of $z = 1.4$, where the angular luminosity distance reaches its peak of ~ 1.8 Gpc, *HST* can resolve dual AGN down to ~ 500 pc separations and *Chandra* can resolve down to ~ 5 kpc separations. As there are few plausible highly-luminous X-ray sources besides SMBH accretion (Lehmer et al., 2010), enhancing the effective resolution of X-ray telescopes with robust Bayesian techniques such as BAYMAX (Foord et al., 2019, 2020, 2021) is of particular value for identifying dual AGN.

1.2.2 Mass Deficits in Cored Ellipticals

As mentioned in 1.1, SMBHBs will scatter nearby stars in three-body interactions, removing them from the central region surrounding the SMBHB and shrinking the binary separation as angular momentum and energy are carried off by the banished star. Eventually, this depletion of stars in the galactic center should be observable as a flattening at the center elliptical galaxy brightness profiles. Such "cored" ellipticals are indeed seen in observations (Kormendy & Ho, 2013). While non-SMBHB interpretations exist, the mass deficits predicted from the binary hypothesis match up with the measured SMBH masses in cored ellipticals (Kormendy & Bender, 2009) and the size of the core matches the SMBH sphere of influence (Thomas et al., 2016), lending weight to a binary origin for at least some cored ellipticals. However, the cores are expected to persist long after the binary merger, making cored ellipticals evidence of past binary presence rather than necessarily implying a current SMBHB occupant. Comparisons between observed mass deficits and mass deficits calculated from IllustrisTNG results find that the core scouring process requires large binary mass ratios $q \gtrsim 0.7$ (Harris & Gültekin, 2024).

1.2.3 Spectroscopic Inferences

Analysis of AGN spectra is commonly used as a means of identifying candidate SMBHBs, as there are several plausible spectroscopic signatures that may arise from the orbital motion of two AGN in a binary. The ionized gas surrounding an accreting SMBH or SMBHB produces a collection of emission lines from various atomic transitions (e.g., O III and Hβ). Emission from gas closer to the central object will be Doppler broadened due to the high orbital velocity (dubbing this the broad line region or BLR), while emission from further away, where the gas orbits more slowly, is not significantly broadened, resulting in relatively narrow emission lines (similarly dubbed the narrow line region or NLR). As the BLR is more closely bound to the central object, it can provide insight into the motions of that central object.

The simplest case is that if each SMBH in a binary possesses its own BLR, then one will observe double-peaked broad lines from that system, with the offset between the two broad lines owed to the different line-of-sight velocities of each binary component. While multiple candidates have been proposed based on this feature, it can also be seen in single AGN, evidenced by, e.g., single-peaked Lyα lines in a source with double-peaked Balmer lines or unrealistically large minimum SMBHB masses ($> 10^{10}$ $M_\odot$) calculated from the radial velocities inferred from the peak separations (Eracleous et al., 1997; Liu et al., 2016; Doan et al., 2020). Additionally, as the broad lines are, in fact, broad, the offset must be large enough for the double-peak to be resolvable. Since the width of the lines are set by the velocity of the BLR and the separation of the peaks is set by the lower velocity of the binary components, the peaks should be separated by less than their width, tightly constraining the orbital configurations that can be probed with such a feature (Shen & Loeb, 2010; Kelley, 2021).

The other binary signature is broad lines which are offset from their narrow line counterparts. This offset can be inferred as a coherent motion of the central object the BLR is bound to relative to the far-out NLR (Eracleous et al., 2012). Such an offset can be identified in single-epoch spectroscopic observations, but multi-epoch observations can identify time-variable offsets as a more robust test. Offsets which evolve coherently over time would be expected for a system where the

BLR is attached to a component of a binary and can, in turn, be used to constrain the binary parameters (Runnoe et al., 2017). Alternatively, offsets which do not evolve or do not imply motions consistent with a binary can be ruled out as SMBHB candidates (Wang et al., 2017). In general, observing broad line offsets targets binaries with separations of 0.1–10 pc, close enough together that the orbital velocities produce resolvable offsets, but far enough apart that at least one can maintain its own BLR (Kelley, 2021).

Binary-driven spectral signatures are also possible at smaller separations, when the SMBHB is embedded in an accretion disk. One proposed signature is that, to first order, the gap or cavity opened in the disk by the binary implies a lack of emission from those radii, leading to a "notch" in the spectral energy distribution of the disk at optical–UV wavelengths (Gültekin & Miller, 2012). However, numerical studies have since found that shocks and tidal heating driven by the binary compensate for the "lost" emission from the gap and, further, that shocks produce an excess of high-energy emission, relative to a single-SMBH disk, which serves as a unique spectral signature of its own (Farris et al., 2015; Tang et al., 2018; Westernacher-Schneider et al., 2022; Whitley et al., 2024). GRMHD simulations of near-merger binaries also find that there is a high-energy emission component from inverse Compton scattering in the optically thin cavity (d'Ascoli et al., 2018; Gutiérrez et al., 2022). While searches for unusual X-ray-to-optical flux ratios in AGN have been performed, no strong candidates have yet been identified in this way (Saade et al., 2020, 2023).

1.2.4 Twisted and Wiggling Jet Structures

Accretion onto a SMBH, at times, results in the launching of a relativistic jet which can extend over vast spatial scales ($\sim$kpc–Mpc) and shines brightly at radio and X-ray wavelengths. For a stationary SMBH, one expects that the jet should be straight, with material being launched away from the central object in a single orientation. However, if the central object at the base of the jet is moving, as in a binary, the jet will trace out a twisted, helical structure over time. Due to relativistic time dilation, monitoring precessing blazar jets can serve as a probe of binaries with periods on the order of decades to centuries (e.g., the candidate examined in Caproni et al., 2013). However,

similar helicity can be produced by precession of the jet caused by, e.g., Lense-Thirring precession from a disk misaligned with the central SMBH's spin, with no need for a second SMBH (Liska et al., 2018). Additionally, interactions of the jet with its surrounding environment can distort the jet structure, potentially mirroring the "wiggly" structure generated from orbital motions or precession. Finally, only $\sim$10% of AGN are radio-loud (i.e., have large-scale jets), limiting the population to which this signature is relevant, even if helical structure was exclusive to binaries. (Lobanov & Zensus, 2001)

1.2.5 Gravitational Waves

Gravitational waves (GWs) will detect SMBHBs during and approaching merger, at separations of order $\sim 10^3$ gravitational radii and below. A binary will emit a spectrum of GWs depending on its eccentricity and orbital frequency $\Omega = \sqrt{GM/a^3}$, but for a circular orbit, this is dominated by GW emission at twice the orbital frequency of the binary. As supermassive binaries spend most of their lives at much larger separations than stellar mass binaries, the GWs they emit will be at much lower frequencies. For these low frequencies supermassive binaries emit at, there are essentially two relevant types of GW observatories: 1) space-based interferometers like *LISA* and 2) pulsar timing arrays (PTAs).

LISA functions under broadly similar principles to ground-based interferometers like LIGO. However, instead of a single source being split, reflected back, and self-interfering, each of the LISA spacecrafts measures the interference of its outgoing and incoming beams. Then, measurements from each spacecraft are combined in order to cancel noise from the individual lasers, accounting for time delays between the measurements each spacecraft makes. Passing GWs will stretch and contract the paths of the lasers, producing correlations between the individual measurements which can be used to detect the GW. However, more massive binaries emit at lower frequencies ($\sim$mHz–nHz) than the stellar mass systems LIGO observes ($\sim$Hz–kHz), requiring longer interferometer arms. For the mHz GWs targeted by LISA, this takes arm lengths of order 10^6 km, necessitating that such an observatory be space-borne. LISA will be comprised of three

spacecrafts arranged in an equilateral triangle trailing the Earth's orbit by 20 degrees and is expected to launch sometime in the 2030s. It will be sensitive to merging binaries with total masses $\sim 10^5$–10^7 $M_\odot$ and is predicted to detect 1 to a few hundred mergers per year out to redshifts as far as $z = 20$ (Amaro-Seoane et al., 2023). In addition to mergers, LISA will be able to detect and follow SMBHB inspirals days or months ahead of the merger, providing sufficient data to measure the parameters of individual binaries and constrain the distribution of those parameters among the merging binary population (Amaro-Seoane et al., 2017). Comparisons of these parameters to those predicted from various SMBHB evolution models will advance our understanding of how and which SMBHBs get to the merger stage.

Just as LISA needed longer arms to measure lower GW frequencies than LIGO, observing nHz GWs requires even longer arms. But making an interferometer on the necessary scale of even μHz GWs would be an engineering marvel. So, to reach the length scales necessary to measure nHz GWs, we use pulsar timing arrays (PTAs). A PTA is a galaxy-wide GW observatory based on the precise monitoring of a collection of millisecond pulsars (MSPs) throughout the galaxy, whose effective baseline is the $\gtrsim 0.1$ kpc distances between Earth and the MSPs of the array. MSPs typically have very stable periods. When GWs from SMBHBs pass through our galaxy, the distance between Earth and the pulsar is perturbed, causing coherent deviations in the arrival time of radio pulses from the MSP. When considering a collection of MSPs throughout the galaxy, these deviations in pulse arrival times should be spatially correlated in a characteristic way. For an isotropic gravitational wave background (GWB), as is expected to be produced by a population of SMBHBs throughout the universe, this characteristic spatial correlation in MSP timing deviations is described by the Hellings & Downs curve (Hellings & Downs, 1983) seen in Figure 1.3.

Several independent PTA collaborations (e.g., NANOGrav (Jenet et al., 2009), EPTA (Kramer & Champion, 2013), and CPTA (Lee, 2016), among others) systematically monitor MSPs to detect nHz GWs and collectively share their efforts as the International Pulsar Timing Array (IPTA; Hobbs et al. (2010)). Recently, the major PTA collaborations have reported evidence for a GWB consistent with the Hellings & Downs predictions (see Figure 1.3). The origin of this background

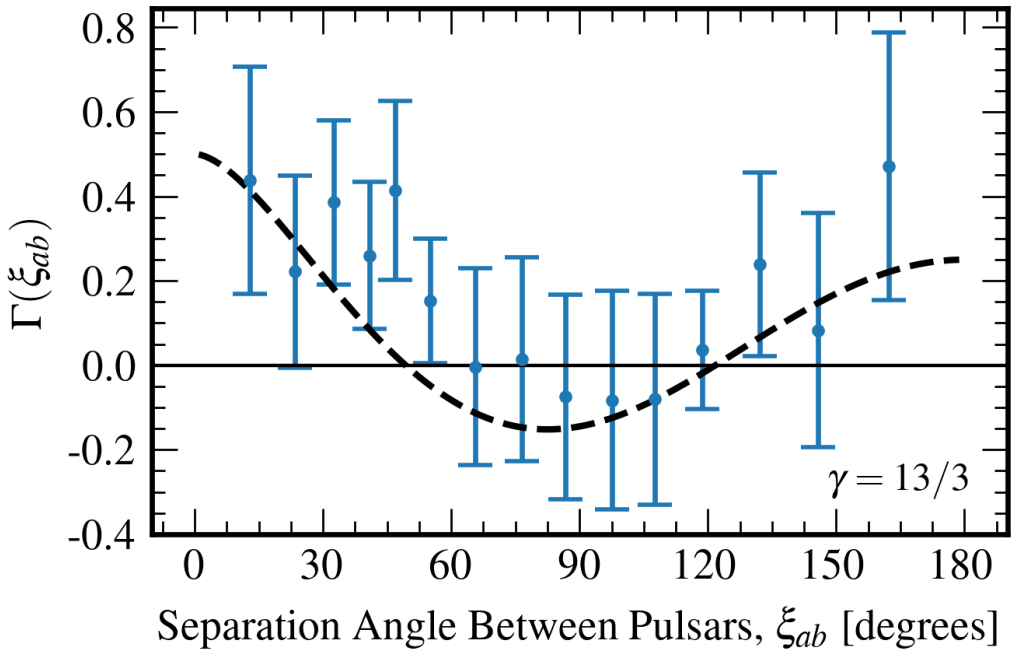


Figure 1.3: Agazie et al. (2023c) plot of the NANOGrav 15-year dataset analysis of interpulsar correlations (blue) compared to the Hellings & Downs prediction for an isotropic GWB (black dashed). The agreement between PTA data and the Hellings & Downs correlations constitutes early evidence for the detection of a GWB.

is yet to be determined, but can be modeled by a realistic population of SMBHBs (Agazie et al., 2023b). As PTAs continue to collect data, the signal-to-noise ratio will improve, and individual SMBHBs may be resolvable in the next few years, opening the door for multi-messenger EM+GW observations of SMBHBs. Characterizing the EM emission of GW-confirmed SMBHBs will help further efforts to identify an EM signature which has real predictive power in differentiating SMBHBs from single-SMBH AGN.

1.2.6 Periodic Photometric Variability

The last signature, and the focus of this dissertation, is periodic photometric variability. Depending on the physical origin, such variability may be seen across the electromagnetic spectrum and may be found via dedicated searches of photometric survey datasets like SDSS or the upcoming Vera Rubin Observatory. There are two major ways such periodicity can be manifested and they are not mutually exclusive: 1) orbit-driven enhancements of existing emission (e.g., Doppler

boosting, self-lensing) and 2) hydrodynamic variability (e.g., accretion modulation, shocks).

At sub-pc separations, the orbital velocities in a binary can be an appreciable fraction of the speed of light, resulting in relativistic effects when a component of this velocity is along the observer's line of sight. The relativistic Doppler boost causes radiation from a source to appear brighter and bluer when the source is moving towards the observer, and dimmer and redder when the source is moving away. Over the course of an orbit, this results in a periodic modulation of the emission. For sub-pc SMBHBs, the amplitude of this modulation can be as high as $\sim 10\%$, observable provided other sources of variability do not overwhelm it. If both SMBHs are accreting, the secondary will have a more pronounced Doppler boost due to its higher orbital velocity, though the total effect will be diminished somewhat by the opposing motion of the primary (Figure 1.4). In the case of a circular binary orbit, this modulation is sinusoidal. Non-zero eccentricities distort this sinusoid and introduce a dependence on the binary argument of periapse due to the non-constant orbital velocities (Hu et al., 2020). Further deviations can be introduced if the source luminosity being boosted (e.g., the secondary's accretion disk) is not constant (Charisi et al., 2022).

If the binary is aligned nearly edge-on to the observer's line of sight, it is possible for the binary to self-lens. In this configuration, light from the material around one binary component is gravitationally lensed when it passes behind the other, briefly magnifying the observed luminosity. These lensing flares are symmetric and will occur in addition to the Doppler boost discussed before. For circular orbits, the flare will occur at the average value of the Doppler signal, as there is zero velocity along the line of sight when one component passes in front of the other. For eccentric orbits, the width of the flares and the phase of the Doppler signal they occur at depends on the eccentricity and the argument of pericenter (e.g., lensing flares become wider if they occur near apoapsis, as the slower orbital velocity means the binary stays in the lensing configuration longer). Precession of an eccentric binary can also cause the phase of the lensing flares to drift over time as the orbital phase where the SMBHs are in conjunction changes. While the self-lensing configuration is rare, with only one decent candidate (the "Spikey" system, KIC 11606854; Hu et al. (2020)), the combined Doppler/self-lensing model can constrain the candidate orbital period, providing a

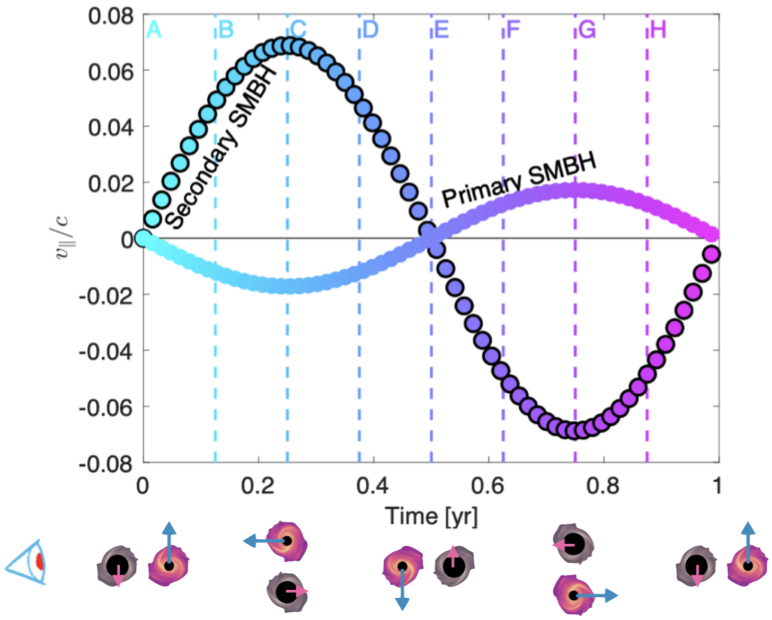


Figure 1.4: Charisi et al. (2022) illustration of line-of-sight velocities for each component of a binary with total mass $M = 10^9$ $M_\odot$, mass ratio $q = 0.25$, inclination $i = 60°$, and a period of 1 yr. The lower illustration by D'Orazio & Charisi (2023) shows the binary-observer configuration at sample phases of the orbit, with the secondary in color and the primary in greyscale. As the secondary orbits with a higher velocity, it dominates the resulting Doppler variability pattern, though the opposing motion of the primary will partially suppress the amplitude of this variability.

prediction of when the next flare should occur — a straightforward test for whether the initial flare is consistent with a binary origin.

Characterizing hydrodynamic variability is the focus of the numerical work in this dissertation and of many previous numerical works. The findings of the simulation literature are detailed in 1.3, but I will introduce the general ideas behind how hydrodynamic effects produce a variable photometric signature now. The first, and most-studied, effect is accretion onto the binary components. The accretion rate of a disk is correlated with the luminosity of the disk, with higher accretion rate disks being brighter. The asymmetric and time-varying binary potential can be expected to drive variations in the flow of material around the binary, producing variable accretion rate onto each SMBH. Since the driving force of this variability is the binary orbit, it is reasonable to expect that the period of this accretion variability will be related to the orbital period of the binary—a prediction confirmed throughout the simulation literature.

The second variable hydrodynamic effect is shocks. At the same time the binary potential is

modulating the accretion flow, it is "sloshing" material around in the gap/cavity the binary resides in. Some of this material is flung into the edge of the cavity, shocking the gas there to high temperatures and thereby enhancing the high-energy emission from the system. Periodic shocks have been noted in several studies as a driver of cavity eccentricity and enhanced continuum X-ray emission (Farris et al., 2015; Tang et al., 2018; Tiede et al., 2022), but their effects on the SMBHB lightcurve had not been studied in detail until the work of this dissertation.

Observationally, the expansion of time-domain surveys in recent decades has made searching for photometric periodicity more viable than ever before. Several systematic searches have been performed on hundreds of thousands of AGN lightcurves from various survey catalogs (Graham et al., 2015b; Liu et al., 2019; Chen et al., 2020, 2024; Charisi et al., 2016). A few hundred candidate SMBHBs have been identified from these searches, with periods ranging from months to years.

However, periodicity searches are susceptible to false positives, largely owing to the fact that single-SMBH AGN are already stochastically variable, which can appear periodic when survey data only covers a few cycles of the proposed period (Vaughan et al., 2016; Witt et al., 2022). (Sesana et al., 2018) suggested that there are too many photometric candidates, as the expected GW background from the SMBHB population inferred from the photometric candidate sample would be in conflict with the PTA upper limits at that time, implying that there are indeed false positives in the candidate pool. The simplest solution for identifying false positives is to just observe candidates for more periods, but this is impractical to do for large numbers of candidates or when those periods are years or decades long. The issue of false positives among photometric candidates might instead be better solved by follow-up searches for additional binary signatures, or identifying an EM signature in simulations which more uniquely distinguishes binaries from single-SMBHs than does simple, single-wavelength periodicity.

1.3 Numerical Predictions of SMBHB Signatures and Evolution

Over the past couple decades, many numerical simulations have been performed to characterize the accretion behavior and orbital evolution of binaries embedded in an accretion disk, both in the context of SMBHBs and also for stellar binaries. The majority of simulations have been performed in 2D, with a locally isothermal equation of state, a constant or α-prescription viscosity, and a constant disk aspect ratio. Even with a simple model like this, simulations of circumbinary accretion are computationally taxing, requiring a wide range of both spatial and time scales to be resolved to accurately capture the behavior of the system. Spatially, the computational domain must cover the large circumbinary disk that feeds the accretion onto the binary while also resolving the narrow spiral waves in both the circumbinary disk and the individual mini-disks in order to accurately calculate the net torque acting on the binary. Temporally, the simulation must resolve the sub-orbital timescales over which accretion is modulated while also running for several hundred to tens of thousands of orbits for the large-scale behavior to reach a quasi-steady state from the initial conditions.

Despite these challenges, numerical simulations have successfully advanced our understanding of circumbinary accretion and generally agree on the key results, at least within the narrow range of disk models typically considered. The important findings can be broadly sorted into two categories: accretion rates and orbital evolution of the binary. We will focus on the results from 2D isothermal simulations, as these are the bulk of the literature, and, after, review what is found by works which deviate from this model.

1.3.1 Accretion Rates

Simulations monitor accretion onto the binary components both as a proxy for the disk luminosity and for its role in evolving the mass and momentum of the SMBHs. In earlier works like MacFadyen & Milosavljević (2008), the binary was beyond the inner boundary of the computational domain and so accretion was tracked by the outflow of material through the inner boundary. More recent simulations include the binary within the simulated domain and implement sink pre-

scriptions to handle the removal of nearby gas from the simulation, preventing unphysical buildup near the point mass, and monitor accreted mass and momentum for each binary component. A variety of sink prescriptions are used throughout the literature, though recent tests favor a torque-free prescription, as this reduces the effect the choice of sink rate (the rate at which density is depleted around the accreting object) has on simulation outcomes (Dittmann & Ryan, 2021).

Despite early expectations that gravitational torques from the binary would suppress accretion (Pringle, 1991), simulations have found that the time-averaged accretion rate onto a binary is comparable to that of accretion onto a single central object of the same mass. Further, this accretion rate is periodically variable, implying a periodic lightcurve for accreting SMBHBs which might be observable in EM surveys.

The accretion rate is modulated on both short timescales (of order the binary orbital period) and long timescales (of order several hundred binary periods), as illustrated in Figure 1.5. Accretion modulation is observed when the binary is able to excite eccentricity in the disk at the outer edge of the gap/cavity, maintained through a combination of gravitational torques and momentum imparted from accretion material being flung back into the cavity edge by the binary (Tiede et al., 2022). Short-period modulation results from material being stripped off from the circumbinary disk when each binary component makes its closest approach to the near side of the gap/cavity each orbit (panel (a) of Fig. 1.5). Long-period modulation is associated with the coherent precession of the eccentric cavity (panel (b) of Fig. 1.5) and, for eccentric binaries, can result in preferential accretion onto one of the binary components, even for an equal-mass binary, with the preferred SMBH switching on timescales of order the cavity's precession timescale (Muñoz & Lai, 2016).

Focusing on the short-period variability, the exact period and shape of the modulation is dependent on the binary parameters, particularly the mass ratio q and the orbital eccentricity e. For circular binaries, the dependence on q is divided into three regimes (D'Orazio et al., 2016; Duffell et al., 2020):

1. $q \gtrsim 0.2$: For large mass ratios, accretion is modulated at once and twice the orbital period of the binary due to the aforementioned periodic stripping of material from the circumbinary

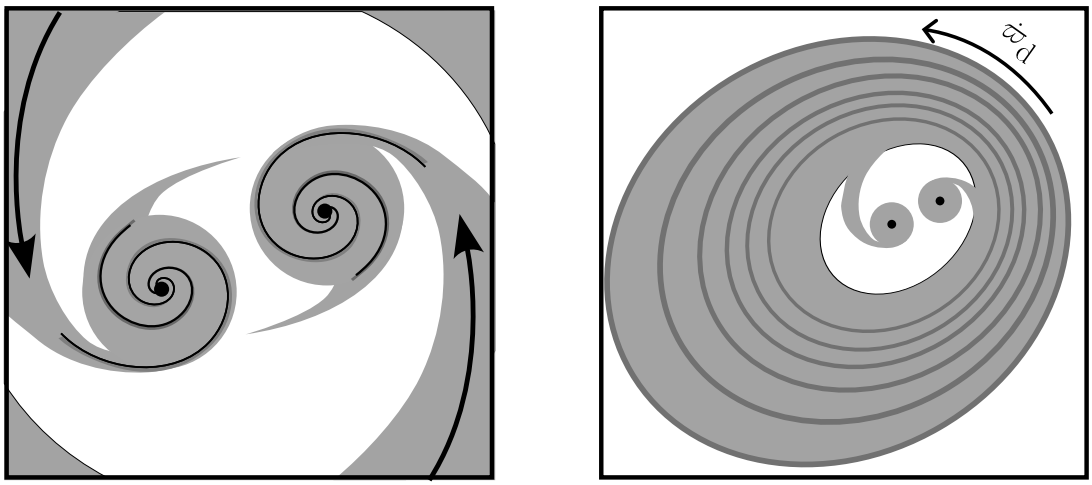


Figure 1.5: Lai & Muñoz (2023) illustration of accretion variability timescales and their dynamical origins for a disk-embedded SMBHB. On short timescales, variability occurs on timescales of order the orbital period of the binary, with enhanced accretion occurring when either SMBH makes its closest approach to the edge of the asymmetric gap. The circumbinary disk precesses on a timescale hundreds of times the orbital period of the binary, modulating the accretion variability over long timescales.

disk. For $q = 1$ the modulation on the orbital period vanishes due to the symmetry of the system. The eccentric cavity develops an overdense "lump" at the edge, which orbits at the Keplerian velocity at the gap edge. For the fiducial $H/R = 0.1$ aspect ratio disk model, with H being the disk scale height at a radius R from the disk center, this results in the lump making its closest approach to the binary every 5 binary periods, producing a higher amplitude accretion enhancement than that of the shorter-period modulations. This lump feature dominates the accretion variability for $q \sim 1$ and is resilient to modeling choices, appearing in both 2D and 3D simulations for isothermal and non-isothermal equations of state, with and without magnetohydrodynamics (MHD) (MacFadyen & Milosavljević, 2008; D'Orazio et al., 2016; Noble et al., 2012; Muñoz et al., 2019; Moody et al., 2019, , among others)

2. $0.05 \lesssim q \lesssim 0.2$: At intermediate mass ratios, the lump cannot be maintained and its associated 5-orbit accretion modulation vanishes. Accretion variability is dominated instead by the orbital period of the binary.

3. $q \lesssim 0.05$: As mass ratio decreases, so does the amplitude of accretion variability. For sufficiently low q, the variability vanishes entirely.

Additionally, for $q < 1$, simulations find that accretion occurs preferentially onto the smaller secondary SMBH. This has led to speculation that the secondary's mini-disk may be more luminous than the primary's and that, over long timescales, this preferential accretion may drive binaries towards $q = 1$ (e.g., Farris et al., 2014).

If the binary is on an eccentric orbit, the lump observed for $q \gtrsim 0.2$ circular binaries fails to form, leaving variability only on the binary orbital timescale. As binary eccentricity increases, the modulated accretion rate becomes "peakier," with a steep rise as the binary nears periapse and an exponential decay thereafter (Zrake et al., 2021), contrasting with the roughly sinusoidal modulation seen in circular binaries. (Siwek et al., 2023) find that eccentricity also impacts the preferential accretion in unequal-mass binaries, with moderate eccentricities $e \lesssim 0.4$ enhancing the preferential accretion and high eccentricities $e \gtrsim 0.6$ suppressing it.

1.3.2 Orbital Evolution

Another active area of research concerns the net torque on the binary, as this is essential to understanding how long binaries take to reach the GW inspiral phase or whether they do at all. Additionally, gas torques acting on the binary can change its orbital eccentricity over time, which has consequences for the accretion variability discussed earlier as well as for the gravitational waveform emitted from the binary.

Resonant gravitational interactions between the binary and the circumbinary disk excite spiral density waves at the Lindblad resonances (Goldreich & Tremaine, 1980). The gravitational torque exerted by the binary is positive on gas exterior to the binary and negative on gas interior to the binary. The net torque exerted on the disk at these resonances is positive, implying a net negative torque on the binary, driving it closer to merger. However, there is an additional, typically positive, torque contribution from the angular momentum accreted onto each of the binary components. For the fiducial $q = 1$, $H/R = 0.1$, $\alpha = 0.1$ case typical in the literature, the net torque is positive,

alarmingly implying that SMBHBs may actually be driven outward, never to merge (Muñoz et al., 2019).

The balance of these torques and the dependence of that balance on binary and disk properties has been the focus of several recent studies. Tiede et al. (2020) and Dittmann & Ryan (2022) found that the sign of the torque flips for thinner disk aspect ratios, with (Dittmann & Ryan, 2022) further finding that decreasing the viscosity further reduces the magnitude of the positive accretion torque at lower H/R, despite little dependence on viscosity at $H/R = 0.1$. Investigations of the mass ratio dependence find that the net torque on the binary becomes negative at low mass ratios, with the critical value of q being dependent on disk properties (Duffell et al., 2020; Dempsey et al., 2021).

There is also complex interplay between disk-binary interactions changing the binary's eccentricity and the binary's eccentricity changing the net torque experienced by the binary. It is observed that binaries which are initially low-eccentricity ($e \lesssim 0.1$) tend to circularize further, while more eccentric binaries are instead drawn to a critical eccentricity $e \sim 0.4$–0.5 (Zrake et al., 2021; D'Orazio & Duffell, 2021; Muñoz et al., 2019). The effect of eccentricity on the orbital evolution is more debated, with Zrake et al. (2021) and Muñoz et al. (2019) finding that the orbit expands for all e, while D'Orazio & Duffell (2021) find that circular binaries migrate outward and eccentric binaries migrate inward.

1.3.3 Reality is 3D and Other Considerations

The previous results nearly all stem from simulations considering a 2D, locally isothermal disk with a constant aspect ratio $H/R = 0.1$. However, real AGN disks are more complicated and more varied than this simple model can capture. We'll briefly review here results from select numerical and semi-analytic works which deviate from the fiducial model, as well as other relevant complications in running and interpreting SMBHB simulations.

Self-consistent modeling of the disk viscosity necessitates 3D MHD, and capturing general relativistic behaviors near the SMBHs further necessitates GRMHD. There have been a few GRMHD simulations exploring SMBHB accretion in recent years, finding broadly similar accretion mod-

ulation to that seen in 2D simulations but with preferential accretion which alternates from one SMBH to the other on orbital timescales, attributed relativistic effects (Bowen et al., 2018; Combi et al., 2022). The major drawback of GRMHD is that it is computationally expensive, with the works cited here running for just tens of binary orbits. As a result, GRMHD simulations are currently only able to probe short-term variability and cannot yet investigate the long-term behavior and orbital evolution of SMBHBs.

There are several 2D works which do explicitly evolve the energy equation in order to obtain a more robust lightcurve for the binary. Gas cooling is typically implemented via an optically thick blackbody prescription or a simple β-cooling prescription, where the gas temperature returns to an equilibrium value on a timescale $t_{\rm cool} = \beta\Omega_K^{-1}$, where Ω_K is the local Keplerian orbital frequency. Generally, the disk luminosity tracks the accretion rate (e.g., Tang et al., 2018; Westernacher-Schneider et al., 2022), though sufficiently slow cooling rates are found to circularize the disk cavity, suppressing accretion variability (Wang et al., 2023).

While accretion rate is widely used as a proxy for a lightcurve in SMBHB simulations, it is not certain that the observed luminosity of a system will so closely track variations of accretion rate. There are intermediate physical processes which must convert the change in accretion rate to a change in luminosity and the timescale this conversion occurs on is unclear. If it is short compared to the binary period, then the picture presented by numerical studies holds. But if the conversion takes a similar or longer time than the orbital period, then this may smooth out the variability, reducing the amplitude of the lightcurve modulation relative to that of the accretion.

Finally, many of the results seen in 2D simulations, especially the morphology of the gap/cavity, the mass ratio cutoffs for accretion variability regimes, and the net torque experienced by the binary, are likely to depend on the properties of the disk the binary is embedded in. Despite this, few works have considered aspect ratios thinner than 0.1 even though real AGN accretion disks are expected to have aspect ratios of 10^{-3}–10^{-2} (Krolik, 1999). Thinner disks are more expensive to simulate, as the spiral density waves are narrower, requiring finer resolution to accurately capture the gravitational torques, but this is a necessary step towards better understanding how SMBHBs

will evolve in their real environments.

The numerical studies in this dissertation utilize disk models based on the conventional Shakura-Sunyaev model (Shakura & Sunyaev, 1973), with aspect ratios consistent with those expected for real SMBH disks. This, in tandem with a focus on shock-borne variability, explores a significant piece of the puzzle of accreting SMBHBs, their evolution, and the EM signatures which may distinguish them from single-SMBH systems.

1.4 Dissertation Overview

Chapter 2 presents a numerical study of a $q = 0.01$ SMBHB with explicit thermal evolution of the circumbinary disk. The binary was embedded in an accretion disk whose initial conditions were calculated from the 1D steady-state configuration for a Shakura Sunyaev α-disk perturbed by a massive secondary. We monitored both accretion onto the individual binary components and the thermal emission inferred from our cooling prescription in order to calculate lightcurves for the system as a function of photon frequency. We found that the binary produced strong variability at all wavelengths with periods of order the binary orbital period. Variability was strongest in X-rays, driven by shocks from the secondary's accretion streams whipping into the edge of the gap. Additionally, the X-ray variability was anti-correlated with the UV variability, an observable feature distinct from single-AGN variability which could be used as an additional test of existing small-separation SMBHB candidates.

In Chapter 3, we examine a similar setup, but with a locally isothermal equation of state and a novel method of monitoring shock-borne emissions without explicit thermal evolution of the system. We embed our $q = 0.01$ binary in a newly-derived steady α-disk model, where the gas pressure is increased to mimic the inclusion of radiation pressure. To approximate the shock lightcurve, we monitor the kinetic energy dissipated by shocks and assume that this is instantaneously emitted as light. As in Chaper 2, we find that the shock-driven variability has a period of order the orbital period of the binary and that this shock-driven variability is out of phase with the accretion variability, implying again that cross-correlation studies of X-ray and UV lightcurves could be a useful

test of binary candidacy.

In Chapter 4, we investigate the portion of the SMBHB parameter space to which existing numerical predictions are applicable to observational efforts. We considered several relevant observational and modeling constraints and applied these to both a three-zone Shakura-Sunyaev α-disk model as well as the constant aspect ratio disk model commonly used in numerical studies of SMBHBs. We found that, for fiducial disk parameters, the gas-dominated binaries explored in simulations are only GW-detectable out to redshifts $z \lesssim 0.3$ and for binary masses $M \sim 10^8$ with orbital periods of $t_{\rm bin} \sim 10$ yr. Most detectable GW emission from SMBHBs will instead arise from close-separation binaries where the secondary is embedded in the inner radiation-dominated part of the disk, beyond the physical regimes tested by the majority of numerical simulations.

Finally, in Chapter 5, I review the results of the previous chapters and discuss future prospects in modeling and observing SMBHB signatures.

CHAPTER 2

Multiwavelength Correlated Variability From a Thermally-Evolving Supermassive Black Hole Binary

The following work was co-authored with Kayhan Gültekin and Mateusz Ruszkowski.

2.1 Abstract

Mergers of supermassive black holes are of profound importance in the evolution of supermassive black holes and their host galaxies, being a channel for mass and spin evolution of the black holes and being linked to the merger history of the host galaxy. The low frequency gravitational waves that these mergers and their precursor binaries will emit remain undetected by present-day gravitational wave observatories, and the sub-milliarcsecond separations involved in the binary phase leave them unobservable using current observational techniques that rely on spatial or spectral resolution of the binary. Here, we use a 2D numerical simulation of a close-separation (100 AU), low mass ratio ($q = 0.01$) supermassive black hole binary with realistic cooling and gas accretion prescriptions to look for periodic emission in optical, UV, and X-ray wavebands which can be used to identify supermassive black hole binaries using time-domain monitoring. We find strong variability across the electromagnetic spectrum with periods corresponding to the binary orbital time. In the X-rays, there is additional strong variability at integer multiples of the orbital frequency, with even multiples of the orbital frequency exhibiting doublet peaks in the Fourier power

spectrum. We further observe that the X-ray peaks are much broader than their optical and UV counterparts. There is also significant enhancement of the continuum X-ray emission over a single SMBH model due to shocks excited along the accretion streams of the minidisk and where they strike the inner and outer disks. These features may be used to identify binary SMBH candidates through both single-epoch observations and long-term time monitoring.

2.2 Introduction

It is expected that close ($\leq$ 0.1 pc) supermassive black hole (SMBH) binaries should exist given that nearly all massive galaxies have a SMBH at their center (Richstone et al., 1998) and that galaxy mergers are a regular occurrence in our universe. Following a galaxy merger, the two SMBHs will sink toward the galactic center through dynamical friction, become gravitationally bound, and harden their orbit by three-body interactions with stars (Begelman et al., 1980) and torques from the surrounding gas (Escala et al., 2004), until gravitational wave (GW) emission can take over and quickly bring the binary to coalescence. In addition to galaxy mergers, which are likely the only formation channel for $\sim$equal mass binaries, several alternative mechanisms have been proposed for the production of low-mass-ratio SMBH binaries. These include the presence of low-mass (10^2–10^4 $M_\odot$) SMBH seeds (Bellovary et al., 2011), in-situ growth of stellar mass BHs to intermediate mass black hole (IMBH) masses in the disk (McKernan et al., 2012), and disruption of IMBH-hosting globular clusters (Fragione & Capuzzo-Dolcetta, 2016; Fragione et al., 2018a; Arca-Sedda & Gualandris, 2018; Fragione et al., 2018b; Rasskazov et al., 2019). There are therefore a number of channels by which to form close-separation SMBH binaries and, correspondingly, produce SMBH mergers.

Understanding of the SMBH merger rate is a key part in answering a variety of questions regarding supermassive black holes and the galaxies which host them. SMBH mergers may be an important pathway for both the spin and mass evolution of SMBHs, especially for smaller, $\sim 10^6$ $M_\odot$ BHs (Sanchez et al., 2018). Some works have even suggested SMBH mergers as the principle mechanism behind the scaling relations between SMBH mass and various galaxy properties

(Jahnke & Macciò, 2011). SMBH mergers also emit gravitational waves, detectable by Pulsar Timing Arrays (PTAs) such as NANOGrav (Jenet et al., 2009) and upcoming space-based GW facilities such as *LISA* (Amaro-Seoane et al., 2017). Asymmetric GW emission (e.g., from SMBHs with misaligned spins) may also lead to a recoil of the merger product, kicking it out of the host galaxy and thereby influencing the BH occupation fraction of galaxies (Merritt et al., 2004).

The most straightforward way to answer these questions concerning the formation of SMBH binaries, the SMBH merger rate, and the implications of SMBH mergers is to make observations of binary SMBH systems. However, direct detection is impossible with current instruments given the tiny angular separations involved ($\sim 10^{-7}$ arcseconds for 10^{-3} pc physical separations at $z \sim 1$). One alternative, and the one to which the present work is relevant, comes from an analogy to protoplanetary disks, in which the presence of a planet in a protoplanetary system may be inferred from the effect it has on the disk, opening up gaps or holes via gravitational torques (Goldreich & Tremaine, 1980). For SMBH binaries, such a method would bridge the gap between future GW detections and current methods for detecting wide-separation unbound pairs through spatially resolving them (down to $\sim$1 kpc; Komossa et al., 2003; Comerford et al., 2012; Blecha et al., 2013; Foord et al., 2019), through HI absorption lines with different Doppler shifts implying the presence of a second relativistic jet (down to $\sim$few pc) (Rodriguez et al., 2009; Tremblay et al., 2016; Bansal et al., 2017), or through identifying spectrally distinct broad line emission regions (down to $\sim$0.1 pc) (Gaskell, 1996; Eracleous et al., 2012; Runnoe et al., 2017).

A preceding analytical work by Gültekin & Miller (2012) examined the observable consequences of gaps opened in an accretion disk by a secondary SMBH. First, they found that for a prototypical α-disk (Shakura & Sunyaev, 1973), the secondary will indeed open up a gap for reasonable properties of the binary. Further, they showed that the spectral energy distribution (SED) of such a system will possess a "dip" feature (see also Kocsis et al. 2012a; Noble et al. 2012; Tanaka et al. 2012; MacFadyen & Milosavljević 2008; Haiman et al. 2009a; Roedig et al. 2014), whose break wavelength and change in powerlaw slope can be used to infer the position and width of the gap, respectively. These, in turn, give the separation and mass ratio of the binary system. Thus,

observations of these "notched" SEDs can be used to not only identify candidate binary SMBH systems but also produce estimates of key properties of the binary.

The limitation of this method is that the dip feature cannot be uniquely attributed to a gapped-disk system, especially for the case of small mass ratios where the dip is very slight. However, it is also expected that such systems will have periodic variability across multiple wavelength regimes due to periodic modulation of accretion onto the secondary SMBH, with the specific variability frequencies depending on the parameters describing the binary (Valtonen et al., 2010; Graham et al., 2015a; Liu et al., 2015). A dip in the SED could therefore be used to identify candidate binary systems as well as make estimates of their mass ratios and separations, these parameters used to identify characteristic periodicities in optical, UV and X-ray wavelengths, and then follow-up observations made to look for the expected periodicity in order to confidently confirm or deny the presence of a SMBH binary. To this end, the aim of the present work is to produce a 2D simulation of a SMBH binary with realistic prescriptions for relevant physics and to use this simulation to demonstrate the existence of time-varying observables in SMBH binaries.

Section 2.3 of this paper discusses the methodology, specifically the simulation setup, physical prescriptions used, and the analysis routine used for time-domain analysis of the simulation. Section 2.4 presents the results of the simulation, showing the time-varying outputs to be discussed. Section 2.5 discusses these results and their implications for time-domain observability of SMBH binaries. Section 2.6 presents the conclusions from this work and discusses the future aims extending from this project. Appendices A.1 and A.2 detail tests of our numerical routines for gas accretion and radiative cooling, respectively.

2.3 Methods

We examine the evolution of a vertically-averaged (i.e., 2-dimensional) Shakura-Sunyaev disk surrounding a fixed-orbit SMBH binary. In particular, we wish to monitor time-varying properties which correspond to variable features in the observed emission from such a system. Here, we describe the implementation of the codeset utilized for this work, the various physics prescriptions

included in our model, the initial conditions used for our run, and the analysis methods used to obtain our results.

2.3.1 Simulation Setup

Our binary is initialized with the following fiducial parameters: primary SMBH mass of 10^8 $M_\odot$, secondary SMBH mass of 10^6 $M_\odot$, and separation of $100R_g$ (~ 100 AU), where $R_g = GM/c^2$ is the gravitational radius of the primary SMBH. We use $\alpha = 0.01$ for our α-viscosity, where the viscosity is computed as $\nu = \alpha c_s h$ (Shakura & Sunyaev, 1973). Here, c_s is the local gas sound speed, and h is the local disk scale height.

In terms of the gravitational wave features of this system, it has a chirp mass of $\mathscr{M}_c = 6.3 \times 10^6$ $M_\odot$, a symmetric mass ratio of $\eta = 9.8 \times 10^{-3}$, and a GW frequency of $f_{\rm GW} = 4 \times 10^{-6}$ Hz. This is simultaneously too high frequency for observation by present PTAs and below the planned frequency range for LISA, but represents a place in parameter space that can be detected with existing and near-future electromagnetic time-domain observations, such as LSST, Pan-STARRS, and the Zwicky Transient Facility.

A preceding work with SMBH binaries, Kocsis et al. (2012a), developed analytic solutions for the quasi steady-state radial structure of the disk for given binary parameters. They use a simple 1D (i.e., vertically and azimuthally averaged) Shakura-Sunyaev disk model, making the following assumptions: radial heat transport is negligible, viscosity follows an α-prescription, and that the sum of gas and radiation pressure supports the disk against vertical gravity. From this work, we take the radial surface density and temperature profiles corresponding to our binary parameters, shown in Figure 2.1, as our initial conditions for the disk gas.

The simulation is performed in a 2D cylindrical coordinate system, extending from 10–1000 R_g in radius and over the full 0 to 2π in azimuthal angle. The radial resolution is 0.39 R_g (~ 0.39 AU) and the azimuthal resolution is 0.0041 radians $= 0.23^\circ$, corresponding to a resolution of 0.41 R_g at the position of the secondary SMBH. These radial and azimuthal resolutions correspond to 39 and 41 gravitational radii of the secondary, respectively. These values are chosen in order to

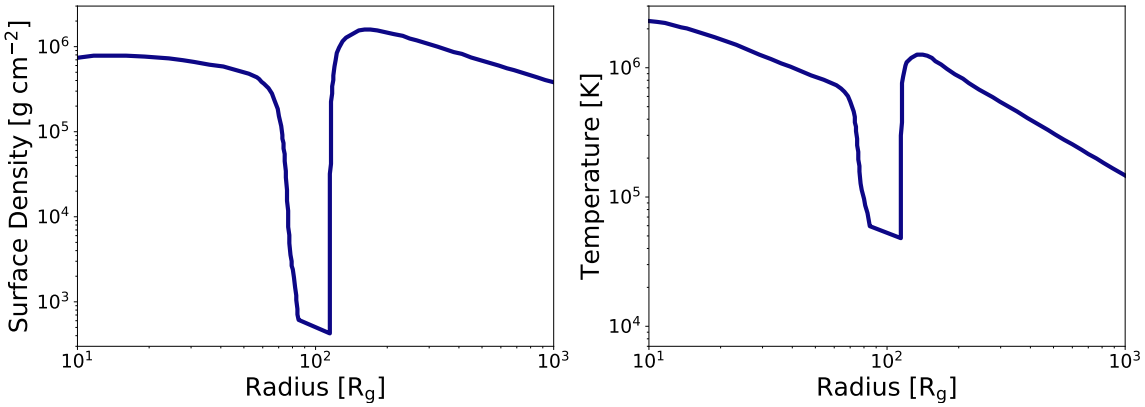


Figure 2.1: Initial radial profiles for disk surface density (*left*) and midplane temperature (*right*) based on the 1D analytic work by Kocsis et al. (2012a) for the quasi steady-state of a SMBH binary with our chosen parameters. The presence of a low density, low temperature gap at 100 R_g is clear and there is also visible enhancement of surface density and temperature at the gap edges, particularly at the outer edge.

adequately resolve the flow onto and within the secondary's mini-disk. Resolving the dynamics of gas within this region is important for identifying the high-frequency modes of variability which may result from the mini-disk flow.

We use a simple outflow condition for the inner radial boundary, which allows gas to freely leave the domain. For the outer boundary, we use an extension of the surface density and midplane temperature profiles from Kocsis et al. (2012a), with velocities set to Keplerian rotation. This use of a Keplerian outer boundary is justified as our outer boundary is far enough out that the deviations from Keplerian behavior due to torques from the secondary SMBH are minimal. We also use the wave-damping boundary condition from de Val-Borro et al. (2006) to keep the disk well behaved near the inner and outer radial boundaries.

We use an adiabatic equation of state,

$$p = (\gamma - 1)e, \tag{2.1}$$

where p is the pressure, e is the energy density of the gas, and $\gamma = 5/3$ is the adiabatic index for an ideal gas. We assume the system to be dominated by gas pressure, with no contribution from radiation pressure.

We grow the secondary's mass from zero to its initial mass of 10^6 $M_\odot$ over the course of the first twenty orbits of the simulation. We take this step, because the sudden presence of a massive object in a Keplerian disk can disturb the disk strongly enough to produce acoustic waves which linger for long times and modify the accretion onto the secondary SMBH (Zhu et al., 2011). Because we are interested in periodic accretion and emission in these systems, it is critical to ensure that there is no excitation of spurious waves which would produce periodic accretion signals in our analysis.

We run the simulation for 1000 orbits of the secondary SMBH about the primary, where $t_{\rm orb} = 2\pi\sqrt{a^3/GM_{\rm tot}} \sim 0.1$ yr. This allows for confident identification of periodicities on long timescales, allowing for multiple iterations of variability with periods on the order of 10-100 orbits. The smallest timescales we are interested in detecting periodicity on are 10^{-1} orbits, which is much longer than the output timestep of 10^{-3} orbits.

2.3.1.1 FARGO3D

FARGO3D is a publicly available magnetohydrodynamics code produced by Benítez-Llambay & Masset (2016). The code is capable of being run in parallel on both CPU and GPU systems. FARGO3D solves the continuity equations in a frame corotating with the secondary, allowing dramatic increases in the timestep and thereby speeding up the simulation of rotating systems like accretion disks. The base code includes routines to handle computations of gravitational forces and viscosity under the Shakura-Sunyaev α-prescription. For detailed descriptions of these built-in routines, we refer the reader to Benítez-Llambay & Masset (2016). In addition to these, we have produced routines for accretion of gas onto the SMBHs and cooling of the gas through a radiative emissions model. We summarize the workings of these and the basic principles of the gravity routines below.

2.3.1.2 Gravity

The disk at large is non-relativistic, and so we only consider Newtonian gravity for this work. Further, we neglect orbital evolution from gravitational wave emission as, for the binary parameters

chosen, the gravitational wave inspiral of the binary is insignificant over the timescales considered in this simulation. This can be determined by computing the ratio of the simulation time to the gravitational wave inspiral time,

$$\frac{t_{\rm sim}}{t_{\rm GW}} = \frac{512\pi}{5} N_{\rm orb} \tilde{r}^{-5/2} q (1+q)^{1/2} (1-f^4)^{-1}, \tag{2.2}$$

where $N_{\rm orb} = 10^3$ is the number of orbits in the simulation, $\tilde{r} = 10^2$ is the initial separation in units of R_g, $q = 10^{-2}$ is the mass ratio, and f is the fraction of the initial separation to which the orbit decays. For a decay to $f = 0.99$ and our binary parameters, this ratio is below unity, indicating that the orbit will decay by $< 1\%$ of the initial separation over the course of our simulation. In addition, because α-disks are Toomre stable (Toomre, 1964), we neglect disk self-gravity, considering only the BH-disk and BH-BH interactions.

In general, the acceleration due to gravity is computed for each cell as

$$\mathbf{g} = \mathbf{g_1} + \mathbf{g_2}, \tag{2.3}$$

where $\mathbf{g_1}$ is the gravitational acceleration from the primary SMBH and $\mathbf{g_2}$ is that of the secondary, with

$$\mathbf{g_i} = -\frac{GM_i}{r_i^2 + (\xi h)^2} \hat{\mathbf{r}}_\mathbf{i}. \tag{2.4}$$

Here, G is the gravitational constant, M_i is the mass of the i-th SMBH, r_i is the distance between the i-th SMBH and the cell of interest, $\hat{\mathbf{r}}_\mathbf{i}$ is a unit vector pointing from the i-th SMBH to the cell of interest, h is the scale height of the cell, and ξ is the fraction of the scale height by which the acceleration is softened. This softening by a factor proportional to the scale height solves two key issues. One, there is otherwise a singularity for the case $r_i = 0$. Two, we would otherwise overestimate the gravitational influence of the secondary on gas close to it, as the two-dimensional treatment of the disk means that cells experience a vertical average of the gravitational force (Masset, 2002). By softening the gravitational acceleration in this way, we account for this vertical averaging of the

potential over the height of the disk. We choose $\xi = 0.6$, following from considerations made by Duffell & MacFadyen (2013).

The scale height itself is computed as

$$h = (H/R)r, \tag{2.5}$$

where $H/R \sim 1.5 \times 10^{-3}$ is the aspect ratio of the disk and r is the radial coordinate in the simulation domain.

2.3.1.3 Gas Accretion

A key component of our simulations is tracking the accretion of gas onto the two SMBHs. The purpose of including accretion of gas onto the SMBHs is twofold: first, the removal of gas from the accretion disk is a natural part of the disk accretion flow; second, the mass accretion rate of an α-disk is intimately linked with its radiative emission, so tracking this property of the SMBHs will aid in our analysis of the binary's time-varying emission properties. Two methods are used for tracking accretion onto the SMBHs, one for the primary and another for the secondary, due to their locations within the grid. For the secondary, our methodology closely follows that of Nelson et al. (2000). In this, the black hole has a pre-defined accretion radius, $r_{\rm accr}$, from which it accretes gas, and accretion time, $t_{\rm accr}$, which defines the rate at which gas is removed from within $r_{\rm accr}$. We use an accretion radius of $\frac{1}{2}R_h$, where $R_h = a\,(q/3)^{1/3}$ is the radius of the secondary's Hill sphere, which denotes the region where the secondary's gravitational influence dominates over the primary's, with q being the mass ratio of the SMBHs and a their separation.

The fraction of mass removed from cells within $r_{\rm accr}$ is computed as

$$f_{\rm accr} = \frac{\Delta t}{t_{\rm accr}}, \tag{2.6}$$

where Δt is the simulation timestep. Following from Zhu et al. (2011), we set the accretion time

equal to the viscous timescale,

$$t_{\rm accr} = \frac{r^2}{\nu} = \frac{r^2}{\alpha c_s h}, \tag{2.7}$$

where r is the distance of a cell's center from the secondary SMBH, for cells within $r_{\rm accr}$. We show in Appendix A.1 that this routine obtains the correct result for the case of pressureless accretion onto a central point mass.

For the primary, due to its location beyond the inner boundary of the domain, we adopt a different means of tracking accretion. We track the mass flux across each radial boundary of cells, giving us the accretion rate throughout the simulation domain as a function of the distance from the center. The primary SMBH's accretion rate is then taken to be the mean accretion rate over the radii comprising the inner disk, 15–50 R_g.

The mass and momentum accreted onto the secondary from the disk is dynamically negligible on the timescales considered in this work. We therefore do not include the effects of these in the gravitational and orbital calculations of the simulation. However, the total accreted mass and the accretion rate of each SMBH are recorded for each timestep to be used in producing light curves during post-processing (see Section 2.3.2). We also track the total linear and angular momenta accreted onto each SMBH at each timestep. From these we find that the total linear momentum accreted onto the secondary over the course of the simulation is $\sim 2.5 \times 10^{43}$ g cm s^{-1}, which is much smaller than the momentum of the secondary on its initial orbit, $p_i = \Omega r M \sim \Omega a M \sim 6 \times 10^{48}$ g cm s^{-1}, supporting our decision to ignore the effects of momentum accretion on orbital evolution.

2.3.1.4 Heating

There are two major forms of heating in our simulations: shock dissipation and viscous heating. Shocks are handled using a von Neumann-Richtmyer artificial viscosity (see Benítez-Llambay & Masset 2016 for more detailed information). Viscous heating is implemented as

$$\frac{de}{dt} = \frac{1}{2\nu\Sigma}\left(\tau_{r,r}^2 + \tau_{\varphi,\rho}^2 + \tau_{r,\rho}^2\right) + \frac{2\nu\Sigma}{9}(\nabla\cdot\mathbf{v})^2, \tag{2.8}$$

where $\frac{de}{dt}$ is the rate of change of energy per unit volume, $\tau_{i,j}$ are the components of the viscous stress tensor, $\nu = \alpha c_s h$ is the kinematic viscosity, and $\nabla \cdot \mathbf{v}$ is the divergence of the velocity. Shock dissipation is the dominant heating mechanism where the influence of the secondary is important (within $\sim 200\, R_g = 2a$ of the primary SMBH). Beyond this, viscous heating dominates the thermal balance.

2.3.1.5 Cooling

Radiative cooling is essential for obtaining a realistic picture of electromagnetic emission from a binary SMBH system, given the high and variable temperatures expected in a system experiencing repeated shocks from accretion streams crossing the gap. Our radiative cooling method is based upon the Townsend (2009) exact cooling scheme. This scheme entails exact integration of an integrable cooling function in order to solve the cooling for a cell of some temperature over the course of a simulation timestep. Because of this, the Townsend scheme is exact and does not impose additional restrictions on the simulation timestep, providing distinct advantages over explicit and implicit solvers.

For our simulations, we use the realistic disk cooling function from Johnson & Gammie (2003),

$$\Lambda = \frac{16}{3}\sigma T^4 \frac{\tau}{1+\tau^2}, \tag{2.9}$$

which allows for a smooth transition between the optically thick and optically thin regimes. We calculate the optical depth as $\tau = \Sigma\kappa/2$, where κ is the Rosseland mean opacity. For this work, we consider both electron scattering, $\kappa_e = 0.4\,\mathrm{cm^2\ g^{-1}}$, and bound–free opacities (following Kramer's law at solar metallicity; $\kappa_{\mathrm{bf}} = 1.6 \times 10^{24} (\rho\ \mathrm{cm^3 g^{-1}})(T/\mathrm{K^{-1}})^{-7/2}\ \mathrm{cm^2\ g^{-1}}$, with $\rho = \Sigma/2h$). For the heating and cooling, scale height is computed as

$$h = \frac{c_s}{\Omega_K}, \tag{2.10}$$

where c_s is the thermal sound speed of the gas and Ω_K is the angular velocity of the gas assuming

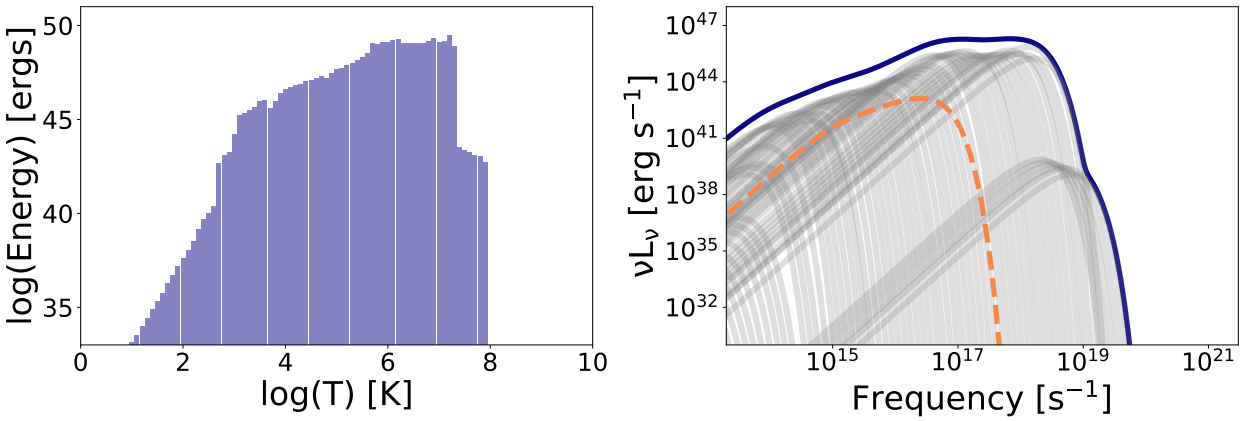


Figure 2.2: Construction of the system spectral energy distribution from cooling outputs. The example presented here is taken at $t = 950t_{\rm orb}$. *Left:* Radiated energy binned by temperature of the emitting cell for the full disk-minidisk system at a particular simulation timestep. *Right:* Planck spectral energy distributions computed for each temperature bin (grey lines), Shakura-Sunyaev SED computed for the minidisk based on the secondary SMBH's accretion rate (dashed orange line), and the resulting summed SED for the disk-minidisk system (purple line).

Keplerian motion.

We confirm in Appendix A.2 that the evolution of the gas temperature using this method follows the predicted analytic evolution to well within 0.1%.

For each simulation timestep, the cooling routine stores the energy radiated by each cell, binned by the *surface* temperature of the cell, where the surface temperature is

$$T_s = T\left(\frac{\tau}{1+\tau^2}\right)^{1/4} \tag{2.11}$$

and T is the code temperature, which represents the midplane. These temperature-binned radiated energies can then be used to create multi-wavelength lightcurves during post-processing (see Section 2.3.2).

2.3.2 Analysis Routines

The periods of variability in different photometric regimes are determined from two outputs of the simulation: the accretion rate onto the secondary SMBH and the temperature-binned radiated energies from the cooling routine.

For the cooling routine, we store the energy radiated by each cell in a timestep Δt binned by the initial surface temperature of the cell (Fig 2.2a). The total energy E_k in each temperature bin of central temperature T_k can then be used to construct a Planck spectral energy distribution (SED) for that bin as follows. The effective area A_k of a blackbody of temperature T_k emitting the same energy E_k over the simulation timestep Δt is given by

$$A_k = \frac{E_k/\Delta t}{\sigma T_k^4}, \tag{2.12}$$

where σ is the Stefan-Boltzmann constant. The SED for this energy bin is then computed as

$$\nu L_\nu = \nu A_k B_\nu(T_k) \tag{2.13}$$

where $B_\nu(T_k)$ is the Planck function for a blackbody of temperature T_k.

The sum of these individual Planck SEDs can then be used to reconstruct the total thermal SED of the system at each timestep (Fig. 2.2b). We separate the cooling outputs for cells within the secondary's Hill sphere from those outside it to allow for independent examination of the contributions from the mini-disk system and the rest of the disk.

For the accretion outputs, the accretion rate can be used to synthesize an α-disk SED at each timestep via the spectral modeling described in Shakura & Sunyaev (1973) (orange curve, Fig 2.2b). This can then be used as an additional source of variability information.

By producing SEDs for each timestep of the simulation, we create multiwavelength lightcurves of the system. We then perform Fourier transforms on portions of these lightcurves binned by photon frequency to identify the periods of variability in individual photometric regimes.

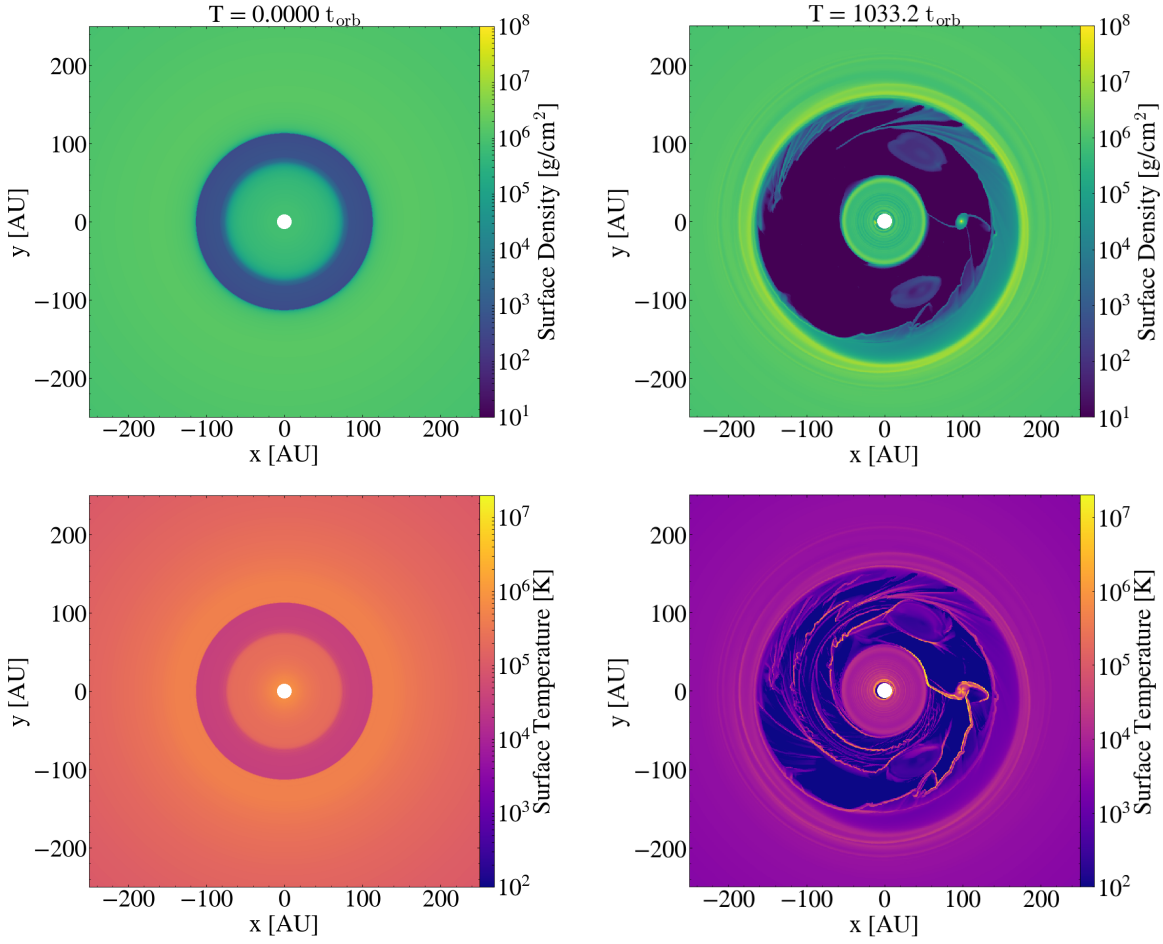


Figure 2.3: Evolution of the disk surface density and surface temperature from initial conditions to quasi-steady state. *Left:* Surface density (*Top*) and surface temperature (*Bottom*) initial conditions adapted from Kocsis et al. (2012a), including low-density gap near position of secondary. *Right:* Surface density (*Top*) and surface temperature (*Bottom*) in the quasi-steady state. Prominent features include a minidisk around the secondary SMBH, hot gas streams connecting the minidisk to the gap edges, and spiral density waves throughout the disk. Low-density clouds are also visible at the L4 and L5 Lagrange points, with hot, shocked streams throughout the gap.

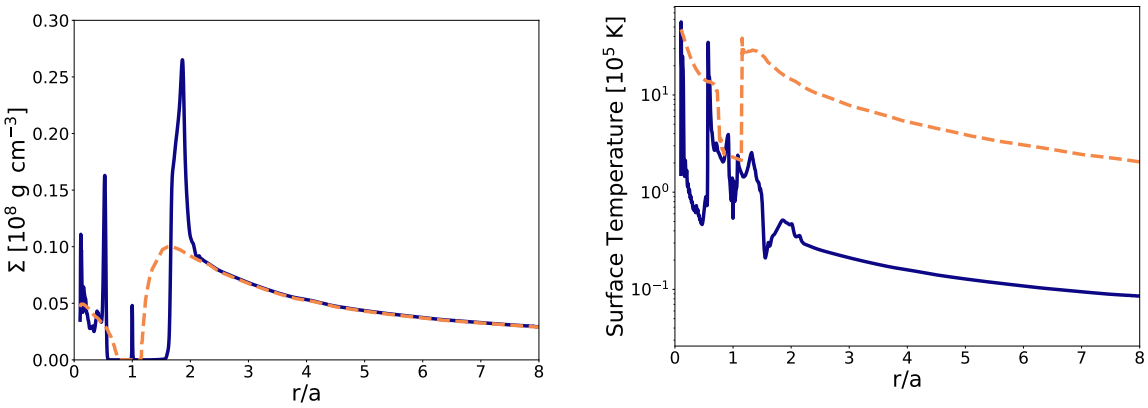


Figure 2.4: Azimuthally averaged surface density (*left*) and surface temperature (*right*) of the disk as a function of radius, with radius in units of the binary separation. The dashed orange curves show the initial radial profile, while the purple curves show the profile after 1000 binary orbits, averaged over 50 orbital times.

2.4 Analysis & Results

2.4.1 Disk Morphology

2.4.1.1 Surface Density

Our simulations begin with an azimuthally symmetric disk, with a gap about the radial position of the secondary SMBH (Fig. 2.3, left). The presence of the secondary quickly breaks this azimuthal symmetry, and a quasi-steady state is eventually reached (Fig. 2.3, right). In this state, the gap has widened, a minidisk has formed around the secondary SMBH, connected by accretion streams to the gap edges, and spiral density waves have been excited throughout the disk.

The top panel of Figure 2.4 shows the surface density profile from initial conditions compared to the time- and azimuthally-averaged surface density profile at 1000 binary orbits. The time-averaging is carried out over 50 binary orbits. In the late-time quasi-steady state, the outer and inner disk density profiles become "peakier" at the gap edges. The inner disk sharply truncates at $r \sim 0.5a$ while the outer disk truncates around $r \sim 2a$. This truncation of the outer disk at $r \sim 2a$ is similar to the results of MacFadyen & Milosavljević (2008), who found that the disk surrounding an equal-mass SMBH binary truncated at $r \sim 2a$. The gap between the inner and outer disk contains essentially no fluid, besides the minidisk around the secondary SMBH and thin accretion streams

connecting the minidisk to the inner and outer disks. The gap widens from $\sim 0.4a$ in the initial conditions from Kocsis et al. (2012a) to $\sim a$ in the quasi-steady state. Besides this pushing out and steepening of the surface density at the outer gap edge, the profile of the outer disk remains very close to the initial conditions.

2.4.1.2 Surface Temperature

Surface temperature is computed as defined in section 2.3.1.5. From Figure 2.3, it can be seen that the disk surface temperature is much lower in our steady state than in the initial conditions from Kocsis et al. (2012a). Our full 2D modeling of the system does, however, result in the production of persistent shocks in streams of gas in the gap, particularly along the streams connecting the minidisk to the inner and outer disks. These shocks contribute substantially to the emission of the system, dominating the X-ray emissions, as discussed in more detail in Section 2.4.3.

The bottom panel of Figure 2.4 shows the change in radial profile of the surface temperature between our initial conditions and quasi-steady state. The difference in temperature in the inner and outer disks between these times is a factor of ~ 30, which we attribute to the difference in how cooling is handled between our simulations and the work of Kocsis et al. (2012a). In Kocsis et al. (2012a), the opacity is assumed to always be dominated by electron scattering, while we additionally include the contributions from bound-free opacity, which significantly reduces the cooling time, particularly for temperatures corresponding to the regions affected in Figure 2.4. Despite the change in magnitude, it remains visible that the shape of the surface temperature profile is retained in both the inner and outer disks between these two works.

2.4.2 Accretion onto the Black Holes

Figure 2.5 shows the accretion rate onto each SMBH as a function of time for the last 5 orbits. Both exhibit periodicity, though this is much more pronounced for the primary SMBH. The secondary sustains a super-Eddington accretion rate at around $4\dot{M}_{\rm Edd}$, while the primary oscillates between $\sim (0.06\text{–}0.08)\dot{M}_{\rm Edd}$. Here we have defined $\dot{M}_{\rm Edd} = L_{\rm Edd}/\eta c^2$, with the radiative efficiency

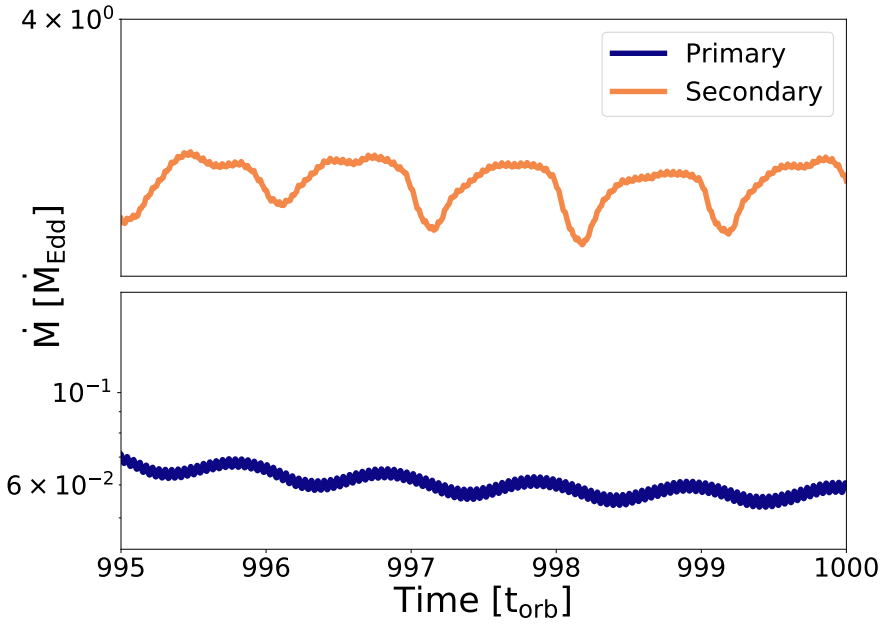


Figure 2.5: Late-time mass accretion rate onto each SMBH, scaled to that SMBH's Eddington accretion rate (assuming a radiative efficiency of 0.1). For the primary SMBH, boxcar smoothing over 10 orbital times has been applied. Accretion onto each BH exhibits oscillatory behavior, with a larger relative amplitude for the primary SMBH than for the secondary.

$\eta = 0.1$. Notably, this puts both black holes as accreting at a similar physical rate.

Figure 2.6 shows the Fourier transform of the accretion rates in Figure 2.5. Both the secondary and primary SMBHs show a distinct peak in their Fourier power spectra at the orbital frequency of the binary, as well as peaks of descending strength at integer multiples of this, though these are weaker relative to the principal peak for the primary, indicating a difference in how accretion onto each SMBH is modulated.

2.4.3 Electromagnetic Emission

Figure 2.7 shows simultaneously the system SED every 10^{-3} orbital times over the course of 10 orbits, displaying the typical variation in the SED. We note that the magnitude of the variability generally increases with photon energy. For frequencies below $\sim 10^{16}$ Hz (wavelengths longer than ~ 300 Å), the emission is disk-dominated, with higher frequencies primarily emitted from higher temperature regions within the disk. Broadly, the disk increases in temperature as one

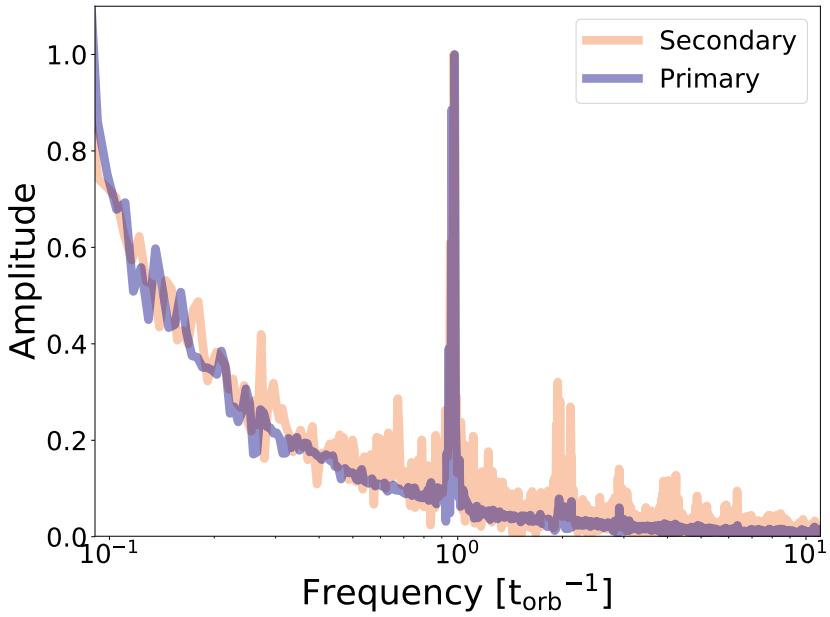


Figure 2.6: Fourier transforms of the accretion rates shown in Fig 2.5. Each Fourier power spectrum is normalized to the peak at $1/t_{orb}$. The secondary exhibits additional descending peaks at integer multiples of this principal frequency.

moves inward (Fig 2.4, bottom panel). The magnitude of variability therefore increases for gas in closer proximity to the binary, which shows that this variability is primarily driven by torques exerted on the gas by the binary.

Of interest to observers is how this variability looks in time at a particular photon frequency. To this end, Figure 2.8 shows the lightcurves and corresponding Fourier transforms for the monochromatic power at 5100 Å (optical), 1500 Å (ultraviolet), and 40 keV (X-ray). The strongest variability in all three wavelengths is at the orbital frequency of the binary. The X-ray also has strong variability on integer multiples of the orbital frequency, which are visible in the lightcurve (Fig. 2.8, third from top). While the optical and UV also show peaks at these integer multiple frequencies, as well as at two lower frequencies, these are much weaker than the principal peak at the binary orbital frequency.

The similarity between the optical and UV power spectra and, contrastingly, their differences from the X-ray power spectrum, hints that the optical and UV variability have the same or similar physical origin, while the X-ray variability arises from a separate process or multiple processes.

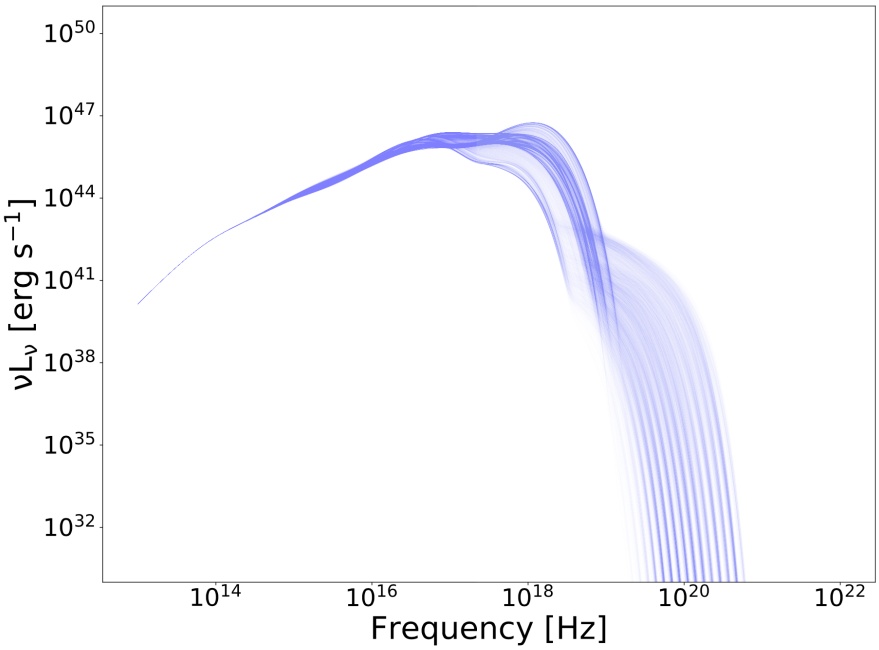


Figure 2.7: Variability of the system's spectral energy distribution. Each individual line shows the system SED every 10^{-3} orbits over the course of 10 orbital times. Darker regions thus correspond to a higher density of SED states and thus more time spent at that value. The spread in power at a given photon frequency indicates the magnitude of variability at that frequency.

We also note the similarity between the optical and UV power spectra with the primary SMBH's accretion rate power spectrum, as well as between the X-ray power spectrum and the secondary's accretion rate power spectrum (compare top panel of Fig. 2.8 to Fig. 2.6).

The temperatures needed to achieve significant X-ray production only occur in the shocks within the gap, particularly along the streams connecting the minidisk to the inner and outer disks. Meanwhile, the UV, optical, and longer wavelength emission are dominantly produced in the inner and outer disks. Therefore, it seems likely that the difference in Fourier power spectra between the X-ray and other wavelengths arises from differences in how torques from the binary impact the disk versus the accretion streams of the minidisk.

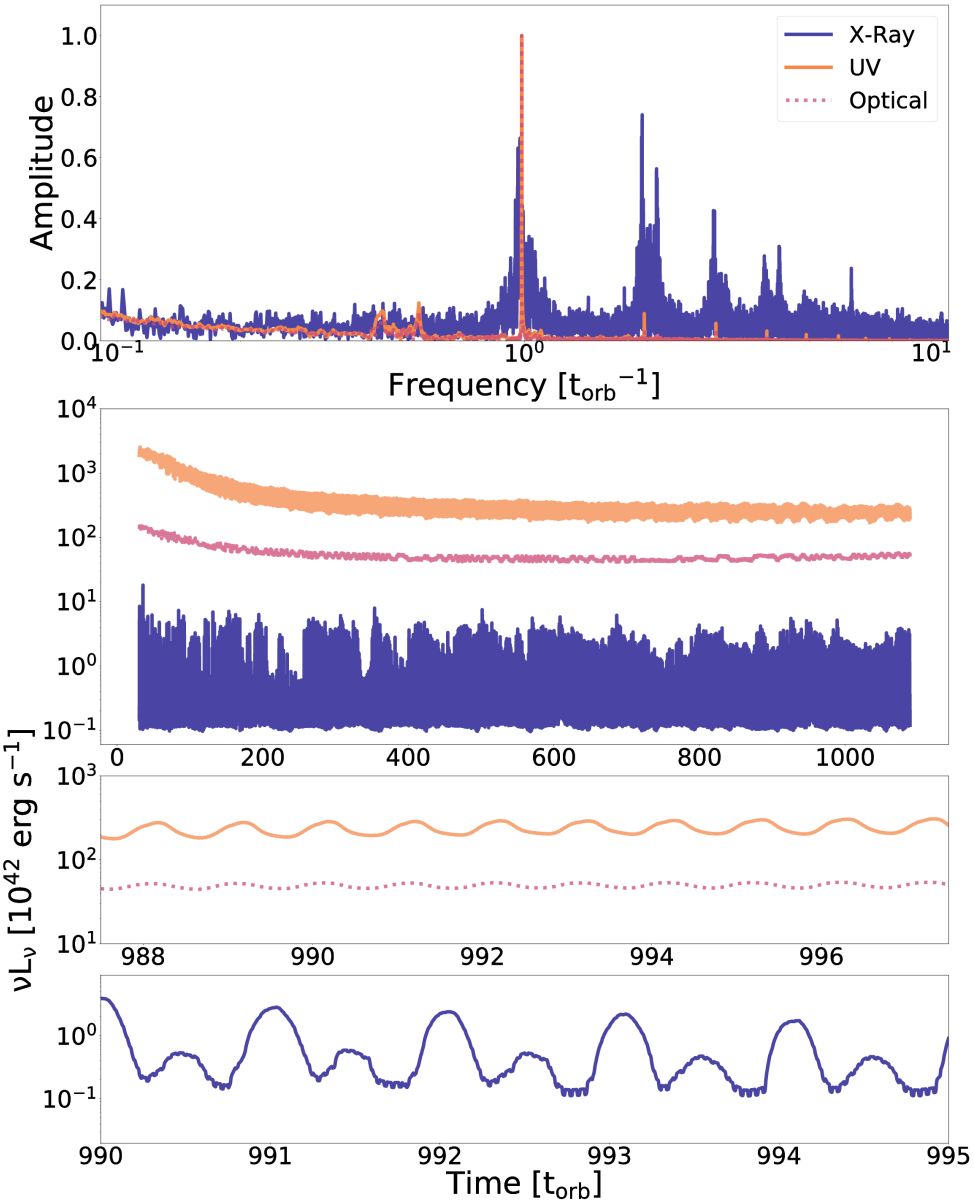


Figure 2.8: A more detailed look at the system variability at specific photon frequencies. *Top:* Fourier transform of the 5100 Å (optical, red dashed), 1500 Å (UV, orange), and 40 keV (X-ray, purple) lightcurves, normalized to the peak at the orbital frequency for each photon energy. All three show a strong peak at the orbital frequency of the binary, with the X-ray additionally possessing strong peaks of descending power at integer multiples of the orbital frequency. The optical and UV possess a similar series, though much weaker relative to the peak at the orbital frequency. The optical and UV additionally possess two peaks at lower frequencies, spaced around half the orbital frequency. We discuss the origins of these in Section 2.5.1. *Second from Top:* Optical, UV, and X-ray light curves, shown over the full simulation duration. The light curves have been smoothed over $0.1t_{\rm orb}$ to highlight the modes on the order of the orbital frequency, suppressing extremely high frequency modes not of interest to this analysis. *Third from Top:* Optical and UV lightcurves, zoomed in on a timescale where the strongest variability patterns are easily visible. *Bottom:* X-ray lightcurves, zoomed in on a timescale where the strongest variability patterns are easily visible.

2.5 Discussion

2.5.1 Origins of Electromagnetic Variability

For the X-rays, variability occurs only on frequencies corresponding to integer multiples of the binary orbital frequency. The only gas which meaningfully contributes to X-ray emission is shocked gas within the gap, particularly along the accretion streams of the minidisk and where these interact with the inner disk. Examination of the surface temperature in time reveals a periodic "whipping" of the accretion streams. Whipping of the outer stream produces the rippling stream observed southward of the minidisk in the bottom right of Fig 2.3. Whipping of the inner arm produces the shocked hotspot on the edge of the inner disk. This arm whips into the inner disk on roughly the orbital time, with a smaller whipping midway between these. These are the primary causes of the first two peaks of the X-ray Fourier power spectrum in the top of Fig 2.8. Examination of the X-ray light curve in the bottom panel of Fig. 2.8 shows that there are major peaks every half orbit, alternating between brighter, wider peaks, and dimmer, narrower peaks. These, respectively, correspond to the large and small whipping observed in the inner accretion stream. We also note that the even peaks (twice and four times the orbital frequency of the secondary) of the X-ray Fourier spectrum are double-peaked, while the optical and UV counterparts are single-peaked.

In the optical and UV, the peak at the orbital frequency dominates over all others in the Fourier spectrum. There is still a descending series at integer multiples of the orbital frequency, though it is substantially suppressed compared to the same series in the X-ray. In addition, there are two peaks positioned roughly evenly about half the orbital frequency of the binary.

2.5.2 Observational Consequences

There presently are no known SMBH binaries at the close separations examined in this work. It is therefore of strong interest to examine our results in the context of electromagnetic signatures that may aid observers in identifying these types of systems. We separate this into discussion of continuum features of the SED and time-domain variability.

2.5.2.1 Variability

Our simulations find strong variability at the orbital frequency for all wavelengths relevant to observations of AGN systems. So if one has an estimate for the orbital time then one can search for periodicity on just this timescale to confidently confirm or deny a binary's presence. In particular, one can improve confidence in this determination by either searching in multiple wavebands for the orbital periodicity since this mode appears in all of our monochromatic lightcurves, or by searching the X-ray for the power spectrum sequence at integer multiples of the orbital frequency, since this is the waveband where this feature is most prominent. Searching for multiple correlated frequencies in this manner strongly decreases the incidence of false alarms associated with red noise in data which is sampled for only a few cycles of a single frequency (Vaughan et al., 2016).

2.5.2.2 Continuum Features

The SED dip feature expected near 10^{15} Hz due to the disk gap is heavily suppressed in our observations (see Figs. 2.9, 2.2). As seen in past works (e.g., Farris et al. (2015)), this appears to be due to a combination of tidal heating at the gap edges and emission from shocks within the gap working to "fill in" the lost emission (see bottom panel of Fig 2.4 for visual of temperature enhancement near and within the gap). This indicates that this feature may be masked in observations both for high mass ratios as examined in Farris et al. (2015) as well as at low mass ratios as explored in this work.

While the SED dip is largely washed out, we do see significant enhancement of emission over standard α-disk predictions starting in the soft X-ray and continuing up to quite hard X-rays (~ 100 keV) (Fig 2.9). This X-ray enhancement from shocked gas has been seen in past works (e.g., Farris et al. (2015); Noble et al. (2012); Sesana et al. (2012)). We agree with the conclusions of Farris et al. (2015) that this makes a better continuum signature of the presence of a binary than does the SED dip, though it does not clearly produce predictions of the binary parameters as observing the dip would.

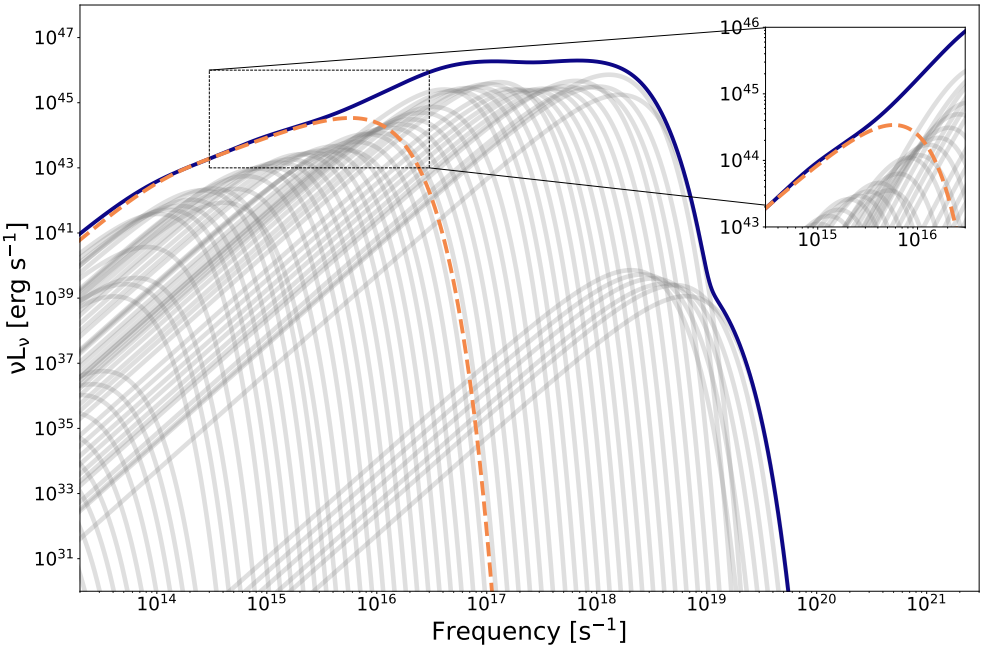


Figure 2.9: Comparison of simulation SED (solid purple line) to standard solution for an α-disk around a single SMBH (dashed orange line). The single SMBH SED is computed for a 10^8 $M_\odot$ black hole accreting at the Eddington rate. It can be seen that this single black hole SED falls off at around 10^{16} Hz, while the simulation SED for the binary case continues on until around 10^{19} Hz (~ 40 keV). An inset shows a zoom on the point of divergence between the two SEDs.

2.5.3 Additional Considerations

A key simplification of our setup is the lack of radiation pressure, despite the innermost regions of α-disks, where our binary is embedded, being radiation pressure dominated. Radiation-dominated disks are thermally unstable, which makes simulating them intractable in 2D, where the instability leads to thermal runaway which drives the simulation timestep to zero. In real disks and 3D simulations, this instability may lead to unique variability patterns different than those observed in this gas-dominated simulation (Ross et al., 2017; Habibi & Abbassi, 2019). Despite this, the continuum and time-domain signatures observed here should remain applicable to binaries at larger separations, embedded in the gas-dominated portion of the disk. While these wider separations are less likely to be simultaneously detectable with GWs, identifying and studying binaries throughout their evolution is essential to understanding which binaries eventually enter the GW-detectable regime and how.

2.6 Conclusion

We performed a 2D, Eulerian hydrodynamic simulation of a non-isothermal, non-self-gravitating, viscous gapped accretion disk around a low-mass-ratio SMBH binary on a fixed orbit. We examined the properties of the system in the quasi-steady state, with a focus on the observable electromagnetic emission from the system.

Our main findings can be summarized as follows.

1. The radial profile of surface density in the quasi-steady state qualitatively agrees with past numerical works, with a sharp rise near the gap edges and a gap width comparable to the binary separation. The trend at large radii agrees with the analytically-derived initial conditions. While the simulated temperature profile is considerably cooler than the initial conditions, the proportionality to radius in both the inner and outer disks remains close to the preceding analytic result.

2. The mass accretion rate onto each black hole is comparable in magnitude, with a sub-Eddington rate onto the primary and super-Eddington onto the secondary. The latter is in part be due to the neglect of radiation pressure as well as the large accretion radius chosen for the secondary SMBH due to the finite resolution of the simulation. The accretion rate onto each SMBH is variable, with Fourier power spectrum peaks of the secondary correlating with the peaks observed in the X-ray lightcurve's Fourier transform, indicating a common physical cause between modulation of the accretion rate and the luminosity.

3. The SED dip due to missing emission from the gap predicted by analytic works is suppressed due to emission from tidally heated gap edges and shocked gas within the gap. This implies greater difficulty in the use of this feature to identify candidate binaries in continuum observations of AGN.

4. There is significant enhancement of continuum emission in soft through hard X-rays over the predictions of the Shakura-Sunyaev model for a single SMBH system. This feature may

be used to identify binary SMBH candidates from observations of their continua.

5. There is strong variability across the electromagnetic spectrum at the orbital frequency of the binary. In X-rays, there are additional strong peaks at integer multiples of this frequency. This makes X-rays a particularly promising regime for observational detection of these systems by searching for this peak series in the power spectrum of an AGN's lightcurve.

In future works we will primarily investigate the effects of the binary parameters (mass ratio, separation, and primary mass) on the resulting variability and continuum properties of the system. This will include systems simultaneously observable by both PTA and long-term electromagnetic monitoring. Another area of possible future work is to relax some of the assumptions we have made, such as the lack of radiation pressure, and the use of α-viscosity to emulate the viscosity from MHD turbulence. A forthcoming work will provide analysis of the torques in this system to explore the "whipping" of accretion streams that cause the variability in our system's emission.

2.7 Acknowledgements

We acknowledge helpful discussions with: Aleksandra Kuznetsova, for recommending the FARGO3D code for this work and for valuable insights in troubleshooting certain numerical issues during development of the routines used for this work; Jaehan Bae, for discussions regarding boundary conditions in FARGO3D and cooling methods for disk simulations; Ryan Farber, for help with implementation of the cooling scheme used in this work; and Adi Foord, for assistance in design of the figures.

This research was supported in part through computational resources and services provided by Advanced Research Computing at the University of Michigan, Ann Arbor. Additional resources supporting this work were provided by the NASA High-End Computing (HEC) Program through the NASA Advanced Supercomputing (NAS) Division at Ames Research Center. This work was funded in part by Michigan Space Grant Consortium, NASA grant #NNX15AJ20H.

KG acknowledges support for this work provided in part by the National Aeronautics and

Space Administration through Chandra Award Numbers TM8-19007X , GO7-18087X, and GO8-19078X issued by the Chandra X-ray Center, which is operated by the Smithsonian Astrophysical Observatory for and on behalf of the National Aeronautics Space Administration under contract NAS8-03060.

MR acknowledges NSF grant AST 1715140. MR thanks the Aspen Center for Physics and the Kavli Institute for Theoretical Physics at the University of California at Santa Barbara, where part of this work was performed. The Aspen Center for Physics is supported by National Science Foundation grant PHY-1607611. This research was supported in part by the National Science Foundation under Grant No. NSF PHY-1748958.

CHAPTER 3

Shock-Driven Periodic Variability in a Low-Mass-Ratio Supermassive Black Hole Binary

This chapter appears in the Monthly Notices of the Royal Astronomical Society, Volume 527, Issue 3, pp.6569 (Whitley et al., 2024). This work was co-authored with Aleksandra Kuznetsova, Kayhan Gültekin, and Mateusz Ruszkowski. The paper is reproduced here with minor stylistic revisions.

3.1 Abstract

We investigate the time-varying electromagnetic emission of a low-mass-ratio supermassive black hole binary (SMBHB) embedded in a circumprimary disk, with a particular interest in variability of shocks driven by the binary. We perform a 2D, locally isothermal hydrodynamics simulation of a SMBHB with mass ratio $q = 0.01$ and separation $a = 100\ R_g$, using a physically self-consistent steady disk model. We estimate the electromagnetic variability from the system by monitoring accretion onto the secondary and using an artificial viscosity scheme to capture shocks and monitor the energy dissipated. While the spectral nature of these variability sources cannot be investigated in detail in an isothermal setup, disk luminosity tracks accretion rate and high-Mach-number shocks can emit at X-ray energies. Thus, we consider accretion in our simulation as a proxy for optical/UV emission, where typical AGN accretion disks are brightest, and shocks as

a proxy for X-ray emission. The SMBHB produces a wide, eccentric gap in the disk, previously only observed for larger mass ratios, which we attribute to our disk model being much thinner ($H/R \approx 0.01$ near the secondary) than is typical of previous works. The eccentric gap drives periodic accretion onto the secondary SMBH on a timescale matching the orbital period of the binary, $t_{\rm bin} \approx 0.1$ yr, implying that the variable accretion regime of the SMBHB parameter space extends to lower mass ratios than previously established. Shocks driven by the binary are periodic, with a period matching the orbital period, and the shocks are correlated with the accretion rate, with peaks in the shock luminosity lagging peaks in the accretion rate by $0.43\,t_{\rm bin}$. We propose that the correlation of these quantities represents a useful identifier of SMBHB candidates, via observations of correlated variability in X-ray and UV monitoring of AGN, rather than single-waveband periodicity alone.

3.2 Introduction

Since most galaxies are host to a supermassive black hole (SMBH) (Kormendy & Ho, 2013) and galaxy mergers are a regular occurrence (Lotz et al., 2011), it is expected that there should exist a population of post-merger galaxies containing a supermassive black hole binary (SMBHB) (Begelman et al., 1980). These binaries are a necessary precursor to SMBH mergers, and both binaries and mergers are sources of gravitational waves (GWs) which may be detected by Pulsar Timing Array (PTA) collaborations and the upcoming Laser Interferometer Space Antenna (LISA) mission (Amaro-Seoane et al., 2017), respectively. While there is no conclusive detection yet for a continuous-wave GW signal of an individual binary (Arzoumanian et al., 2023; Agazie et al., 2023a; Antoniadis et al., 2023a), several PTA collaborations have recently reported detection of a nanohertz gravitational wave background (GWB), consistent with what would be produced by a population of SMBHBs (Agazie et al., 2023c,d; EPTA Collaboration et al., 2023; Antoniadis et al., 2023b; Reardon et al., 2023a,b; Xu et al., 2023).

These discoveries and future continuous-wave GW detections of individual binaries can best be used for astrophysical inference when combined with electromagnetic (EM) observations, ne-

cessitating the development of methods for identifying and studying candidate SMBHBs with EM data alone. At wider separations, candidate multiple-SMBH systems can be identified through spatially resolving them (down to $\sim$1 kpc; Komossa et al., 2003; Comerford et al., 2012; Blecha et al., 2013; Foord et al., 2019), through HI absorption lines with different Doppler shifts implying the presence of a second relativistic jet (down to $\sim$few pc) (Rodriguez et al., 2009; Tremblay et al., 2016; Bansal et al., 2017), or through identifying spectrally distinct broad line emission regions (down to $\sim$0.1 pc) (Eracleous et al., 2012; Runnoe et al., 2017). However, at the very close ($\ll 1$ pc) separations most relevant to multimessenger studies with GWs, we rely on searches for active galactic nuclei (AGN) with periodically-modulated lightcurves (Graham et al., 2015b; Liu et al., 2019, 2020; Chen et al., 2020, among others). Unfortunately, even single-SMBH AGN are intrinsically variable sources, such that distinguishing periodicity from stochastic variability requires observing many cycles of the hypothetical period (Vaughan et al., 2016). It is important, then, to understand the properties of binary-induced EM periodicity which distinguish it from other sources of AGN variability.

A great deal of numerical simulations have been performed to understand the nature of SMBHB variability and evolution, investigating trends with binary mass ratio, separation, and eccentricity, as well as with disk temperature and viscosity (MacFadyen & Milosavljević, 2008; D'Orazio et al., 2013; Farris et al., 2014, 2015; D'Orazio et al., 2016; Tang et al., 2017, 2018; Moody et al., 2019; Tiede et al., 2020; Duffell et al., 2020; Westernacher-Schneider et al., 2022; D'Orazio & Duffell, 2021; Derdzinski et al., 2021).

The vast majority of the existing literature has used a locally isothermal equation of state, with accretion rate onto the binary components being used as the proxy for EM variability. However, Tang et al. (2018) have shown in a non-isothermal simulation that shock-heating of the cavity wall produces significant periodicity at high energies. This shock-induced periodicity can still be monitored in locally isothermal simulations via shock capturing, as binary-induced shocks are still present and dissipating energy, offering a second proxy for EM variability to analyze alongside accretion rates.

A particularly interesting case to examine is low-q SMBHBs. The majority of galaxy mergers are unequal-mass, and thus are expected to produce unequal-mass SMBHBs, with the caveat that smaller BHs are likely to form binaries less efficiently. Additionally, there are other proposed formation channels for low-q SMBHBs, such as the presence of low-mass (10^2–10^4 $M_\odot$) SMBH seeds (Bellovary et al., 2011), in-situ growth of stellar mass BHs to intermediate mass black hole (IMBH) masses in the disk (McKernan et al., 2012), and disruption of IMBH-hosting globular clusters (Fragione & Capuzzo-Dolcetta, 2016; Fragione et al., 2018a; Arca-Sedda & Gualandris, 2018; Fragione et al., 2018b; Rasskazov et al., 2019). However, it has been found previously that accretion onto the binary components becomes steady for $q < 0.05$ (D'Orazio et al., 2016). It is of interest, then, to determine whether periodic shocks also vanish for low-q SMBHBs, or whether the parameter space for EM-variable SMBHBs extends to lower mass ratios than previously established.

In this work, we perform a 2D hydrodynamic simulation of a $q = 0.01$ SMBHB and examine its implied variable electromagnetic properties via monitoring of both accretion and shocks. Shock capturing is performed using an artificial viscosity to both identify shocks and calculate the energy dissipated by them (Von Neumann & Richtmyer, 1950). Further, we relax the common assumption of constant disk aspect ratio in favor of a physically self-consistent disk model in order to better reproduce the real environments of these systems.

This paper is organized as follows. In Section 3.3, we describe the simulation setup, including the models used for the disk, gravity, accretion, and shock capturing. Section 3.4 presents our analysis of the disk dynamics and morphological evolution and our monitored accretion rate and shock outputs. We discuss the implications of these results in Section 3.5, in particular the dynamical and morphological differences from past works at this mass ratio (§3.5.1) and EM observables (§3.5.2). Section 4.5 summarizes our findings. Appendix B.1 provides a derivation for the disk model used in this work.

3.3 Methods

In this section, we describe the setup of the numerical simulation performed for this work. We review the initial conditions used for the system, the physics included in the simulation, and methodology for monitoring accretion and shock dissipation, which will serve as proxies for electromagnetic variability in our analysis.

3.3.1 FARGO3D

The simulations run for this work were performed on a two-dimensional, Eulerian, cylindrical grid using the *FARGO3D* code (Benítez-Llambay & Masset, 2016). *FARGO3D* solves the hydrodynamics equations

$$\frac{\partial \Sigma}{\partial t} + \nabla \cdot (\Sigma \mathbf{v}) = 0, \tag{3.1}$$

$$\Sigma \left(\frac{\partial \mathbf{v}}{\partial t} + \mathbf{v} \cdot \nabla \mathbf{v} \right) = -\nabla P - \Sigma \nabla \Phi + \nabla \cdot \Pi, \tag{3.2}$$

where Σ is the surface density, $\mathbf{v}$ is the fluid velocity, $P = \Sigma c_s^2$ is the isothermal pressure with c_s the isothermal sound speed, Φ is the gravitational potential, and Π is the viscous stress tensor. We use *FARGO3D*'s built-in α-prescription to set the viscosity as $\nu = \alpha c_s H$ (Shakura & Sunyaev, 1973), where H is the local scale height of the disk.

For the transport step in the azimuthal direction, *FARGO3D* employs the FARGO orbital advection algorithm (Masset, 2000), which greatly increases the solution accuracy and allowable simulation timestep for systems dominated by rotation, such as accretion disks.

3.3.2 Disk Setup

Our simulated domain is that of a disk centered on a primary SMBH with mass $M_1 = 10^8\ M_\odot$ and extends from $R_{\rm min} = 10\ R_g$ to $R_{\rm max} = 1000\ R_g$, where $R_g = GM_1/c^2$ is the gravitational radius of the primary SMBH. The secondary SMBH has mass $M_2 = 10^6\ M_\odot$ and is placed at a separation

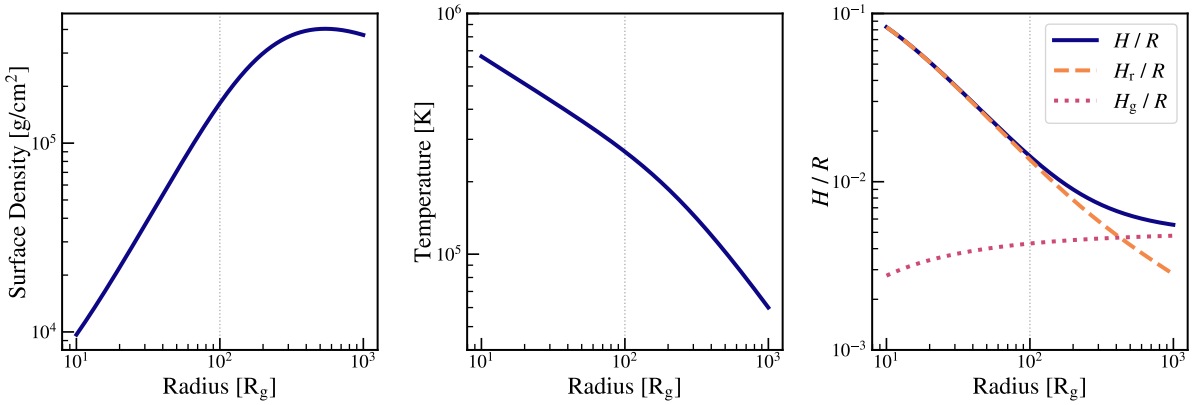


Figure 3.1: The initial conditions used for the simulation, calculated from the disk model described in Section 3.3.2. The vertical dotted line on each panel shows the position of the secondary SMBH. For H/R (*solid purple*), H_r/R (*dashed orange*) and H_g/R (*dotted magenta*), where $H_r^2 \equiv P_r/(\Sigma\Omega_K^2)$ and $H_g^2 \equiv P_g/(\Sigma\Omega_K^2)$, are also plotted to illustrate the relative contributions of radiation and gas pressure, respectively, throughout the disk.

$a = 100\,R_g$ from the primary, resulting in a binary orbital timescale $t_{\rm bin} \approx 0.1$ yr. We use the torque-free boundary conditions described by Dempsey et al. (2020) for our inner boundary, including the use of the de Val-Borro et al. (2006) wave-killing prescription, but allow outflow at the outer boundary with no wave-killing.

The initial conditions of the disk are derived from the steady disk equations (Frank et al., 2002),

$$\left.\begin{aligned}
&\rho = \Sigma/H;\\
&H = c_s R^{3/2}/\left(GM\right)^{1/2};\\
&c_s^2 = P/\rho;\\
&P = \frac{\rho k_B T_c}{\mu m_p} + \frac{4\sigma}{3c}T_c^4;\\
&\frac{4\sigma T_c^4}{3\tau} = \frac{3GM\dot{M}}{8\pi R^3}\left[1-\left(\frac{2R_g}{R}\right)^{1/2}\right];\\
&\tau = \Sigma\kappa_{\rm R}\left(\rho, T_c\right) = \tau\left(\Sigma, \rho, T_c\right);\\
&\nu\Sigma = \frac{\dot{M}}{3\pi}\left[1-\left(\frac{2R_g}{R}\right)^{1/2}\right];\\
&\nu = \nu\left(\rho, T_c, \Sigma, \alpha, \ldots\right),
\end{aligned}\right\}, \tag{3.3}$$

where ρ is the gas density, Σ is the surface density, H is the scale height, c_s is the sound speed, R is the radial distance from the central object, M is the mass of the central object, $\dot{M}$ is the accretion rate through the disk, P is the total pressure, T_c is the temperature at the disk midplane, ν is the viscosity, τ is the optical depth, and $\kappa_{\rm R}$ is the Rosseland mean opacity, which throughout this work is assumed to be dominated by electron scattering, $\kappa_{\rm R} \approx \kappa_{\rm e} = 0.4\,{\rm cm}^2/{\rm g}$. We choose an α-viscosity, $\nu = \alpha c_s H$ (Shakura & Sunyaev, 1973), and introduce a prescription for the scale height in order to control where the disk transitions from radiation-dominated to gas-dominated and the proportionality of H to r in the gas-dominated region:

$$H(r) = h(r)d(r)^{1/2}; \tag{3.4}$$

$$h(r) \equiv \frac{3}{2}\frac{GM_\odot}{\eta c^2} m\dot{m}\left[1-\left(\frac{2R_g}{R}\right)^{1/2}\right], \tag{3.5}$$

$$d(r) \equiv \left[\left(\frac{r}{r_c}\right)^{2k} + \frac{1}{2}\left(1+\sqrt{1+4\left(\frac{r}{r_c}\right)^{2k}}\right)\right]. \tag{3.6}$$

Here, $m \equiv M/M_\odot$ is the mass of the central object in units of solar masses, $r \equiv R/R_g$ is the radial coordinate in units of gravitational radii ($R_g \equiv GM/c^2$), and $\dot{m} \equiv \dot{M}/\dot{M}_{\rm Edd}$ is the accretion rate in units of Eddington, where $\dot{M}_{\rm Edd} \equiv 4\pi GMm_p/(\eta\sigma_T c)$ with m_p being the mass of a proton, σ_T the Thomson cross-section, and $\eta \equiv L/(\dot{M}c^2)$ the accretion efficiency. The parameters r_c and k set, respectively, the radius in gravitational radii at which the disk pressure transitions from radiation to gas-dominated and the powerlaw slope of H in the gas-dominated region (i.e., $H \propto r^k$ far from the central object). With these prescriptions for ν and H in hand, we are able to solve the system in equation (3.3) for the surface density and sound speed distributions,

$$\Sigma(r) = \frac{16}{27}\frac{m_p}{\sigma_T}\eta\alpha^{-1}\dot{m}^{-1}r^{\frac{3}{2}}\left(1-\sqrt{\frac{2}{r}}\right)^{-1} d\,(r)^{-1}, \tag{3.7}$$

$$c_s(r) = \frac{3}{2}c\eta^{-1}\dot{m}r^{-\frac{3}{2}}\left(1-\sqrt{\frac{2}{r}}\right)^{2} d\,(r)^{\frac{1}{2}}. \tag{3.8}$$

A full derivation of these expressions (equations (3.4)–(3.8)) can be found in Appendix B.1. For this work, we use $\alpha = 10^{-2}$, $\dot{m} = 10^{-1}$, $\eta = 10^{-1}$, $r_c = 300\,\mathrm{R_g}$, and $k = 1$. Fig. 3.1 shows the surface density, temperature, and scale height distributions calculated from equations (3.7), (3.8), and (3.4) for our initial conditions. Note that throughout this derivation we consider $P = P_{\mathrm{gas}} + P_{\mathrm{rad}}$, the sum of the gas and radiation pressures. The resulting $c_s(r)$ from equation (3.8) used in our simulation is then an effective isothermal sound speed which includes the contributions from both the gas and radiation pressure.

The simulation is run on a cylindrical grid of $N_r = 2560$, $N_\theta = 3493$ cells. The radial spacing of the grid is logarithmic, with $\Delta R/R = 0.0018$. This is chosen in order to resolve the 2:1 eccentric corotation resonance (ECR), which is necessary to correctly capture the evolution of eccentricity in the disk (Teyssandier & Ogilvie, 2017).

3.3.3 Gravity

The regions of interest to this work, namely the secondary's minidisk and the gas comprising and surrounding the gap, are non-relativistic, and so we use a purely Newtonian potential for each black hole. We apply a softening length based on the local disk scale height, giving each black hole a potential of the form

$$\Phi_i = \frac{GM_i}{\sqrt{r_i^2 + \xi^2 H^2}}, \tag{3.9}$$

where M_i is the mass of black hole i, r_i is the distance between black hole i and the point of interest, $H = c_s/\Omega_K$ is the disk scale height at that point, with Ω_K the local Keplerian angular velocity, and ξ is a constant parameter controlling the magnitude of the softening. We choose $\xi = 0.6$, following from considerations made by Duffell & MacFadyen (2013). The calculations do not include the self-gravity of the disk, as the disk is much less massive than the secondary SMBH ($M_{\mathrm{disk}}/M_2 \sim 0.04$). The mass of the secondary is increased from 0 to M_2 over the first 20 orbits of the simulation in order to soften spurious waves generated by the introduction of this asymmetry to the initially symmetric system.

We set the binary on a fixed, circular orbit. The disk is less massive than the secondary SMBH and so torques from the surrounding gas are not expected to significantly alter the orbit over the duration of the simulation (verified in §3.5.3). Likewise, we do not expect significant orbital evolution due to the emission of gravitational waves. We can demonstrate this by calculating the ratio of the simulation time to the gravitational inspiral time (Peters & Mathews, 1963),

$$\frac{t_{\rm sim}}{t_{\rm GW}} = \frac{512\pi}{5} N_{\rm orb} \tilde{r}^{-5/2} q (1+q)^{1/2} (1-f_{\rm sep}^4)^{-1}, \tag{3.10}$$

where $N_{\rm orb} = 10^3$ is the number of orbits in the simulation, $\tilde{r} = 10^2$ is the initial separation in units of R_g, $q = 10^{-2}$ is the mass ratio, and $f_{\rm sep}$ is the fraction of the initial separation to which the orbit decays. For a small decay to $f_{\rm sep} = 0.99$ and our binary parameters, this ratio is below unity, indicating that the orbit will decay by $< 1\%$ of the initial separation over the course of our simulation.

3.3.4 Accretion Model

The purpose of including accretion of gas onto the secondary SMBH is twofold: first, the removal of gas from the minidisk is a natural part of the disk accretion flow, preventing spurious buildup of material at the location of the secondary; second, the mass accretion rate of an α-disk is directly linked to its radiative emission, so monitoring this property allows an estimation of the minidisk's luminosity over time. The secondary removes gas from within an accretion radius $r_{\rm accr} = 0.5 r_{\rm hill}$, where $r_{\rm hill} = a(q/3)^{1/3}$ is the Hill radius of the secondary, on an accretion timescale, $t_{\rm accr}$. $t_{\rm accr}$ varies as a function of distance r from the secondary SMBH, based on the viscous timescale for our disk model,

$$t_{\rm accr} = \frac{4}{9} \frac{G M_\odot}{c^3} \eta^2 \alpha^{-1} m \dot{m}^{-2} r^{7/2} \left(1 - \sqrt{\frac{2}{r}}\right)^2 d(r), \tag{3.11}$$

where we use the same values as in our initial conditions for all parameters except that $m = 10^6$ and r is now measured in gravitational radii of the secondary. A disk-like accretion timescale such

as this steeply increases with distance from the central body, causing accretion to be dominated by the inner parts of the minidisk and relatively insensitive to the specific value of $r_{\rm accr}$ chosen.

The fraction of mass removed from cells within $r_{\rm accr}$ is computed as

$$f_{\rm accr} = \frac{\Delta t}{t_{\rm accr}}, \tag{3.12}$$

where Δt is the simulation timestep. We monitor mass, momentum, and angular momentum accreted onto the secondary, binned over every $10^{-3}\, t_{\rm bin}$.

3.3.5 Shock Capturing

For shock capturing and characterization, we adapt FARGO3D's von Neumann-Richtmyer artificial viscosity (Von Neumann & Richtmyer, 1950), using the tensor implementation described in Appendix B of Stone & Norman (1992). This artificial viscosity has the form

$$\mathbf{Q} = \begin{cases} l^2 \Delta x^2 \Sigma \nabla \cdot \mathbf{v} \left[\nabla \mathbf{v} - \frac{\mathbf{1}}{\mathbf{3}} (\nabla \cdot \mathbf{v}) \mathbf{e} \right], & \text{if } \nabla \cdot \mathbf{v} < \mathbf{0} \\ 0, & \text{otherwise,} \end{cases} \tag{3.13}$$

where Δx is the zone size, $\nabla \mathbf{v}$ is the symmetrized velocity gradient tensor, $\mathbf{e}$ is the unit tensor, and l is a parameter controlling the number of zone widths a shock is spread over. In this work, we use $l = 5$. The key properties of the artificial viscosity are that it broadens shocks such that they are resolved on the grid, is sensitive only to compressive flows ($\nabla \cdot \mathbf{v} < \mathbf{0}$), and is large inside shocks, but small elsewhere.

In this work, we estimate the EM radiation emitted by shocks from the energy dissipated by the shock capturing scheme, $\partial e / \partial t = -\mathbf{Q} : \nabla \mathbf{v}$. This estimate assumes that shock energy is radiated efficiently, such that the thermal energy escapes the disk and does not significantly contribute to heating the gas on long enough timescales to affect the disk evolution.

For the range of typical shock Mach numbers in the simulation ($\mathscr{M} \gtrsim 10$), the thermal timescale due to radiative diffusion $t_{\rm diff} = H^2 (3 C_p / 16 \sigma)(\rho^2 \kappa_R / T^3)$ (Kippenhahn & Weigert, 1990), with C_p

the specific heat at constant pressure, is less than $t_{\rm bin}$ in the region of interest $R < 300\,R_g$, supporting this assumption.

Like the accretion monitoring, we bin the shock emission over every $10^{-3}\,t_{\rm bin}$. The Hill sphere of the secondary is excluded from the analysis of this monitoring.

3.4 Results

In this section, we present outputs from the simulation as well as our analysis of the dynamics and of the accretion rate and shock dissipation, which stand in as predictors of the electromagnetic variability of the system. When indicated, we restrict our analysis to simulation outputs after the system has reached a quasi-steady state, when $t > 700\,t_{\rm bin}$, the angular momentum deficit (AMD) has saturated, and the $r > a$ shock luminosity and average accretion rate onto the secondary have plateaued.

3.4.1 Disk Morphology and Dynamics

In contrast to previous works at this mass ratio, we find that a $q = 0.01$ binary is able to sustain a lopsided gap in the disk. In Fig. 3.2, we show snapshots of the disk surface density at various times and overplot ellipses showing the orbits taken by gas in the disk. The ellipse-fitting procedure is based on that of Teyssandier & Ogilvie (2017, see their §4). First, we calculate orbital elements for each cell in the simulation: the semi-major axis a, eccentricity e, and argument of pericenter $\overline{\omega}$. We then bin cells by semimajor axis and average the orbital properties of cells in the bin to obtain an overall fit to the orbit for a given value of a and bin width δa. Throughout this analysis, we use a bin width of $\delta a = 1.0\,R_{\rm g}$.

The eccentricity of the disk can be seen to grow over time and, as was done by Teyssandier & Ogilvie (2017), we measure this growth rate using the disk's angular momentum deficit,

$$\mathrm{AMD} = \int_{R_{\rm in}}^{R_{\rm out}} \int_{0}^{2\pi} \Sigma R^2 \Omega \left(1 - \sqrt{1-e^2}\right) R\, dR\, d\phi, \tag{3.14}$$

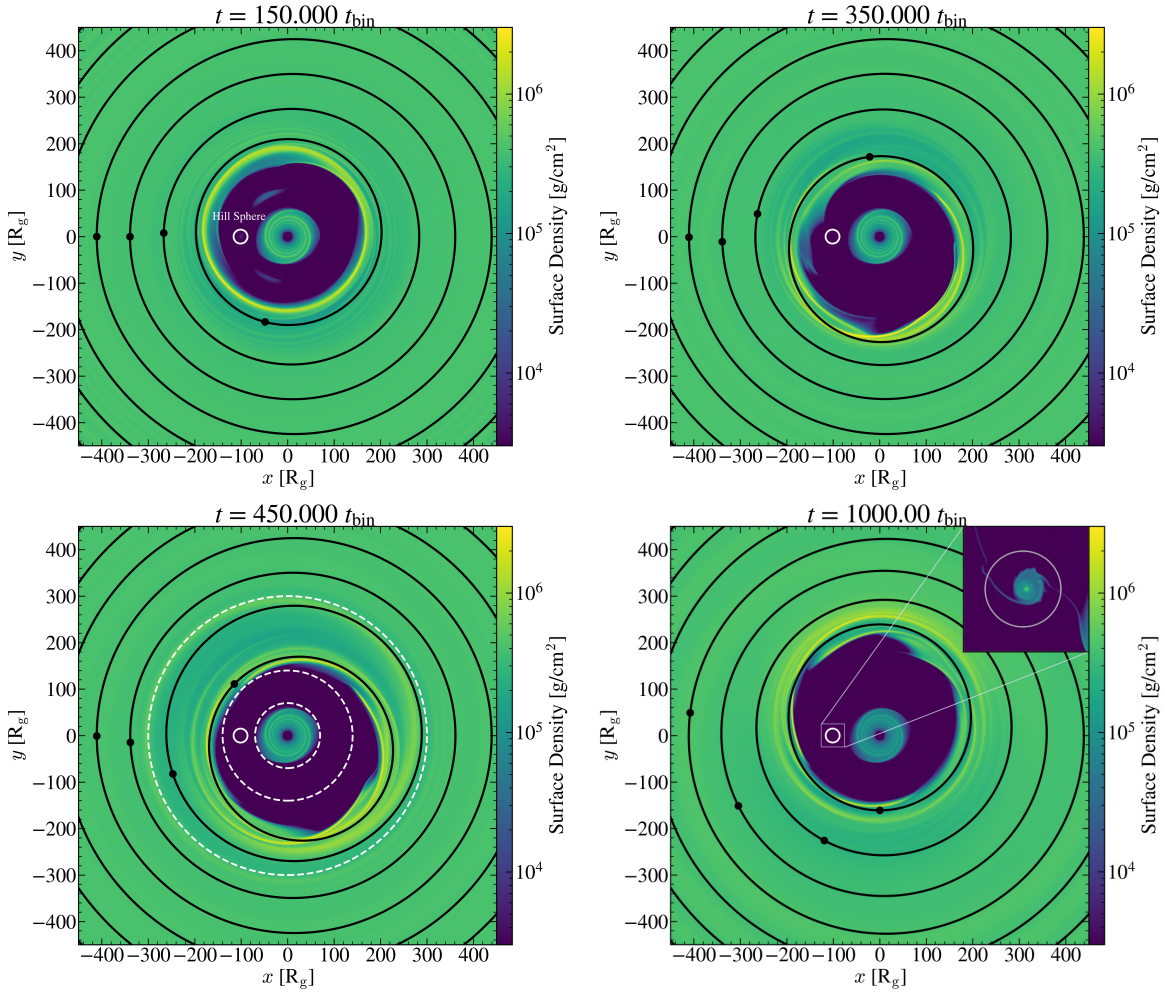


Figure 3.2: Snapshots of the gas surface density over time. The white circle indicates the extent of the secondary SMBH's Hill sphere, and the black ellipses show fits to the orbits taken by gas in the disk, with the circles on each ellipse indicating pericenter for that orbit. The snapshot at $t = 1000\,t_{\rm bin}$ includes a $50\,R_g \times 50\,R_g$ inset showing the minidisk and accretion streams, with the colorbar rescaled to span 3–3 $\times\,10^3$ g/cm^2 to better highlight the structure in this region. The snapshot at $t = 450\,t_{\rm bin}$ has dashed lines showing the boundaries used in the torque analysis in §3.4.1. Early on, the gap opened by the secondary is circular, but interactions with the binary subsequently drive rapid eccentricity growth, which saturates between 400–500 $t_{\rm bin}$. The orientation of this eccentric gap precesses relative to the binary over long timescales.

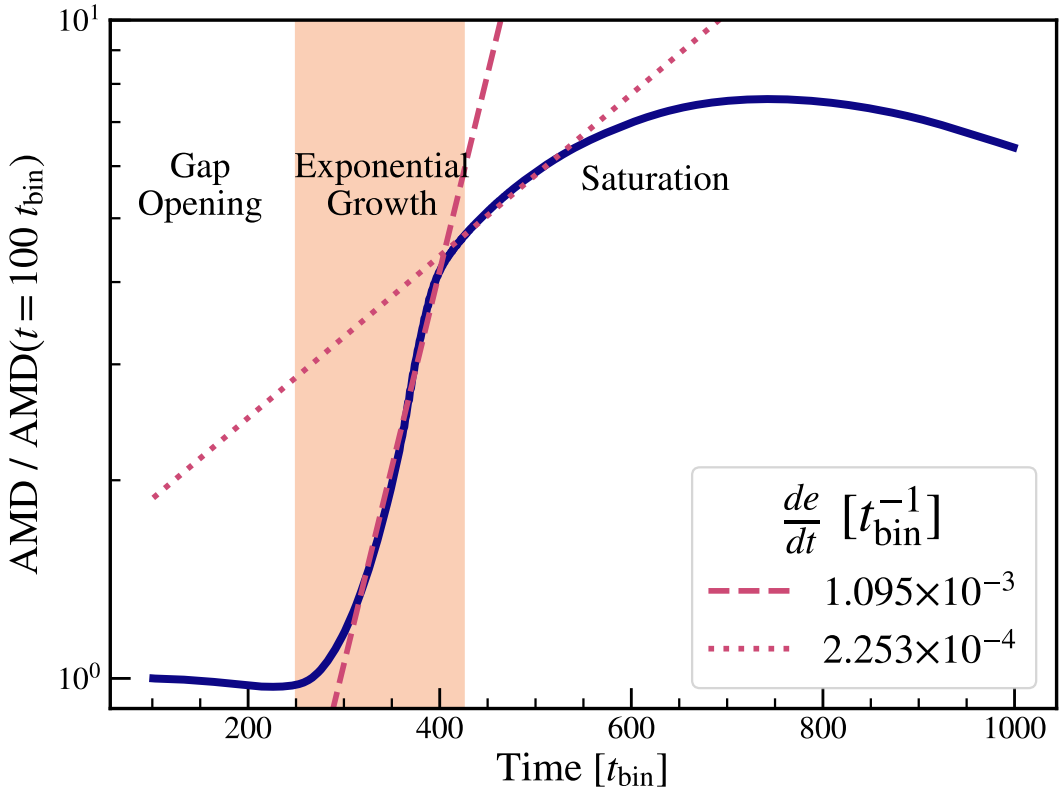


Figure 3.3: Total angular momentum deficit between $r = 200\,R_{\rm g}$ and $r = 400\,R_{\rm g}$. The orange box highlights the time during which the AMD grows exponentially. Linear fits to the growth rate are plotted for two separate times, one during the exponential phase and one immediately after as the AMD begins to saturate. These fits are labeled with the corresponding eccentricity growth rate, calculated by multiplying the slope of each fit by $\log(10)/(2\pi \times 2)$, which corrects for the log scaling, the time unit, and the proportionality AMD $\propto e^2$, as was done in Teyssandier & Ogilvie (2017).

which is shown in Fig. 3.3. Similar to Kley & Dirksen (2006) and Teyssandier & Ogilvie (2017), we observe an early relaxing phase where the gap is opened, followed by an exponential growth phase of the eccentric mode, and, finally, saturation. The saturation of the AMD indicates the settling of the large-scale dynamics of the system and coincides with the settling of behavior in other monitored quantities (see Section 3.4.2), motivating our use of it as an indicator of reaching a quasi-steady state.

Fig. 3.4 shows the time-averaged eccentricity profile of our disk at the end of the simulation, both in terms of the radial coordinate of the simulation, r, and the semi-major axes, a, of the gas orbits. The gap edge, at approximately $r, a = 200\,R_{\rm g}$, reaches an eccentricity of 0.25, larger even than the $e \approx 0.1 - 0.2$ measured for higher mass ratios in past works with hotter disks (Farris et al.,

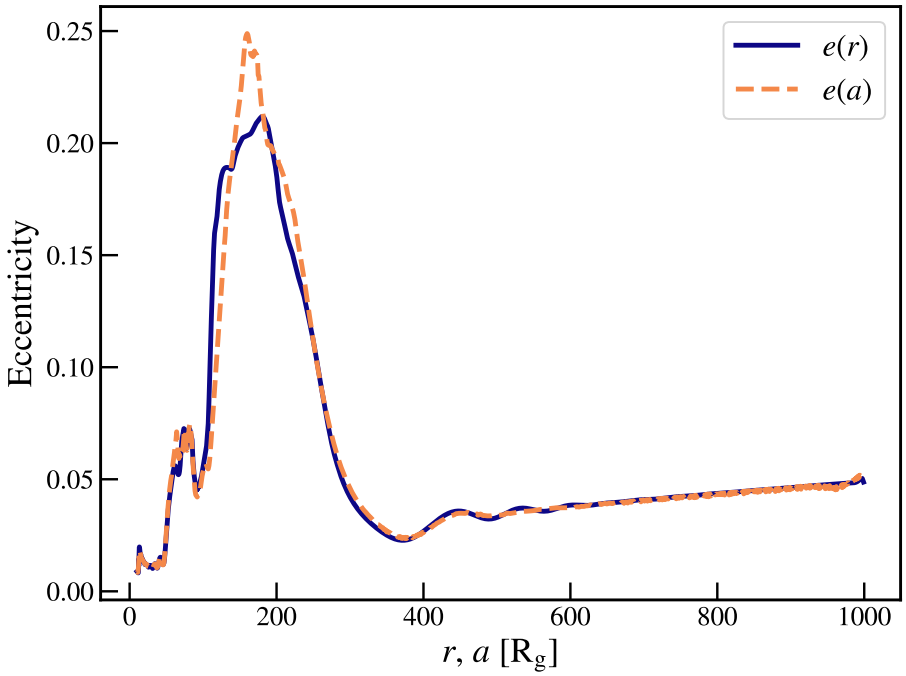


Figure 3.4: Eccentricity profile of the disk as a function of radial coordinate r (solid purple) and semimajor axis a (dashed orange). These profiles were time-averaged over 50 $t_{\rm bin}$ from $t = 950\,t_{\rm bin}$ to $t = 1000\,t_{\rm bin}$. The peak in eccentricity occurs at the approximate location of the gap edge.

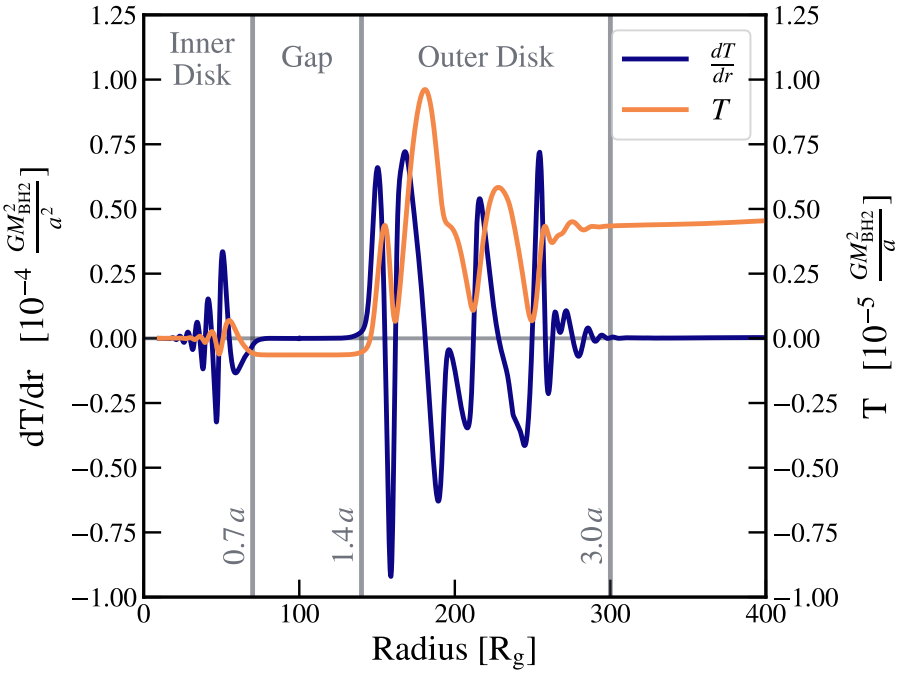


Figure 3.5: Torque density (purple) and integrated torque (orange) exerted by the binary on the disk. Quantities were time-averaged over 50 $t_{\rm bin}$ from $t = 950\,t_{\rm bin}$ to $t = 1000\,t_{\rm bin}$. The total torque on the disk is positive, and thus the reciprocal torque on the binary is negative, shrinking the binary separation over time. The disk can be separated into an inner, gap, and outer region based on the distribution of the torque density, indicated with the vertical grey lines at $0.7a$, $1.4a$, and $3a$. The total torque is plainly dominated by the contributions of the material near the outer disk edge.

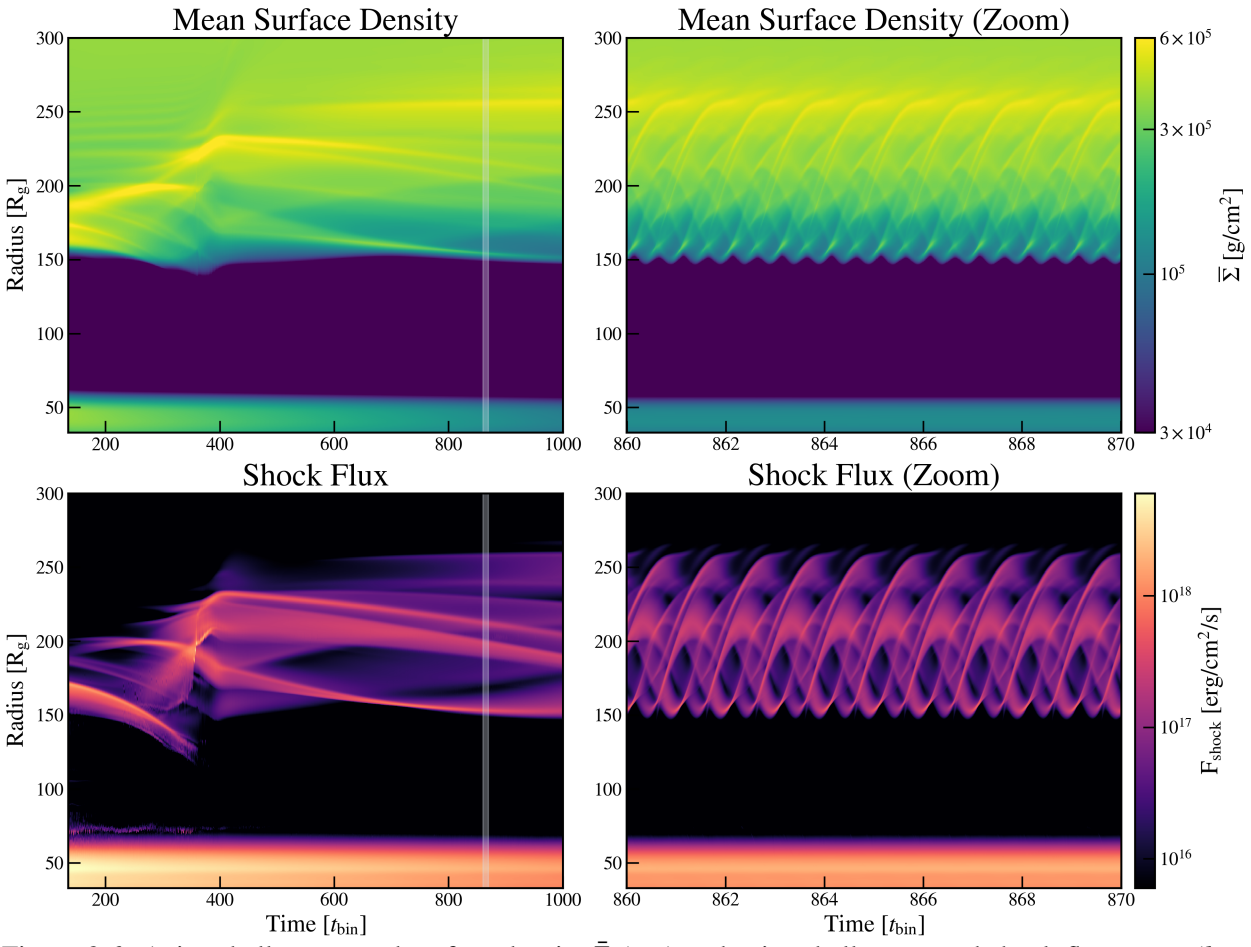


Figure 3.6: Azimuthally-averaged surface density $\bar{\Sigma}$ (*top*) and azimuthally-summed shock flux $F_{\rm shock}$ (*bottom*) as functions of time. The left column shows the quantities over the full simulation, while the right zooms in on 10 orbits during the quasi-steady state to highlight the parallel periodic structure in both quantities. The white bar on the left column plots indicates the times covered by the right column plots. The inner disk behavior is steady on short timescales, while a regular pattern is seen in both quantities at the outer edge of the gap ($\sim$ 150–250 $R_{\rm g}$), indicating periodic shock waves excited by the binary. Shock dissipation in the inner disk gradually decreases over the course of the simulation, caused by depletion of surface density in the inner disk as gas is accreted across the inner boundary of the domain.

2014; MacFadyen & Milosavljević, 2008).

It can also be seen from Fig. 3.2 that the eccentric gap is precessing. Using the same orbit-fitting as was used to produce the orbital contours shown in Fig. 3.2, we calculate the rotation angle of the $a = 200\,R_{\rm g}$ ellipse, corresponding to the gap edge, over time. From this, we obtain a precession timescale of $\sim 1.41 \times 10^3\,t_{\rm bin}$, comparable to the $\sim 3.85 \times 10^3\,t_{\rm bin}$ calculated from the linear theory developed by Teyssandier & Ogilvie (2016).

Fig. 3.5 shows the time-averaged torque density, defined in MacFadyen & Milosavljević (2008) as

$$\frac{dT}{dr} = -2\pi R \left\langle \Sigma \frac{\partial \Phi}{\partial \phi} \right\rangle, \tag{3.15}$$

and integrated torque, $T(r) = \int_0^r (dT/dr)\,dr$, of the secondary SMBH acting on the disk, averaged over 50 $t_{\rm bin}$. The strongest peak in the torque density occurs near $r = 2.5a$, coinciding with the peak in the surface density distribution of the disk. Beyond this, the torque density quickly decays to oscillations about zero. The total torque experienced by the disk is positive, with $T(\infty) \approx 7.89 \times 10^{50}$ g cm^{2}s^{-2}. The reciprocal torque of the disk on the secondary is thus negative, serving to shrink the binary separation on a timescale $t_T = M_2 a^2 \Omega_{\rm BH2}/T\,(\infty) = 3.62 \times 10^6\,t_{\rm bin}$. This is substantially longer than the runtime of the simulation, but much shorter than the timescales computed for the accretion of momentum and the emission of gravitational waves, implying that the binary's evolution is dominated by the gravitational torque of the disk at this time.

We can further explore where this negative torque comes from by following a similar procedure to Tiede et al. (2020) and Muñoz et al. (2019). We divide our domain into three regions based on the distribution of the torque density shown in Fig. 3.5: (1) an inner region $R < 0.7a$, consisting of the inner disk, (2) an outer region $R > 1.4a$, which includes the entire outer disk, and (3) a gap region $0.7a < R < 1.4a$. It can be seen from the integrated torque in Fig. 3.5 that the torque is dominated by the contributions from the outer disk, with $|T_{\rm out}| \approx 9|T_{\rm in}|$, and, further, that these contributions becomes negligible past $R \sim 3a$. We plot guides showing each of these regional boundaries in the bottom-left panel of Fig. 3.2, which reveals that the outer region $1.4a < R < 3a$ dominating the torque corresponds to the approximate extent of the overdense region near the eccentric gap

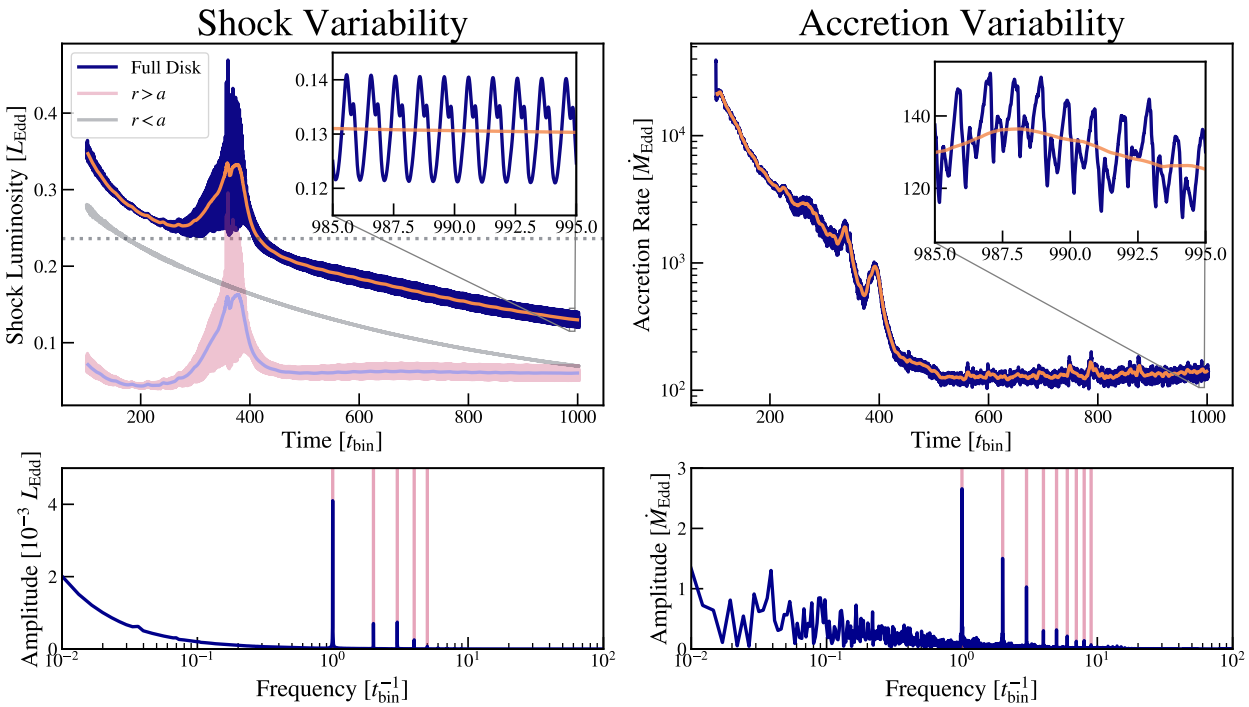


Figure 3.7: *Top*: Shock dissipation rate summed over the disk (left) and accretion rate onto the secondary SMBH (right), shown over the full runtime of the simulation. The insets zoom in on 10 orbits late in the run to highlight the periodic structure of each quantity. The orange curves are moving averages of each quantity, taken over 10 orbits. For the shock lightcurve, the horizontal dotted line shows, for comparison, the thermal luminosity of the unperturbed disk model used for our initial conditions, though we note that the shocks will primarily emit in X-rays, while the thermal luminosity will peak at optical wavelengths. The pink and grey curves are, respectively, the shock luminosity from outside and inside the secondary's orbit, revealing that the variability is dominated by regions outside the secondary's orbit (see also Fig. 3.6) and that the behavior of shocks in that region have reached a steady state. The lilac curve is a moving-average of the $r > a$ shock luminosity, taken over 10 orbits. The large, long-duration flare in the shock luminosity between 300 $t_{\rm bin}$ and 400 $t_{\rm bin}$ coincides with the exponential growth in gap eccentricity illustrated in Fig. 3.3. *Bottom*: Fourier transforms of the shock lightcurve (left) and accretion rate (right). Only data from after the system reached a quasi-steady state around ~ 700 $t_{\rm bin}$ were included in these calculations. Both quantities exhibit clear periodicity on the orbital timescale of the binary.

edge. This is in line with the results of Tiede et al. (2020), who found that the enhanced buildup of material near the gap edge in cold disks drives the total torque on the binary to be negative.

3.4.2 Electromagnetic Emission

The primary aim of this work is to investigate the time-varying electromagnetic properties of a low-mass-ratio SMBHB embedded in a realistic disk. To this end, we have employed two key proxies for variable electromagnetic emission generated from the system: shocks, tracked

via dissipation in the artificial viscosity (§3.3.5), and accretion rate onto the secondary (§3.3.4), standing in for the radiative emission of the minidisk. We find clear evidence for periodicity in both of these markers, each with a period matching the binary orbital period and a peak-to-trough ratio of ~ 1.2.

3.4.2.1 Shocks

There are two major modes in which shocks occur in our disk: spiral shocks in the inner disk and shocks at the outer edge of the eccentric gap, driven by a portion of the gas streams feeding the secondary being flung back into the gap edge. The behavior of shocks in these regions can be observed in Fig. 3.6, which shows the surface density and shock dissipation flux as a functions of time and radius through the disk. We see that, in the quasi-steady state, the shock dissipation in the inner disk is steady, while the outer gap edge displays clear repeating shock waves, which map onto similar behavior in the surface density. It is these shock waves in the outer gap edge that drive variability in the total shock emission.

We produce a shock "lightcurve" (Fig. 3.7, top left panel) by monitoring the total energy dissipated by artificial viscosity across the disk over our output timescale $\mathrm{DT} = 10^{-3}\, t_{\mathrm{bin}}$. First, we note that the shocks are bright, producing an average luminosity $L_{\mathrm{shock}} \approx 0.13\ \mathrm{L_{Edd}}$ late in the simulation, with $\mathrm{L_{Edd}}$ being the Eddington luminosity of the primary. For comparison, the unperturbed disk of our initial conditions has a luminosity $L_{\mathrm{disk}} \approx 0.25\ \mathrm{L_{Edd}}$, assuming an opacity dominated by electron scattering.

The bottom-left panel of Fig. 3.7 shows the Fourier transform of the lightcurve. There is a clear peak corresponding to the orbital frequency of the binary, with the first few harmonics of this frequency also present, but weak. This periodicity is plainly visible in the zoomed-in inset of the lightcurve itself, where we also note that the peak-to-trough ratio of the shock luminosity is only 1.17, though this rises to ~ 1.4 when considering emission from $r > a$ only, as may be relevant if the $r < a$ emission continues decaying to zero on longer timescales.

3.4.2.2 Accretion

The accretion rate onto the secondary, shown in the top-right panel of Fig. 3.7, is highly super-Eddington, hovering at around $\sim 130\,\dot{M}_{\rm Edd}$ in the steady state. Enhancement of accretion through the circumbinary disk and comparable accretion rates onto unequal-mass binary components has also been seen in preceding works such as Farris et al. (2014). Enhancement of accretion through the disk is also, in general, expected given the enhancement of Reynolds stresses due to the secondary's perturbation of the flow.

The bottom-right panel of Fig. 3.7 shows the Fourier transform of the secondary's accretion rate. Like the shock lightcurve, the accretion rate varies on the orbital frequency of the binary, with clear but weaker harmonics also apparent. The accretion rate is less steady from orbit to orbit than the shock lightcurve, but has a similar average peak-to-trough ratio of ~ 1.2. The once-per-orbit peaks in accretion rate occur when the secondary makes its closest approach to the gap edge, stripping off material, some of which is accreted onto the minidisk, and the rest of which is flung back into the gap edge. Similar behavior is discussed in, e.g., D'Orazio et al. (2013).

We also monitored the linear and angular momentum accreted by the secondary to consider the resulting evolution of the secondary's orbit and spin, respectively. In the steady state, the secondary accreted momentum at a rate $\Delta p/t_{\rm bin} = 1.01 \times 10^{-10} p_{\rm BH2}$, where $p_{\rm BH2}$ is the initial momentum of the secondary on its orbit. This net accretion torque is positive and therefore acts to increase the binary separation, but its magnitude is very low, validating our choice not to evolve the binary orbit based on the accreted momentum during the simulation. The accreted angular momentum is likewise inconsequential. Expressed as a rate of change of the dimensionless spin parameter, the secondary SMBH accretes angular momentum at a rate $\Delta a/t_{\rm bin} = 1.30 \times 10^{-10}$.

3.5 Discussion

In this section, we discuss the implications of our results in greater detail. First, we examine the disk dynamics and why the dynamics observed in this work differ from previous low-mass-

ratio SMBHB simulations. Then, we discuss our proxies for electromagnetic variability and their implications for observational identification of SMBHB candidates. Finally, we look at the various torques acting on the binary and their implications for the binary orbital evolution.

3.5.1 Disk Dynamics

Previous SMBHB works have found that eccentric cavities as drivers of accretion variability are not present at low mass ratios, $q < 0.05$ (D'Orazio et al., 2016). Conversely, in this work, with the use of a self-consistent disk model for the surface density and scale height, we show that such behavior can be present in mass ratios as low as $q \sim 0.01$.

At a similar mass-ratio regime, simulations of super-Jupiters embedded in protoplanetary disks also produce eccentric gap systems with comparable eccentricity distributions to those in Fig. 3.4 (Dempsey et al., 2021). They also find that the mass ratio for which eccentricity is excited coincides with the transition from inward to outward migration due to gravitational torques. Contrary to this, we are able to develop an eccentric gap while maintaining an inward migration of the secondary. Whether this decoupling of the two phenomena is due to our disk being much thinner than the thinnest H/R tested in Dempsey et al. (2021), our H/R being non-uniform throughout our domain, or some other difference in the two setups is an interesting question, but beyond the scope of the present investigation.

The greatest difference between the disk in this study and those of preceding works is the disk model used for our initial conditions. In particular, our disk aspect ratio H/R varies with radius and is, in general, much thinner than the constant $H/R = 0.1$ disks common in the literature, with the disk having $H/R \approx 10^{-2}$ at the location of the secondary (see Fig. 3.1). The efficiency of gap-opening depends on the relationship between opposing torques: the tidal torque, $T_{\rm tid} \propto (H/R)^{-3}$, and the viscous torque $T_{\rm visc} \propto \nu \propto (H/R)^{2}$, which work to open the gap and to fill it in, respectively. In a colder, thinner disk, the tidal torque gets stronger and the viscous torque gets weaker, leading to wider, deeper gaps and allowing gap-opening to extend to SMBHBs with lower secondary masses (Crida et al., 2006; Duffell, 2015, 2020). This phenomenon of wider gaps in colder disks has been

observed in simulations of equal-mass binaries which test different values of H/R (Ragusa et al., 2016; Tiede et al., 2020), and here we demonstrate that this behavior continues to lower mass ratios.

So a colder, thinner disk makes gap-clearing more effective. In clearing a deeper gap, the secondary removes material near its orbit, weakening the damping of eccentricity occurring at eccentric corotation resonances (ECRs), enhancing the ability for the binary to drive eccentricity growth in the disk (Teyssandier & Ogilvie, 2017). In summary, thinner disks are conducive to opening deeper gaps at lower mass ratios, which in turn drives eccentricity evolution in the outer disk and the consequent variable accretion onto the binary. Given that AGN have disks with $H/R \approx 10^{-2}$–10^{-3} (Krolik, 1999), consistent with the disk model used in this study, this suggests that the electromagnetic variability signatures seen in this and previous works may exist for lower mass ratios than previously indicated, increasing the population of SMBHB candidates identifiable in observations.

3.5.2 Variability

The underlying motivation of this work and many other simulations of SMBHBs is to better characterize the periodic electromagnetic emission which can differentiate binaries from single-SMBH AGN. Previous works generally find that high-mass-ratio binaries exhibit periodic accretion rates, but that accretion becomes steady for $q \lesssim 0.05$ (Farris et al., 2014; D'Orazio et al., 2016; Duffell et al., 2020). The timescale of accretion variability depends on the mass ratio, with lower mass ratios $0.05 \lesssim q \lesssim 0.25$ being modulated only on the binary orbital timescale, while at larger mass ratios an overdense lump forms on the gap wall, causing periodic accretion on a timescale linked to its own orbital time (Farris et al., 2014; D'Orazio et al., 2013).

In contrast, we find periodic accretion onto our secondary even with $q = 0.01$, with a timescale matching the orbital timescale of the binary. This matches the properties seen for binaries in the $0.05 \lesssim q \lesssim 0.25$ regime in these past works, and implies that this regime may simply extend to lower mass ratios given a thinner disk. We note that the exact structure of this periodicity is depen-

dent on the sink prescription used for the accretion. In the broadest sense, the accretion timescale used determines how quickly the minidisk around the secondary is drained. If this timescale is very short, the minidisk vanishes, and the amplitude of variability is magnified, being dependent only on the rate at which material enters the accretion zone. For slower sink accretion, where the minidisk persists over many orbits, the minidisk acts as a "buffer," smoothing out the "spiky" events of material being added to the minidisk (see Duffell et al. (2020) for one investigation of this relationship between accretion variability and sink accretion timescale). Here, we have chosen to model the minidisk as a steady α-disk using the same model as for our initial conditions, which resulted in a stable minidisk with moderate accretion variability. Other disk models, such as an eccentric or shock-dominated disk, may be appropriate to consider for modeling the sink accretion timescale, but will likely impact the variability seen here primarily by being either faster or slower than the timescale used in this work, resulting in variability which is more or less pronounced, respectively.

Shocks have not been used as a signifier of variable EM emission in preceding isothermal works, though they have been shown to be a source of periodic X-rays in non-isothermal simulations such as Tang et al. (2018), implying that shock capturing and characterization is necessary to understand a potentially crucial source of periodic emission driven by the binary. We find from our shock monitoring scheme that, like Tang et al. (2018), shocks occur periodically from rejected accretion streams striking the gap wall. This periodic shocking, like our variable accretion, occurs on a timescale equal to the orbital timescale of the binary.

One important caveat to the variability seen in our accretion and shocks is that the amplitude is modest, with both proxies peaking $\lesssim 10\%$ above their mean. However, the timescale is well-constrained and short ($t_{\rm bin} \approx 0.1$ yr), allowing many cycles of such a system to be obtained from continued monitoring with UV or X-ray instruments, alleviating the difficulties discussed by Vaughan et al. (2016) in distinguishing genuine periodicity from insufficiently-sampled red noise.

Further still, in Fig. 3.8 we examine the timing relationship between the shock lightcurve and the secondary's accretion rate via cross-correlation and find that they are nearly fully out-

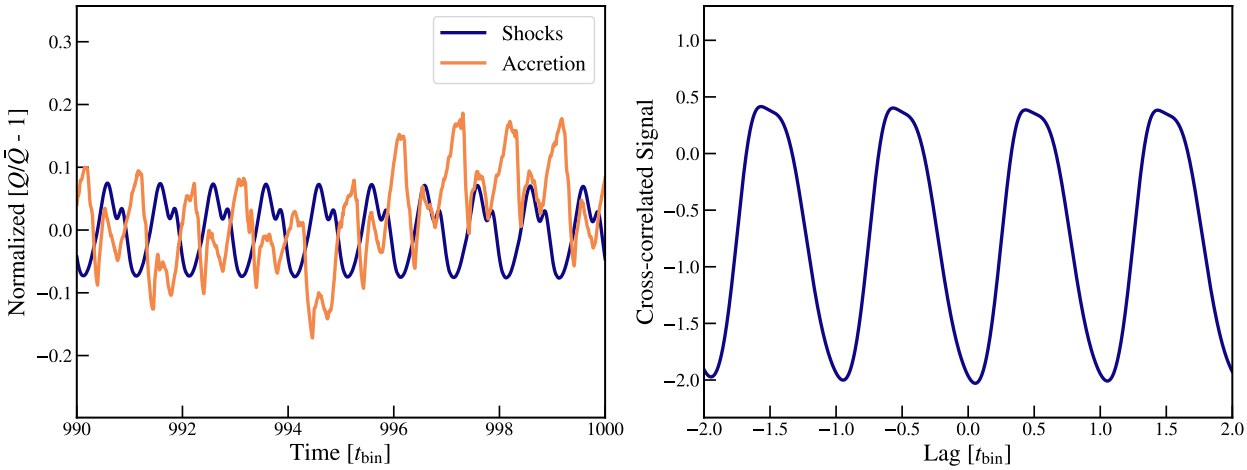


Figure 3.8: Examination of the timing relationship between shocks and accretion. *Left:* Shock lightcurve (*purple*) and accretion rate (*orange*), each normalized by their mean value. *Right:* Cross-correlation of the shock and accretion "lightcurves." The cross-correlation is itself periodic due to both signals being periodic, and peaks at a lag of 0.43 $t_{\rm bin}$. Since the two signals have a period of $t_{\rm bin}$, this affirms that they are almost fully out of phase with one another, as is apparent by eye in the left panel.

of-phase with one another, with a timing offset of $\Delta t_{\rm lag} \approx 0.43\ t_{\rm bin}$ between peaks in the accretion rate and peaks in the shock luminosity. This parallels the relationship found between the optical lightcurve and accretion rate for a circular binary in the fully adiabatic simulations performed by Westernacher-Schneider et al. (2022). This timing offset is potentially valuable as an identifier of SMBHB candidates, as the shocks can produce X-ray variability (Tang et al., 2018), while the minidisk emission will typically peak at UV or longer wavelengths, depending on the mass of the secondary (Shakura & Sunyaev, 1973). This type of correlated variability across wavebands is not expected for red noise, and thus cross-correlation analysis between UV and X-ray monitoring of AGN could be a valuable observational pursuit for identifying candidate SMBHBs.

3.5.3 Binary Orbital Evolution

A recurring point of discussion around SMBHBs is the sign of the gravitational torque acting on the binary, as this tends to dominate the evolution of the separation prior to the gravitational wave-dominated phase. We find that our disk exerts a negative torque on the binary, reducing the binary separation over time, which matches Duffell et al. (2020), which finds that the torque is negative for mass ratios below $q \sim 0.05$, albeit for a much warmer disk with constant $H/R = 0.1$.

The majority of the negative torque can be attributed to the build up of material at the outer edge of an eccentric gap – as seen in the case of equal-mass binaries in Tiede et al. (2020) in which this effect is greater in magnitude for colder disks that accumulate more material at the gap edge. Conversely, Derdzinski et al. (2021) find, for lower mass ratios than ours, that the torque on the binary flips from negative to positive as the disk becomes thinner, though they note that the density asymmetry key to determining the gravitational torque is unresolved, falling within the smoothing length of the secondary in some of their simulations. In general, these works and ours suggest that the magnitude of this effect is dependent on the specific disk model as well as the mass ratio of the embedded binary, likely due to whether the system leads to the opening of an eccentric gap. A systematic study of the gravitational torque over a wide range of gap opening scenarios is an interesting avenue for future investigation.

While not explored in this work, it is expected that, just as the binary excites eccentricity in the disk, the disk should excite eccentricity in the binary orbit. There are several works which have explored the case of eccentric binaries (D'Orazio & Duffell, 2021; Miranda et al., 2017) finding that the eccentricity of the binary affects the variability of accretion, the morphology and dynamics of the disk gap, and the evolution of the binary orbit. Franchini et al. (2023) have also found that fixing the binary orbit leads to overestimation of the gravitational torque and underestimation of accretion torques for equal-mass binaries. Exploring the effects of eccentric and live binaries in our cold disk model and how these compare to the existing warmer disk works is an interesting path for future investigation.

3.6 Summary

We performed a 2D, locally isothermal hydrodynamic simulation of a low-mass-ratio ($q = 10^{-2}$) SMBHB embedded in a disk with initial surface density and sound speed profiles derived from a physically self-consistent disk model. We monitored the dynamical evolution of the system as well as two proxies for electromagnetic variability, the accretion rate onto the secondary SMBH, and the energy dissipated by shocks.

Our main findings can be summarized as follows.

1. The binary opens a wide, eccentric gap which precesses on long timescales. This behavior is seen throughout the literature at larger mass ratios, but has not generally been observed for $q \lesssim 0.05$. We attribute this change to our disk model, which is much thinner than the $H/R = 0.1$ disks common in the existing literature, and in line with the $H/R \sim 0.01$–0.001 expected for real AGN disks. A thinner disk is both more susceptible to gravitational torques from the binary, which open the gap, and experiences weaker viscous torques, which serve to close it. Wider cavities in thinner disks have been seen in a few works which explored changing H/R with $q = 1$ binaries, and here we have shown that this behavior extends to $q = 0.01$ binaries.

2. We find that accretion onto the secondary SMBH is clearly variable, with a period matching the orbital period of the binary and a peak-to-trough ratio of ~ 1.2. As with the eccentric gap, this behavior was previously not seen for $q \lesssim 0.05$ in works using thicker disks. We find, as has been the case in previous works, that the peaks in the accretion rate occur due to the passage of the secondary near the overdensity at the edge of the gap, stripping off material to feed the minidisk. This process is necessarily linked to the gap becoming eccentric. Since we find that a thinner disk leads to eccentricity at smaller mass ratios than previously seen, it is unsurprising that accretion variability follows. Importantly, since real AGN disks are expected to be thin ($H/R \sim 0.01$–0.001), we expect that the parameter space for which real binaries are variable is wider than has been previously established by works with thicker disks.

3. We find that shocks excited by the binary are also periodic, with a period matching the orbital period of the binary and a peak-to-trough ratio of 1.17. Shocks have been found to be an important source of periodic X-ray emission in non-isothermal works, but have not previously been monitored in isothermal simulations.

4. We find that there is a correlated lag between the accretion and shock lightcurves. The two

quantities are nearly fully out of phase, with the shocks lagging behind accretion by $0.43\,t_{\rm bin}$. This presents a potential smoking gun for binary candidacy in observations. Since accretion tracks the minidisk luminosity, which will typically be brightest at ultraviolet wavelengths, and shocks are seen to be bright in X-rays, the timing correlation between shock dissipation and accretion rate implies correlated variability in separate wavebands. Observations can then be made to search for such correlated variability as a sign of a possible SMBHB rather than more ambiguous single-waveband variability.

3.7 Acknowledgements

This research was supported in part through computational resources and services provided by Advanced Research Computing at the University of Michigan, Ann Arbor. This work was funded in part by Michigan Space Grant Consortium, NASA grant #NNX15AJ20H.

A.K. would like to acknowledge support provided by NASA through the NASA Hubble Fellowship grant #HST-HF2-51463.001-A awarded by the Space Telescope Science Institute, which is operated by the Association of Universities for Research in Astronomy, Incorporated, under NASA contract NAS5-26555.

M.R. acknowledges support from NASA grants 80NSSC20K1541 and 80NSSC20K1583 and NSF grants AST-1715140 and AST-2009227.

CHAPTER 4

Prospects for Gravitational Wave Detection of Gas-Dominated Supermassive Black Hole Binary Interactions

This chapter has been submitted for publication in the Astrophysical Journal. This work was co-authored with Aleksandra Kuznetsova. The paper is reproduced here with minor stylistic revisions.

4.1 Abstract

Numerical simulations predict that disk-secondary interaction in supermassive black hole binaries (SMBHBs) should produce variable and periodic electromagnetic emission. We apply a range of relevant observational and modeling constraints to the SMBHB parameter space, comparing the subset of SMBHB parameters that are detectable with current and future gravitational wave facilities to the model space from analytic and numerical models expected to produce observable periodic electromagnetic signatures driven by disk-secondary interaction. Our analysis aims to produce self-consistent predictions of gravitational-wave detectable SMBHB disk populations, investigating both a full three zone Shakura-Sunayev α-disk, as well as the commonly employed constant aspect ratio disk. We find that, for a fiducial $\dot{M} = 0.1\dot{M}_{\rm Edd}$ disk, gas-dominated binaries like those in simulations are only GW-detectable out to redshifts $z = 0.3$ and only then in a narrow range of masses $\sim 10^8$ M$_\odot$ with orbital periods ~ 10 yr. In the context of a full three zone

SS73 AGN disk model, our results predict that the bulk of detectable GW emission from SMBHBs will arise from close-in secondaries embedded in the inner radiation-dominated zone of the disk – outside of the physical regimes currently probed by the bulk of numerical simulations.

4.2 Introduction

Supermassive black hole binaries (SMBHBs) are expected to form during the hierarchical growth of galaxies via mergers (Begelman et al., 1980), with other, more niche channels being possible for low-mass-ratio SMBHBs (e.g., in-situ formation of intermediate mass black holes in AGN disks (McKernan et al., 2012) or disruption of IMBH-hosting globular clusters (Fragione & Capuzzo-Dolcetta, 2016; Fragione et al., 2018a; Arca-Sedda & Gualandris, 2018; Fragione et al., 2018b; Rasskazov et al., 2019)). SMBHBs are thus a valuable probe into the evolution and co-evolution of host galaxies and their supermassive black holes. They serve as a source of continuous gravitational waves (GWs), which may be detected by pulsar timing array (PTA) collaborations, and their mergers may in turn be detected by the future Laser Interferometer Space Antenna (LISA) mission Amaro-Seoane et al. (2017). Several PTA collaborations have reported detection of a nanohertz gravitational wave background (GWB) (Agazie et al., 2023c,d; EPTA Collaboration et al., 2023; Antoniadis et al., 2023b; Reardon et al., 2023a,b; Xu et al., 2023), possibly originating from a population of SMBHBs, though alternative explanations exist (Afzal et al., 2023) and there remain no individually-resolved binaries at this time.

While there is no definite confirmation of a SMBHB, several candidate binaries have been identified via their electromagnetic (EM) emission. The most promising, and only imaged, candidate is in the radio galaxy 0402+379, where radio interferometry detected two distinct flat-spectrum radio cores at a projected separation of ~ 7 pc (Rodriguez et al., 2006) and later VLBI measurements confirmed proper motions consistent with the SMBHB interpretation (Rodriguez et al., 2009). At smaller separations, spectroscopic observations can identify candidates via shifts between broad and narrow emission lines (Eracleous et al., 2012; Runnoe et al., 2017) or broad emission lines whose central frequency changes over time (Ju et al., 2013; Shen et al., 2013; Wang et al., 2017),

both of which can arise as a consequence of orbital motion in a binary. Finally, for separations $\ll 1$ pc, there are various variability signatures which can be caused by the presence of a SMBHB, including relativistic Doppler boosting throughout the binary's orbit (D'Orazio et al., 2016; Duffell et al., 2020; D'Orazio et al., 2015), flares from a secondary SMBH passing through the primary's accretion disk (Valtonen et al., 2008), and modulated accretion onto each of the binary components due to the time-dependent, non-axisymmetric binary potential as is commonly seen in hydrodynamics simulations of these systems (MacFadyen & Milosavljević, 2008; D'Orazio et al., 2013; Farris et al., 2014, 2015; D'Orazio et al., 2016; Tang et al., 2017, 2018; Moody et al., 2019; Tiede et al., 2020; Duffell et al., 2020; Westernacher-Schneider et al., 2022; D'Orazio & Duffell, 2021; Derdzinski et al., 2021; Whitley et al., 2024).

Periodic modulation of EM emission is of particular interest as it remains a viable test of binary candidacy at the extremely close separations most relevant to gravitational wave detection. Many numerical works have been performed to better characterize the expected EM signatures of embedded SMBHBs approaching and during the merger stage for different binary and disk properties (Farris et al., 2015; D'Orazio et al., 2016; Tang et al., 2018; Duffell et al., 2020; Whitley et al., 2024). With decreasing mass ratio, simulations find that variable accretion vanishes (D'Orazio et al., 2016), though the exact mass ratio for this threshold depends on the properties of the circumbinary disk; with colder, thinner disks producing variable accretion rates down to lower mass ratios than is possible in the relatively thick $H/R = 0.1$ model common in the literature (Whitley et al., 2024). The exact timescale of variability varies with mass ratio (D'Orazio et al., 2013, 2016), but is of order the orbital period of the binary. It has also been found that SMBHBs produce substantial shock-heating at the edge of the gap due to gas flung outward by the secondary SMBH (Farris et al., 2015) and, further, that the shocks are themselves periodic and correlated with the accretion variability, implying a possible multiwavelength signature that further distinguishes binary-induced periodicity from single-AGN variability (Tang et al., 2018; Whitley et al., 2024).

To date, simulations exploring the accretion and shock-driven EM variability of SMBHBs have been focused implicitly or explicitly on systems in the thermally stable gas-dominated regime.

However, we can expect that the GW-loudest binaries will be at close separations in the radiation-dominated innermost part of the accretion disk. Conditions in the radiation-dominated zone are favorable for the development of thermal instabilities, which both provides a mechanism for variable behavior distinct from that driven by disk-secondary interaction in the gas-dominated zone (Ross et al., 2017; Habibi & Abbassi, 2019; Jiang & Blaes, 2020) and presents a numerical hurdle for 2D simulations wishing to self-consistently evolve the disk temperature for higher-fidelity understanding of the EM properties of the system. Capturing the physics of the radiation dominated zone is possible with the use of 3D radiation hydrodynamics simulations, but running simulations for the number of orbits required to achieve steady-state behavior is computationally expensive, making coverage of the entire relevant SMBHB parameter space with these methods currently intractable. Thus, it is of interest to know which binaries are simultaneously observable by existing or upcoming GW detectors, have expected light-curve periods on human-observable timescales, and also have a separation which places the secondary SMBH outside of the thermally-unstable radiation-dominated zone, as this is where current simulation predictions are directly applicable to multimessenger detections.

The purpose of this work is to examine several constraints on the SMBHB population in the context of both a conventional three-zone Shakura-Sunyaev α-disk model (Shakura & Sunyaev, 1973) as well as the popular constant aspect-ratio disk model (e.g., MacFadyen & Milosavljević, 2008; D'Orazio et al., 2016; Derdzinski et al., 2021) for a comprehensive range of disk and binary parameters. We consider the sensitivity of GW detectors, the orbital period of the binary, the residence time of the binary as it migrates inward, and the complications presented by relevant physics in different disk regions, including the thermal instability in the radiation-dominated zone. Based on these constraints, we identify the subset of the SMBHB and disk parameter spaces which satisfy all these constraints and how this compares to the model space explored in the existing literature, with the aim of informing future studies as to the most relevant systems for future GW observations that can be investigated with the most sophisticated physics possible.

This paper is organized as follows. In Section 4.3, we describe the disk models considered and

the criterion used to identify "maximally interesting" SMBHB parameter combinations. Section 4.4 presents visualizations of these criteria for the tested models and our discussion of the implications, particularly regarding which sorts of binaries are most desirable to simulate in order to best support multimessenger searches for SMBHBs. We summarize our findings in Section 4.5.

4.3 Methods

We consider two distinct disk models in this work — a conventional, steady, thin α-disk as described in Shakura & Sunyaev (1973) (hereafter SS73), and a constant aspect-ratio disk model as is commonly used in 2D simulations of SMBHBs. The conventional α-disk is described by the equations

$$\left.\begin{aligned}
&\text{a. } \rho = \Sigma/H; \\
&\text{b. } H = c_s/\Omega_K; \\
&\text{c. } c_s^2 = P/\rho; \\
&\text{d. } P = \frac{\rho k_B T_c}{\mu_0 m_H} + \frac{4\sigma}{3c} T_c^4 = P_g + P_r; \\
&\text{e. } \frac{4\sigma T_c^4}{3\tau} = \frac{3GM_p\dot{M}}{8\pi R^3}\left[1 - \left(\frac{2R_g}{R}\right)^{1/2}\right]; \\
&\text{f. } \tau = \Sigma\kappa_{\mathrm{R}}(\rho, T_c) = \tau(\Sigma, \rho, T_c); \\
&\text{g. } \nu\Sigma = \frac{\dot{M}}{3\pi}\left[1 - \left(\frac{2R_g}{R}\right)^{1/2}\right]; \\
&\text{h. } \nu = \alpha c_s H,
\end{aligned}\right\}, \tag{4.1}$$

where ρ is the gas density, Σ is the surface density, H is the scale height, c_s is the sound speed, R is the radial distance from the central object, M_p is the mass of the central object, $\Omega_K = \sqrt{GM_p/R^3}$ is the Keplerian orbital frequency, $R_g = GM_p/c^2$ is the gravitational radius of the central object, $\dot{M}$ is the accretion rate through the disk, P is the total pressure, with gas pressure $P_g = \rho k_B T_c/\mu_0 m_H$ and radiation pressure $P_r = 4\sigma T_c^4/3c$, T_c is the temperature at the disk midplane, ν is the kinematic viscosity, α is a constant, τ is the optical depth, and κ_{R} is the Rosseland mean opacity, which

we take to be dominated by electron scattering, $\kappa_{\rm R} \approx \kappa_{\rm es} = \mu_e \sigma_T / m_H$, or free-free absorption $\kappa_{\rm R} \approx \kappa_{\rm ff} = (8 \times 10^{22}\ {\rm cm^2\ g^{-1}}) \mu_{\rm e} \left[\rho / \left({\rm g\ cm^{-3}}\right)\right] ({\rm T/K})^{-7/2}$, depending on which region of the disk we are considering. μ_0 is the mean molecular mass and μ_e is the mean mass per electron, both in units of hydrogen atomic mass, m_H. Following Haiman et al. (2009b), we adopt the fiducial values $\mu_0 = 0.615$ and $\mu_e = 0.875$, corresponding to a fully ionized gas consisting of 75% hydrogen and 25% helium. Correspondingly, for brevity, later expressions will not include scalings with gas composition (see Haiman et al. (2009b) for the full expressions).

The properties of the typical SS73 model disk are divided into three zones, depending on the dominant form of opacity and the whether gas or radiation dominates the total pressure. We consider three zones: an innermost radiation pressure-dominated zone where electron scattering is the dominant opacity, a middle gas-dominated zone where electron scattering remains the dominant opacity, and an outer zone which is still gas-dominated but where free-free absorption processes dominate over electron scattering. A general expression for the surface density in terms of the scale height can be obtained by combining equations (4.1g), (4.1h), and (4.1b), yielding

$$\Sigma = \frac{1}{3\pi G^{1/2}} \alpha^{-1} M_p^{-1/2} \dot{M} H^{-2} R^{3/2} \left[1 - \left(\frac{2R_g}{R}\right)^{1/2}\right], \tag{4.2}$$

and combining equations (4.1a–c) with (4.1e–f) gives the scale height in terms of the pressure and opacity,

$$H = \frac{3}{8\pi c} \frac{P}{P_r} \kappa_{\rm R} \dot{M} \left[1 - \left(\frac{2R_g}{R}\right)^{1/2}\right]. \tag{4.3}$$

The surface density in each of the three zones can then be obtained by combining equations (4.2–4.3) and requiring a) $\kappa_{\rm R} = \kappa_{\rm es}$ and $P = P_r$, b) $\kappa_{\rm R} = \kappa_{\rm es}$ and $P = P_g$, and c) $\kappa_{\rm R} = \kappa_{\rm ff}$ and $P = P_g$, resulting in

$$\left.\begin{aligned}
\Sigma_a &= 7.5 \times 10^5\ {\rm g\,cm^{-2}}\ \ \alpha_{0.01}^{-1} \left(\frac{\dot{m}_{0.1}}{\varepsilon_{0.1}}\right)^{-1} r_3^{3/2} f^{-1} \\
\Sigma_b &= 2.48 \times 10^6\ {\rm g\,cm^{-2}}\ \ \alpha_{0.01}^{-4/5} \left(\frac{\dot{m}_{0.1}}{\varepsilon_{0.1}}\right)^{3/5} M_{p,7}^{1/5} r_3^{-3/5} f^{3/5} \\
\Sigma_c &= 3.97 \times 10^6\ {\rm g\,cm^{-2}}\ \ \alpha_{0.01}^{-4/5} \left(\frac{\dot{m}_{0.1}}{\varepsilon_{0.1}}\right)^{7/10} M_{p,7}^{1/5} r_3^{-3/4} f^{7/10}
\end{aligned}\right\}, \tag{4.4}$$

where Σ_a is the surface density in the radiation-dominated inner zone, Σ_b is the surface density in the middle zone, Σ_c is the surface density in the outer zone, and we have defined $f \equiv 1-(2/r)^{1/2}$ for brevity. Here and elsewhere we use dimensionless quantities representing our fiducial choices for certain parameters, defined as $r = R/R_g$, $r_3 = r/10^3$, $\alpha_{0.01} = \alpha/0.01$, $\dot{m}_{0.1} = \dot{M}/\dot{M}_{\rm Edd}/0.1$, $\varepsilon_{0.1} = \varepsilon/0.1$, and $M_7 = M/10^7\ \mathrm{M}_\odot$. These and other such fiducial parameter choices are summarized in Table 4.1 below.

In numerical studies, it is typical to restrict the simulation to a local domain, adopting a constant aspect ratio h to define the scale height,

$$H = hR. \tag{4.5}$$

Such models typically use a power-law surface density profile:

$$\Sigma = \Sigma_0 \left(\frac{r}{r_0}\right)^{-\delta}, \tag{4.6}$$

with $\delta = 0$ being most common, but other values (e.g., $\delta = 3$ in Farris et al. 2014 and $\delta = 1/2$ in Derdzinski et al. 2021 and Tang et al. 2018) also seeing use. While the magnitude of Σ_0 is arbitrary for non-migrating black holes in many scale-free simulations, our analysis uses the surface density to estimate migration rates dR/dt for disk-mediated migration needed to calculate the secondary's residence time $t_{\rm res} \equiv -R(dR/dt)^{-1}$, which describes how long the secondary spends at a given R as it migrates inward. We obtain a value for Σ_0 by combining equations (4.1g) and (4.1h), yielding

$$\Sigma_0 = 3.84\times10^4\ \mathrm{g\,cm^{-2}}\ \ \alpha_{0.01}^{-1}\frac{\dot{m}_{0.1}}{\varepsilon_{0.1}} h_{0.1}^{-2} r_0^{-1/2}\left(1-\left(\frac{2}{r_0}\right)^{1/2}\right), \tag{4.7}$$

with $\varepsilon = L_{\rm acc}/\dot{M}c^2$ being the accretion efficiency.

We consider a binary parameter space spanning total binary masses $10^5\ \mathrm{M}_\odot < M < 10^{10}\ \mathrm{M}_\odot$, separations $10\ \mathrm{R_g} < a < 10^5\ \mathrm{R_g}$, and mass ratios $10^{-3} < q < 1$. These ranges cover the masses and separations to which low-frequency GW detectors are sensitive and the mass ratios at which gap-opening is likely for an embedded secondary in an AGN disk.

Parameter	Definition	Fiducial Value	Disk Model/Zone
α	viscosity parameter	0.01	All
$\dot{m}$	$\dot{m} = \dot{M}/\dot{M}_{\rm Edd}$	0.1	All
ε	$\varepsilon = L/\dot{M}c^2$	0.1	All
M	Total binary mass	10^7 $M_\odot$	All
M_p	Primary BH mass	10^7 $M_\odot$	All
r	$r = R/R_g$=$R/(GM/c^2)$	10^3	All
h	$h = H/R$	0.1	H/R=const
δ	$\Sigma \propto r^\delta$	0; 3/2, -3/5, -3/4	H/R=const; SS73 (Inner, Middle, Outer)

Table 4.1: Parameters and their fiducial values for the disk models considered. In addition to the power-law index δ used for the constant aspect ratio disk, for comparison, we include the corresponding δ calculated for the three zones of the SS73 model.

4.3.1 Observational constraints

The key observational signatures we are interested in to identify SMBHBs are: periodicity in EM radiation and direct detection of continuous gravitational waves. Previous simulations of SMBHBs (D'Orazio et al., 2013, 2016; Duffell et al., 2020) find that the period of EM modulation is expected to be of order the orbital period of the binary,

$$t_{\rm bin} = 2\pi\sqrt{\frac{a^3}{GM}}, \tag{4.8}$$

where a is the binary separation and M is the total mass of the binary. Identifying periodicity in AGN requires monitoring the target system for several cycles (Vaughan et al., 2016), with multiple samples per cycle. Thus, we constrain our domain of interest to binaries with a period longer than 1 hour, below which it is challenging to achieve sufficient sampling, and shorter than 10 years, above which it is challenging to observe for a sufficient number of cycles to distinguish periodicity from stochastic variability.

Gravitational wave observations are limited by both the frequencies and strains which upcoming detectors are sensitive to. The continuous-wave frequency for a circular binary is twice the orbital frequency of the binary. For a binary at redshift z, the observed frequency is

$$f_{\rm gw} = \frac{2}{t_{\rm bin}}(1+z)^{-1} = \frac{1}{\pi}\sqrt{\frac{GM}{a^3}}(1+z)^{-1}, \tag{4.9}$$

and the strain amplitude is given by

$$h_{\rm gw} = \frac{8}{\sqrt{5}} \frac{c}{D_L} (\pi f_{\rm gw})^{2/3} (\frac{G M_{\rm ch}}{c^3} (1+z))^{5/3}, \tag{4.10}$$

where D_L is the luminosity distance to the source and $M_{\rm ch} = (q/(1+q)^2)^{3/5} M$ is the chirp mass of the binary. To determine what sources are GW-observable, we compare the frequencies and strains for our SMBHB parameter space to the sensitivity curves for the NANOGrav 15-year dataset (Agazie et al., 2023a), the *LISA* ESA L3 proposal (Amaro-Seoane et al., 2017), and a projection of PTA sensitivity in the 2030s when the Square Kilometer Array is online, based on the estimates of Sesana et al. (2008). We calculate these instrument sensitivities and source strains using tools from the gwent python package (Kaiser & McWilliams, 2021).

We calculate the combinations of SMBHB parameters which produce detectable strains for sources at three illustrative redshifts: $z = 2$, corresponding to the approximate peak of AGN activity (Wolf et al., 2003), $z = 0.3$, corresponding to the approximate median redshift of the SMBHB population inferred to have been detected in the NANOGrav 15-year dataset (Agazie et al., 2023b), and $z = 0.01$, which we present as an upper limit for what is technically detectable.

4.3.2 Model constraints

In addition to the above observational considerations, we investigate the effect of the local disk environment of the embedded secondary on the expected electromagnetic signatures and their observability. In order to determine the regions of parameter space for which there are applicable model predictions in addition to which regions would require follow-up with radiation hydrodynamics simulations, we consider three primary criteria: gap-opening, radiation pressure, and secondary migration rate.

All simulations that have found evidence for EM-variability in SMBHB systems – either through the proxy of variable accretion rates onto the binary components (e.g., MacFadyen & Milosavljević, 2008; D'Orazio et al., 2016) or through shock variability at the edges of asymmet-

ric gaps (e.g., Tang et al., 2018; Whitley et al., 2024) – require that the secondary is able to open a gap within its disk. While gap width is controlled by SMBHB and disk model parameters and correlated with variability properties – wider gaps being formed by higher mass ratio secondaries or within colder disks associated with higher-amplitude variability (D'Orazio et al., 2016; Tiede et al., 2020) – we require only that gap-opening is possible, through the gap-opening criteria on the mass ratio described in Kocsis et al. (2012b). The constraints on the mass-ratio are two-fold, arising from the balance of tidal and viscous torques near the secondary (Lin & Papaloizou, 1986; Crida et al., 2006). The first constraint requires that $q > q_{s0}$ to ensure that the gap is not closed by viscous torques:

$$q_{s0} = \sqrt{\frac{3k_\nu}{f}\frac{\nu}{r_s^2\Omega_s}}\left(\frac{H}{r_s}\right)^{3/2}. \tag{4.11}$$

The second constraint, $q > q_{u0}$ ensures that the gap edge is outside the Hill radius of the secondary so that the gap is not closed by the near-field gravitational forces of the secondary:

$$q_{u0} = \frac{k_\nu}{f}\frac{\nu}{r_s^2\Omega}, \tag{4.12}$$

where $k_\nu = 1/2$ is the radial exponent of the unperturbed viscous torque near the secondary, $f \approx 0.01$ is a constant determined from numerical simulations, ν is the viscosity near the secondary, r_s is the radial position of the secondary in the disk, Ω_s is the Keplerian orbital velocity at r_s, and H is the scale height of the disk near the secondary. Throughout this work, we will consider $\nu = \alpha c_s H$, where c_s is the sound speed and α is the conventional viscosity parameter for a thin disk. This, along with the scale height $H = c_s/\Omega$, reduce the above expressions to

$$q_{s0} = \sqrt{\frac{3k_\nu\alpha}{f}}\left(\frac{H}{r_s}\right)^{5/2}, \quad \text{and} \tag{4.13}$$

$$q_{u0} = \frac{k_\nu}{f}\alpha\left(\frac{H}{r_s}\right)^2. \tag{4.14}$$

For observable EM variability signatures, we require that the mass ratio satisfies both $q > q_{s0}$ and

$q > q_{u0}$.

Our second criterion imposes a constraint on the black hole separation, limiting the parameter space for predicted electromagnetic signatures to those from the gas-pressure dominated zone, as this is the region where the predictions of existing numerical works are applicable. The radiation and gas pressures are $P_r = 4\sigma T_c^4/3c$ and $P_g = \rho k_B T_c/\mu_0 m_H$, respectively. Thus, in the hottest, innermost regions of SMBH accretion disks, $P_r > P_g$ and the pressure is radiation-dominated. This presents challenges for accurately simulating the behavior of binaries where the secondary is embedded in this region. Investigations of radiation pressure dominated MRI-active accretion disks have found significant departures from α-disk behavior, in which most models in radiation-dominated zones experienced thermal instability (Jiang et al., 2013). Thermal instabilities in accretion disks have been invoked as potential drivers of outburst behavior in cataclysmic variables and FU Orionis objects and have also been shown to potentially drive unique variability signatures in the context of AGN disks (Ross et al., 2017; Habibi & Abbassi, 2019). In addition, opacity transitions in these innermost regions can drive convection and introduce additional variability in the electromagnetic emission (Jiang & Blaes, 2020). It is unclear if the variability behavior within the radiation-dominated region of the parameter space is well-captured by the average conditions tested in typical SMBHB simulations, which tend to simulate locally isothermal, gas-pressure-dominated systems in 2D. This constraint is also useful for identifying where 2D non-isothermal simulations, which are desirable for higher-fidelity determination of the EM variability in these systems, are unlikely to be thermally unstable and thus are more likely to be computationally tractable and produce self-consistent predictions for variability signatures. Thus, ideally, we would like to focus attention on SMBHBs where the secondary is embedded in the gas-dominated part of the disk, where non-isothermal simulations could be performed without issue (e.g., Westernacher-Schneider et al. 2022) and where the results of isothermal simulations are more applicable.

Our third constraint is on the residence time of the secondary at its current location. Depending on the initial separation and local disk conditions, the secondary black hole can be expected to migrate inward through the disk. Many simulations keep the secondary SMBH at a fixed semi-

major axis, running for ~ 1000 orbits. Thus, for the purposes of comparison between models and observations, we constrain the relevant parameter space to those systems whose expected migration distance over 1000 orbits is $< 1\%$ of the initial separation. We calculate migration rates from disk-dominated migration, secondary-dominated migration, and gravitational wave inspiral, as in Haiman et al. (2009b).

We apply these constraints to a SS73 three-zone α-disk model and a constant aspect ratio disk model in order to identify the subset of parameter space where all conditions are satisfied.

4.3.3 Multi-zone α-disk

4.3.3.1 Disk zones

We consider three main zones whose boundaries are delineated by the transition between radiation and gas pressure dominated hydrodynamics and the transition between electron scattering and free-free opacities. The gas-radiation boundary can be found by requiring $P_g = P_r$ and combining equations (4.1a–h), yielding

$$r_{g/r} = 6.75 \times 10^2 \;\; \tilde{\mu}_0^{8/21} \tilde{\mu}_e^{6/7} \tilde{\kappa}_{\rm es}^{6/7} \left(\frac{\dot{m}_{0.1}}{\varepsilon_{0.1}} \right)^{16/21} M_7^{2/21} \alpha_{0.01}^{2/21}. \tag{4.15}$$

Within the radiation dominated zone, we can assume that equation (4.1d) becomes $P = P_r = 4\sigma T_c^4/3c$ and combine equations (4.1a–f) to solve for the scale height in the radiation-dominated zone:

$$H = 1.5 R_g \;\; (\dot{m}_{0.1}/\varepsilon_{0.1}). \tag{4.16}$$

The second zonal boundary we consider occurs in the cooler outer regions of the disk, where the opacity transitions from being dominated by electron scattering to being dominated by free-free absorption. To find the radius of this opacity transition, we require $\kappa_{\rm es} = \kappa_{\rm ff}$ and combine equations (4.1a–h), yielding

$$r_{\rm es/ff} = 8.2 \times 10^3 \;\; \tilde{\mu}_0^{-1/3} \tilde{f}_T^{17/12} \left(\frac{\tilde{\kappa}_{\rm ff}}{\tilde{\kappa}_{\rm es}} \right)^{-2/3} \left(\frac{\dot{m}_{0.1}}{\varepsilon_{0.1}} \right)^{2/3}. \tag{4.17}$$

For the middle zone, $r_{g/r} < r < r_{\rm es/ff}$, the pressure is gas-dominated, so equation (4.1d) becomes $P = P_g = \rho k_B T_c / \mu_0 m_H$ and the opacity is dominated by electron scattering, so $\kappa_R = \kappa_{\rm es}$. We can then combine equations (4.1a-h) to get the scale height in the middle zone,

$$H = 8.74 R_g \ \mu_e^{-1/10} \mu_0^{-2/5} \tilde{\kappa}_{\rm es}^{1/10} f_T \alpha_{0.01}^{-1/10} \left(\frac{\dot{m}_{0.1}}{\varepsilon_{0.1}} \right)^{1/5} M_7^{-1/10} r_3^{21/20}. \tag{4.18}$$

Then, for the outer zone, the pressure is again gas-dominated but the opacity is now dominated by free-free absorption, so $\kappa_{\rm R} = \kappa_{\rm ff} = (8 \times 10^{22}\ {\rm cm^2\ g^{-1}}) \mu_{\rm e} \left[\rho / \left({\rm g\ cm^{-3}} \right) \right] ({\rm T/K})^{-7/2}$. With these, we can again combine equations (4.1a-h) to obtain the scale height for the outer zone:

$$H = 8.66 R_g \ \mu_e^{-1/10} \mu_0^{-3/8} \tilde{\kappa}_{\rm ff}^{1/20} f_T^{143/160} \alpha_{0.01}^{-1/10} \left(\frac{\dot{m}_{0.1}}{\varepsilon_{0.1}} \right)^{3/20} M_7^{-1/10} r_3^{9/8}. \tag{4.19}$$

4.3.3.2 Migration

For the gap-opening secondaries of interest here, migration can be expected to occur in two disk-mediated migration phases, culminating in gravitational wave driven inspiral. At large separations, when the local disk mass is larger than the mass of the secondary, the secondary migrates inward on the viscous timescale of the disk,

$$t_\nu = -\frac{r}{\dot{r}_\nu} = \frac{2}{3} \frac{R^2}{\nu(R)} = 2\pi \frac{R^2 \Sigma(R)}{\dot{M}}, \tag{4.20}$$

analogous to disk-dominated Type-II planetary migration (Lin & Papaloizou, 1986).

At smaller separations, the secondary will be more massive than the local disk and the inertia of the secondary thereby becomes dynamically significant, leading to a slower migration rate than in the disk-dominated case (Syer & Clarke, 1995) on a timescale

$$t_s = -\frac{r}{\dot{r}_s} = q_B^{-k} t_\nu, \tag{4.21}$$

where

$$q_B = \frac{4\pi R^2 \Sigma(R)}{\mu_0} = \frac{2\dot{M}}{\mu_0} t_\nu = \frac{8\dot{m}}{q_s} \frac{t_\nu}{t_{\rm Edd}} \tag{4.22}$$

measures the mass dominance of the local disk vs the secondary and k is a constant of order unity whose value depends on q_B and the opacity (Haiman et al., 2009b).

The final phase of migration, gravitational wave inspiral, is independent of the local disk properties and occurs on a timescale (Peters, 1964)

$$t_{\rm GW} = -\frac{r}{\dot{r}_{\rm GW}} = \frac{5}{16} \frac{GM}{c^3} q_s^{-1} r^4. \tag{4.23}$$

Where the secondary transitions between these different migration modes depends on both the disk parameters and the mass ratio of the binary. We calculate, for each zone, the disk-mediated migration timescales and the transition radii between the different migration phases.

In the radiation-dominated zone, the migration timescales and transition radii are

$$\left.\begin{aligned}
t_\nu &= 8.46 \times 10^8 \text{ yr } \alpha_{0.01}^{-1} \left(\frac{\dot{m}_{0.1}}{\varepsilon_{0.1}}\right)^{-2} M_7 \lambda^{7/2} r_3^{7/2} \\
t_s &= 5.15 \times 10^7 \text{ yr } \alpha_{0.01}^{-10/16} \left(\frac{\dot{m}_{0.1}}{\varepsilon_{0.1}}\right)^{-26/16} M_7^{10/16} q_s^{6/16} \lambda^{35/16} r_3^{25/16} \\
r_{\nu/{\rm s}} &= 2.73 \times 10^3 \ \alpha_{0.01}^{2/7} \left(\frac{\dot{m}_{0.1}}{\varepsilon_{0.1}}\right)^{2/7} M_7^{-2/7} q_s^{2/7} \lambda^{-1} \\
r_{{\rm s}/{\rm GW}} &= 3.78 \times 10^3 \ \alpha_{0.01}^{-10/29} \left(\frac{\dot{m}_{0.1}}{\varepsilon_{0.1}}\right)^{-26/29} M_7^{-6/29} q_s^{22/29} \lambda^{35/29} \beta_{{\rm GW}/{\rm s}}^{16/29} \\
r_{\nu/{\rm GW}} &= 3.64 \times 10^5 \ \alpha_{0.01}^{-2} \left(\frac{\dot{m}_{0.1}}{\varepsilon_{0.1}}\right)^{-4} q_s^2 \lambda^7 \beta_{{\rm GW}/\nu}^2
\end{aligned}\right\}, \tag{4.24}$$

with $\lambda = r_{\rm gap}/a$ being the relative position of the outer gap edge to the secondary, $\beta_{{\rm GW}/{\rm s}} \equiv t_{\rm GW}/t_s$, $\beta_{{\rm GW}/\nu} \equiv t_{\rm GW}/t_\nu$, t_ν being the viscous timescale of disk-dominated migration, t_s the timescale of secondary-dominated migration, $r_{\nu,{\rm s}}$ the radius where migrations transitions from being disk-dominated to secondary-dominated, $r_{{\rm s}/{\rm GW}}$ the radius where migration transitions from secondary-dominated to gravitational wave-dominated, and $r_{\nu/{\rm GW}}$ the radius where migration transitions from disk-dominated directly to gravitational wave-dominated, though skipping the secondary-

dominated phase in this way will only occur for the most massive binaries at near-equal mass ratios. As in Haiman et al. (2009b), we fiducially take $\lambda = 1$, $\beta_{\rm GW/s} = 1$, and $\beta_{\rm GW/\nu} = 0.1$ throughout this work.

In the middle zone, where the pressure is gas-dominated and the opacity is dominated by electron scattering, the migration timescales and transition radii are

$$\left.\begin{aligned} t_\nu &= 9.06\times10^5 \text{ yr } \alpha_{0.01}^{-4/5}\left(\frac{\dot m_{0.1}}{\varepsilon_{0.1}}\right)^{-2/5} M_7^{6/5}\lambda^{7/5}r_3^{7/5} \\ t_s &= 4.05\times10^6 \text{ yr } \alpha_{0.01}^{-1/2}\left(\frac{\dot m_{0.1}}{\varepsilon_{0.1}}\right)^{-5/8} M_7^{3/4}q_s^{3/8}\lambda^{7/8}r_3^{7/8} \\ r_{\nu/\rm s} &= 2.03\times10^4 \ \alpha_{0.01}^{4/7}\left(\frac{\dot m_{0.1}}{\varepsilon_{0.1}}\right)^{-3/7} M_7^{-6/7}q_s^{5/7}\lambda^{-1} \\ r_{\rm s/GW} &= 1.62\times10^3 \ \alpha_{0.01}^{-4/25}\left(\frac{\dot m_{0.1}}{\varepsilon_{0.1}}\right)^{-1/5} M_7^{-2/25}q_s^{11/25}\lambda^{7/25}\beta_{\rm GW/s}^{8/25} \\ r_{\nu/\rm GW} &= 1.26\times10^3 \ \alpha_{0.01}^{-4/13}\left(\frac{\dot m_{0.1}}{\varepsilon_{0.1}}\right)^{-2/13} M_7^{1/13}q_s^{5/13}\lambda^{7/13}\beta_{\rm GW/\nu}^{5/13} \end{aligned}\right\}. \tag{4.25}$$

Finally, in the outer zone, where the pressure is gas-dominated but the opacity is now dominated by free-free absorption, the migration timescales and transition radii are

$$\left.\begin{aligned} t_\nu &= 1.12\times10^6 \text{ yr } \alpha_{0.01}^{-4/5}\left(\frac{\dot m_{0.1}}{\varepsilon_{0.1}}\right)^{-3/10} M_7^{6/5}\lambda^{5/4}r_3^{5/4} \\ t_s &= 5.30\times10^6 \text{ yr } \alpha_{0.01}^{-8/17}\left(\frac{\dot m_{0.1}}{\varepsilon_{0.1}}\right)^{-10/17} M_7^{12/17}q_s^{7/17}\lambda^{25/34} \\ r_{\nu/\rm s} &= 4.13\times10^4 \ \alpha_{0.01}^{16/25}\left(\frac{\dot m_{0.1}}{\varepsilon_{0.1}}\right)^{-14/25} M_7^{-24/25}q_s^{4/5}\lambda^{-1} \\ r_{\rm s/GW} &= 1.73\times10^3 \ \alpha_{0.01}^{-15/111}\left(\frac{\dot m_{0.1}}{\varepsilon_{0.1}}\right)^{-20/111} M_7^{-10/111}q_s^{48/111}\lambda^{25/111}\beta_{\rm GW/s}^{34/111} \\ r_{\nu/\rm GW} &= 9.84\times10^2 \ \alpha_{0.01}^{-16/55}\left(\frac{\dot m_{0.1}}{\varepsilon_{0.1}}\right)^{-6/55} M_7^{-4/55}q_s^{20/55}\lambda^{25/55}\beta_{\rm GW/\nu}^{20/55} \end{aligned}\right\}. \tag{4.26}$$

Scaled to our fiducial parameter values, for comparison with equations (4.24-4.26), the gravi-

tational wave inspiral timescale is

$$t_{\rm GW} = 4.88 \times 10^5 \text{ yr } M_7 q_s^{-1} r_3^4. \tag{4.27}$$

In Figure 4.1, we plot the regions of identified constraints for a range of mass ratios $10^{-3} < q < 1$, masses $10^5\ \mathrm{M}_\odot < M < 10^{10}\ \mathrm{M}_\odot$, separations $10\ \mathrm{R_g} < a < 10^5\ \mathrm{R_g}$, viscosity parameters $10^{-3} < \alpha < 10^{-1}$, and accretion rates $10^{-2} < \dot{m} < 1$. We find that for our fiducial parameter choices, a gap is opened for all mass ratios for separations larger than $20\,\mathrm{R_g}$. Even for very viscous, high accretion rate models, a gap is opened for separations larger than $\sim 20\,\mathrm{R_g}$ for $q \geq 0.1$. The transition from radiation-dominated to gas-dominated is primarily governed by the accretion rate (see Eq. 4.15), with smaller accretion rates moving this transition inward. At sufficiently low accretion rates ($\dot{m} \lesssim 0.01$), however, the inner regions will transition to a radiatively-inefficient advection-dominated accretion flow (Trump et al., 2011), rather than the radiation-dominated thin disk of this model. For our migration criterion, we see that the inner cutoff has no dependence on disk parameters, as this corresponds to the GW-dominated migration phase, which is independent of the disk. For very high viscosities and accretion rates, however, the disk-dominated migration phase is rapid down to radii in our domain of interest, particularly for lower mass ratios for whom the secondary-dominated migration phase begins at smaller radii.

4.3.4 Constant aspect ratio disk

For the constant aspect ratio disk model, the scale height and surface density distributions are prescribed, resulting in a single solution for each of the migration timescales and the corresponding transition radii.

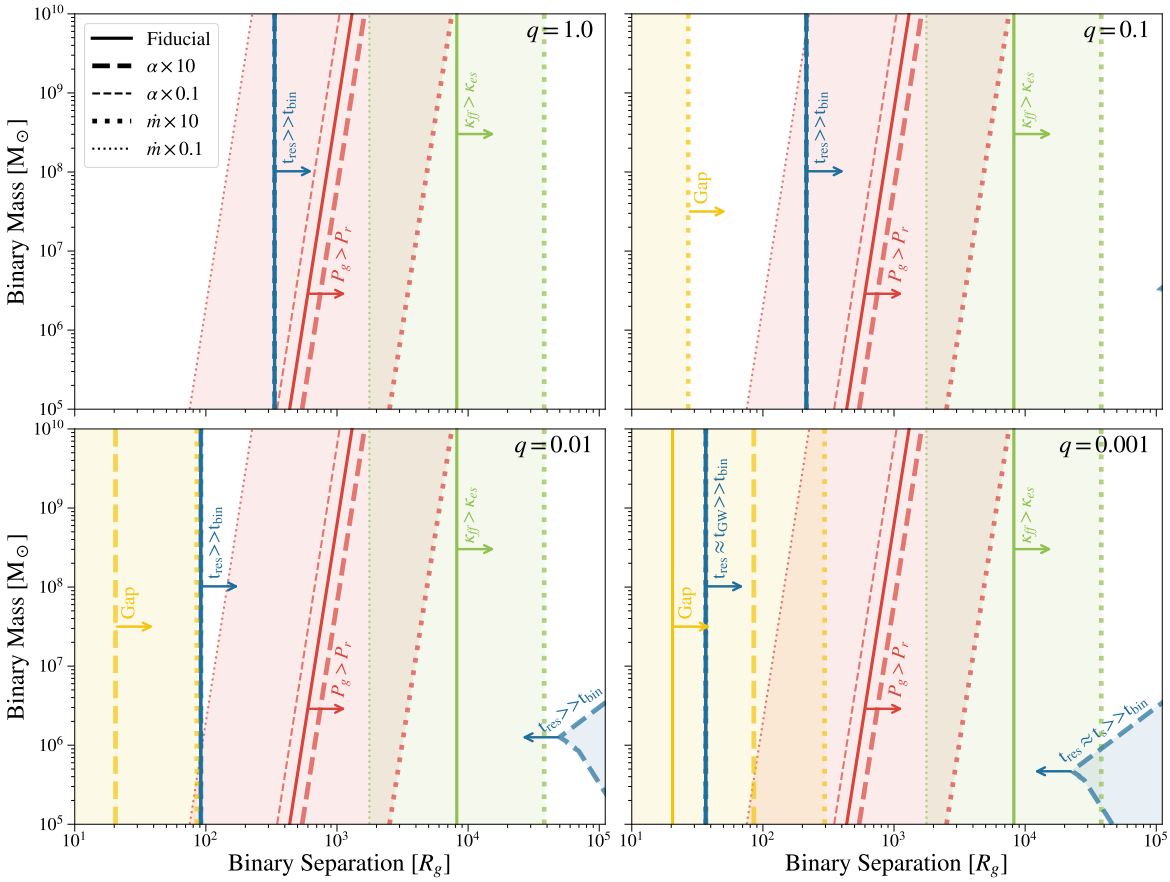


Figure 4.1: Model-dependent constraints, for a range of disk parameter values. For each constraint, the solid line corresponds to our fiducial parameter values of $\alpha = 10^{-2}$ and $\dot{m} = 0.1$. We show how these constraints change when varying α (dashed lines) and $\dot{m}$ (dotted lines) by a factor of 10 (thinner linewidth is a factor of 10 smaller, thicker linewidth a factor of 10 larger). We shade the region covered by each constraint so it is easier to discern which lines correspond to the same constraint. We do not consider changes to the disk composition or the accretion efficiency. We observe that for large α or $\dot{m}$, smaller mass ratios become unable to open a gap (indicated by the yellow contour labeled "Gap") in the innermost part of the disk due to the increased viscous torque. Further, at large α and $q \lesssim 0.01$, the viscous timescale becomes short enough that there is a subset of SMBHBs who rapidly inspiral through the disk-dominated migration phase at large radii, failing to meet our criterion for being considered approximately stationary (indicated by the blue contour "$t_{\rm res} >> t_{\rm bin}$"). Meanwhile, the small-separation cutoff is virtually independent of the disk model, as it is governed by the gravitational wave inspiral. The pressure and opacity transitions (red "$P_g > P_r$" and green "$\kappa_{\rm ff} > \kappa_{\rm es}$," respectively) are both primarily governed by $\dot{m}$, moving inward for lower values and outward for higher ones.

$$\left.\begin{aligned}
t_\nu &= 4.94\times10^2 \text{ yr } M_7\alpha_{0.01}^{-1}h_{0.1}^{-2}r_3^{3/2} \\
t_s &= 3.89\times10^4 \text{ yr } \alpha_{0.01}^{-5/8}q_s^{3/8}M_7^{5/8}\left(\frac{\dot{m}_{0.1}}{\varepsilon_{0.1}}\right)^{-3/8}h_{0.1}^{-5/4}r_3^{15/16} \\
r_{\nu/\mathrm{s}} &= 2.35\times10^6 \ \alpha_{0.01}^{2/3}h_{0.1}^{4/3}M_7^{-2/3}\left(\frac{\dot{m}_{0.1}}{\varepsilon_{0.1}}\right)^{-2/3}q_s^{2/3} \\
r_{\mathrm{s/GW}} &= 4.38\times10^2 \ \alpha_{0.01}^{-10/49}h_{0.1}^{-20/49}M_7^{-6/49}\left(\frac{\dot{m}_{0.1}}{\varepsilon_{0.1}}\right)^{6/49}q_s^{22/49}\beta_{\mathrm{GW/s}}^{16/49} \\
\nu/\mathrm{GW} &= 63.4 \ \alpha_{0.01}^{-2/5}h_{0.1}^{-4/5}q_s^{2/5}\beta_{\mathrm{GW}/\nu}^{2/5}
\end{aligned}\right\}. \tag{4.28}$$

While the pressure and opacity zones do not introduce separate solutions for the migration quantities, they are still relevant for other phenomena (e.g., the thermal instability in the radiation-dominated zone). For the constant aspect-ratio model, the pressure zone transition occurs at

$$r_{\mathrm{g/r}}^{5-\delta} = 7.45\times10^{19} \ \alpha_{0.01}M_7\left(\frac{\dot{m}_{0.1}}{\varepsilon 0.1}\right)^2 h_{0.1}^6 r_0^{1/2-\delta}\left(1-\left(\frac{2}{r_0}\right)^{1/2}\right)^{-1} \tag{4.29}$$

and the opacity transition at

$$r_{\mathrm{es/ff}}^{5-2\delta} = 2.21\times10^{42} \ \alpha_{0.01}^2M_7^2\left(\frac{\dot{m}_{0.1}}{\varepsilon_{0.1}}\right)^{-2} h_{0.1}^{20} r_0^{1-2\delta}\left(1-\left(\frac{2}{r_0}\right)^{1/2}\right)^{-2}. \tag{4.30}$$

For the common $\delta = 0$ case, these give

$$r_{\mathrm{g/r}} = 9.43\times10^3 \ \alpha_{0.01}^{1/5}M_7^{1/5}\left(\frac{\dot{m}_{0.1}}{\varepsilon 0.1}\right)^{2/5} h_{0.1}^{6/5} r_0^{1/10}\left(1-\left(\frac{2}{r_0}\right)^{1/2}\right)^{-1/5} \tag{4.31}$$

and

$$r_{\mathrm{es/ff}} = 2.94\times10^8 \ \alpha_{0.01}^{2/5}M_7^{2/5}\left(\frac{\dot{m}_{0.1}}{\varepsilon_{0.1}}\right)^{-2/5} h_{0.1}^4 r_0^{1/5}\left(1-\left(\frac{2}{r_0}\right)^{1/2}\right)^{-2/5}. \tag{4.32}$$

Figure 4.2 shows the variation of our constraints with the parameters of the constant aspect-ratio model, as Figure 4.1 did for the multi-zone α disk. As before, we consider viscosity parameters $10^{-3} < \alpha < 10^{-1}$, and accretion rates $10^{-2} < \dot{m} < 1$, as well as aspect ratios $0.01 < h < 0.1$. We plot only $\delta = 0$ as it is the simplest and most commonly used in the literature. As h is constant

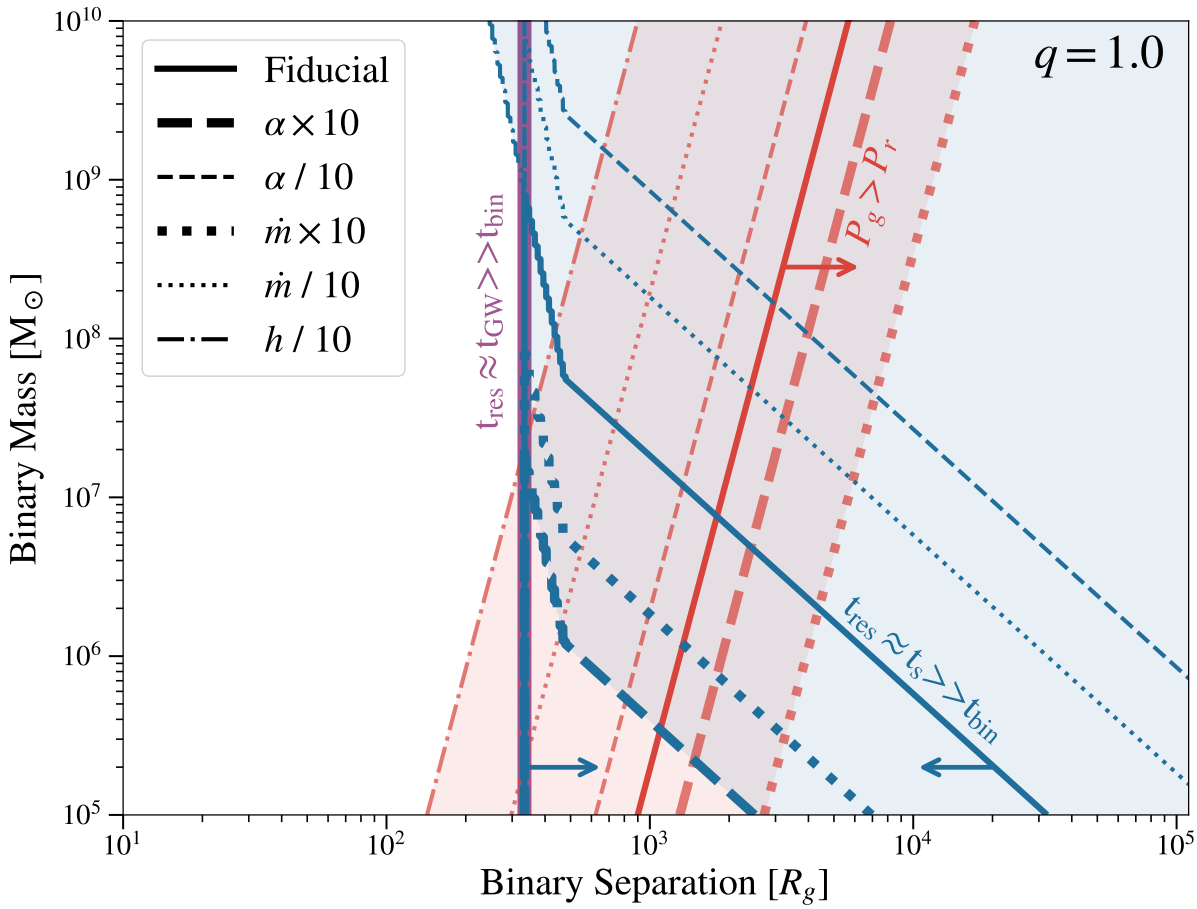


Figure 4.2: Variation of constraints with disk parameters as in Figure 4.1, but for the constant aspect-ratio model. In addition to α and $\dot{m}$, we consider a range of aspect ratios $0.01 < h < 0.1$ (see equations 4.13–4.14, 4.31, 4.32, and 4.28 to see the specific proportionalities of constraints to the disk parameters). As our fiducial $h = 0.1$ is already thicker than the $h \sim 0.01$–0.001 expected of real AGN disks, we consider only a factor of 10 smaller h, shown by a thin dot-dashed line for each constraint. The only visible variation with mass ratio is where the migration rate cutoff lies, and so we plot a single panel for this disk model, with migration contours labeled for each mass ratio. Because there is, by definition, no radial dependence on h, the gap-opening criterion is either met or not met for all $\{M, a\}$ for a given q. The opacity transition occurs, for all disk parameter values considered, at a radius beyond our domain of interest. The pressure transition (red "$P_g > P_r$") behaves much the same as for the multi-zone α-disk, with the strongest dependencies being on $\dot{m}$ and now h. The largest difference between this model and the multi-zone α-disk is seen for our residence time constraint (blue "$t_{res} >> t_{bin}$"). The fiducial $h = 0.1$ results in a thicker disk, which increases the viscosity of the disk and shortens the viscous timescale. As a result, both disk-dominated and secondary-dominated migration are more rapid and leave only a narrow space of $\{M, a\}$ combinations which do not significantly migrate over $10^3\ t_{bin}$. The sloped portion of the residence time contour corresponds to where the disk-mediated migration meets our constraint, but there is also maximum separation, set by the GW inspiral timescale, below which any combination of disk parameters fails to meet our residence time constraint. We highlight this boundary with a thick purple line, labeled "$t_{res} = t_{GW} = 10^3\ t_{bin}$".

in this model, gap-opening depends only on q, with $q > 5 \times 10^{-3}$ opening a gap for $\alpha = 0.01$ and $h = 0.1$ and $q > 5 \times 10^{-5}$ opening a gap for $h = 0.01$. The location of the radiation-gas transition depends primarily upon the disk aspect ratio and the accretion rate, but generally occurs in a similar range as for the multi-zone α-disk case, $10^2 \lesssim r_{\mathrm{g/r}} \lesssim 10^4$.

4.4 Results & Discussion

In this section, we combine all of the outlined observational and model constraints from Section 4.3, including GW detection limits for *LISA*, contemporary PTA results, and projected future PTA results including SKA data. We examine the resulting regions of the mass-separation parameter space, discuss the implications of these constraints for various subsets of the SMBHB parameter space, and examine where previous numerical studies lie in relation to these constraints.

The analysis in Figures 4.3 and 4.4 can be compared to the one presented in Figure 14 of D'Orazio et al. (2013), extended to include additional constraints from GW instrument sensitivities and the radiation-gas pressure transition boundary. Unlike D'Orazio et al. (2013), we do not include constraints based on gravitational stability of the disk, as perturbations from a secondary keep the disk stable out to larger radii than is the case for an unperturbed disk. We also use a more relaxed gap-opening criterion, requiring only that the secondary is able to open a gap at a given separation rather than maintain it throughout migration as in the cavity criterion derived by Kocsis et al. (2012a) and used by D'Orazio et al. (2013).

4.4.1 Multi-zone α-disk

For a self-consistent multi-zone α-disk mode, there are few regions of the mass–separation parameter space in which detectable SMBHB gravitational wave sources can be expected to exhibit predicted EM variability signatures. The most limiting constraint is that the majority of SMBHBs that are detectable by LISA or PTAs require relatively small separations ($a \lesssim 10^2\ R_g$), well within the radiation-dominated zone. The population which is GW-detectable and outside the radiation-dominated zone is generally biased toward lower redshifts and higher mass ratios, with no binaries

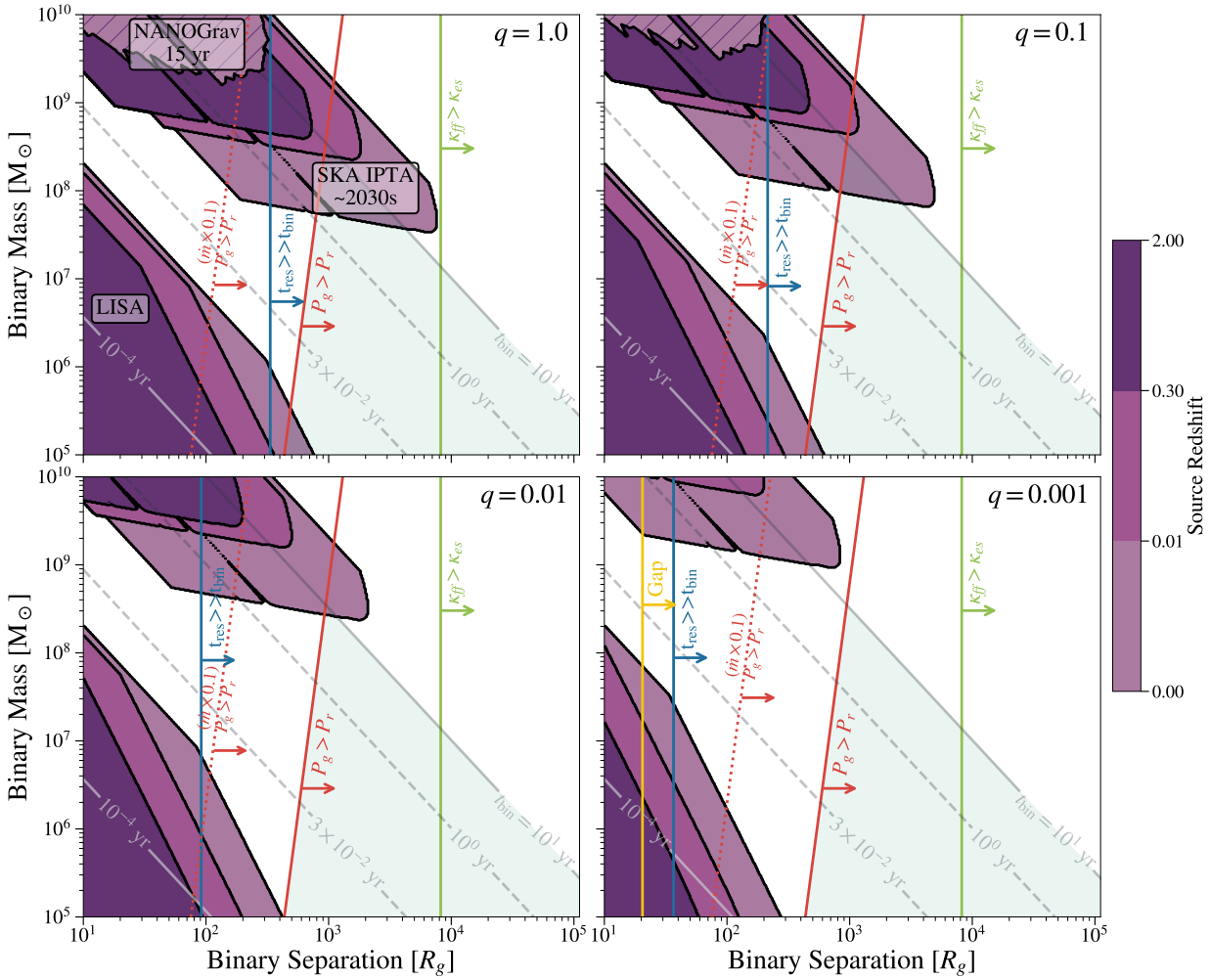


Figure 4.3: Illustration of our constraints on the SMBHB parameter space, with the region shaded in soft green being the subset of the parameter space which meets all our constraints. The filled purple contours show the redshift at which a given combination of binary $\{M,q,a\}$ is detectable by GW detectors. The hatched contour shows the sensitivity for the recent NANOGrav 15-year dataset at a redshift of $z = 0.01$. The red line (labeled "$P_g > P_r$") indicates the transition from radiation to gas-dominated pressure for our fiducial disk parameters, with the dotted red line showing where this transition occurs for $\dot{m} = 0.01$, which produces a more generous constraint on the applicable domain. The green line (labeled "$\kappa_{\rm ff} \gg \kappa_{\rm es}$") shows where the opacity transitions from being electron scattering-dominated to free-free absorption-dominated. The blue line (labeled "$t_{\rm res} >> t_{\rm bin}$") marks where the binary will inspiral by $> 1\%$ of its initial separation in 10^3 orbits. The yellow line (labeled "Gap") indicates where in the disk a gap can be opened, though this is relevant only at $q = 10^{-3}$, as the larger mass ratios are capable of opening a gap anywhere in our domain of interest for our fiducial disk. Finally, in grey, we show the binary orbital timescale for 10 years, 1 year, 2 weeks, and 1 hour, encompassing a range of reasonable monitoring cadences. The binaries which meet all these constraints, and which we thus expect to both behave as predicted by the simulation literature and be observable, is very narrow. Only for $q = 1$ do we have any GW-detectable binaries at a redshift of $z \geq 0.3$ for our fiducial disk parameters.

having $q \leq 0.01$ being GW-detectable at redshifts of $z \geq 0.3$ for our fiducial accretion rate $\dot{m} = 0.1$. For equal mass binaries, the most well-studied mass ratio regime in simulations, most of the GW-detectable population that lies outside the radiation-dominated zone has orbital periods longer than 10 years, making confirmation of binary candidacy via EM periodicity challenging. Further, for our choice of fiducial disk parameters, no part of the SMBHB parameter space is both outside the radiation-dominated zone and detectable by currently-active GW instruments.

The outlook is more optimistic for AGN with lower mass accretion rates. The transition between the radiation and gas pressure dominated zones is shifted inward to within a few 100 R_g for accretors at $\dot{m} = 0.01$ (the dotted red line in Figure 4.3). With the gas pressure dominated zone extended to smaller radii, SMBHBs of interest are detectable with GWs out to $z = 2$ for $q \geq 0.01$. For larger mass ratios $0.1 \leq q \leq 1$, the primary constraint on which binaries can be expected to have EM variability like that in constant-separation, gas-dominated simulations becomes the residence timescale of the binary rather than the pressure transition. We note, however, that at sufficiently low accretion rates ($L_{\rm acc}/L_{\rm Edd} \lesssim 10^{-3}$) the inner disk edge is truncated at $R \sim 80\ R_g$ by a radiatively inefficient accretion flow (RIAF) (Trump et al., 2011), requiring a different disk model than is considered here or in the numerical works we discuss.

Ignoring the radiation pressure constraint, there are SMBHBs which are GW-detectable out to $z = 2$ at all mass ratios, though for $q \leq 0.01$ these are generally restricted to either extremely massive $M \sim 10^{10}$ M$_\odot$ or very low-mass $M \sim 10^5$ M$_\odot$ systems. We observe that the constraint that the binary separation changes by $< 1\%$ over 1000 orbits becomes less strict at lower mass ratios, as GWs don't dominate the migration until much smaller separations for low-q binaries. We also note that this constraint is always less strict than the radiation pressure constraint for our fiducial disk parameters, such that any simulation where the secondary is placed outside the radiation-dominated zone can be modeled as a fixed-orbit binary.

4.4.2 Constant aspect-ratio disk

In order to compare our results directly to the parameter space of simulated SMBHBs in the literature, we also calculate the constraints to be self-consistent with the oft-employed constant aspect-ratio disk model (Figure 4.4). The substantive differences are that the pressure transition occurs further out for fiducial parameters than it does for the multi-zone α-disk and that inspiral occurs at slightly smaller radii for high-mass ($M \gtrsim 10^9$ M$_\odot$ at $q = 1$ down to $M \gtrsim 10^8$ M$_\odot$ at $q = 10^{-3}$) binaries. But for the $h = 0.1$ common in the literature and our fiducial $\dot{m} = 0.1$, there are no binaries in the gas-dominated regime that are GW-detectable beyond $z = 0.01$. However, similar to the previous case, the pressure transition will occur at smaller radii for thinner disks or those that have lower accretion rates. While an aspect ratio as thin as the $h = 0.01$ case shown in Figure 4.4 is rarely used in numerical simulations, it is closer to that of real AGN disks and, optimistically, implies GW-detectable binaries in the gas-dominated regime out to $z = 0.3$ for mass ratios $q \geq 0.01$.

4.4.3 Comparison to Existing Numerical Works

To more fully understand the SMBHB parameter space probed by existing numerical works, we want to directly compare the SMBHB parameters and modeling choices stated in these works to the constraints discussed above. Figure 4.5 shows a sample of SMBHB simulations which specify a mass and separation for their work. We note, however, that the majority of works in this space utilize a scale-free setup, wherein the mass and separation are unspecified and results can be rescaled. These scale-free setups come at the cost, however, of including less robust physics, restricted to isothermal evolution, limiting their applicability. We see that, of those works which do specify a mass and separation, only those dedicated to GW inspiral do so in a regime detectable by GW instruments. While Whitley et al. (2024) and Farris et al. (2015) are stationary-orbit simulations which appear to be in the inspiraling regime, we note that Whitley et al. (2024) uses a mass ratio of $q = 0.01$, placing their binary outside of this regime, and Farris et al. (2015) worked in a scale-free setup, with the values plotted here being only their chosen rescaling for discussing

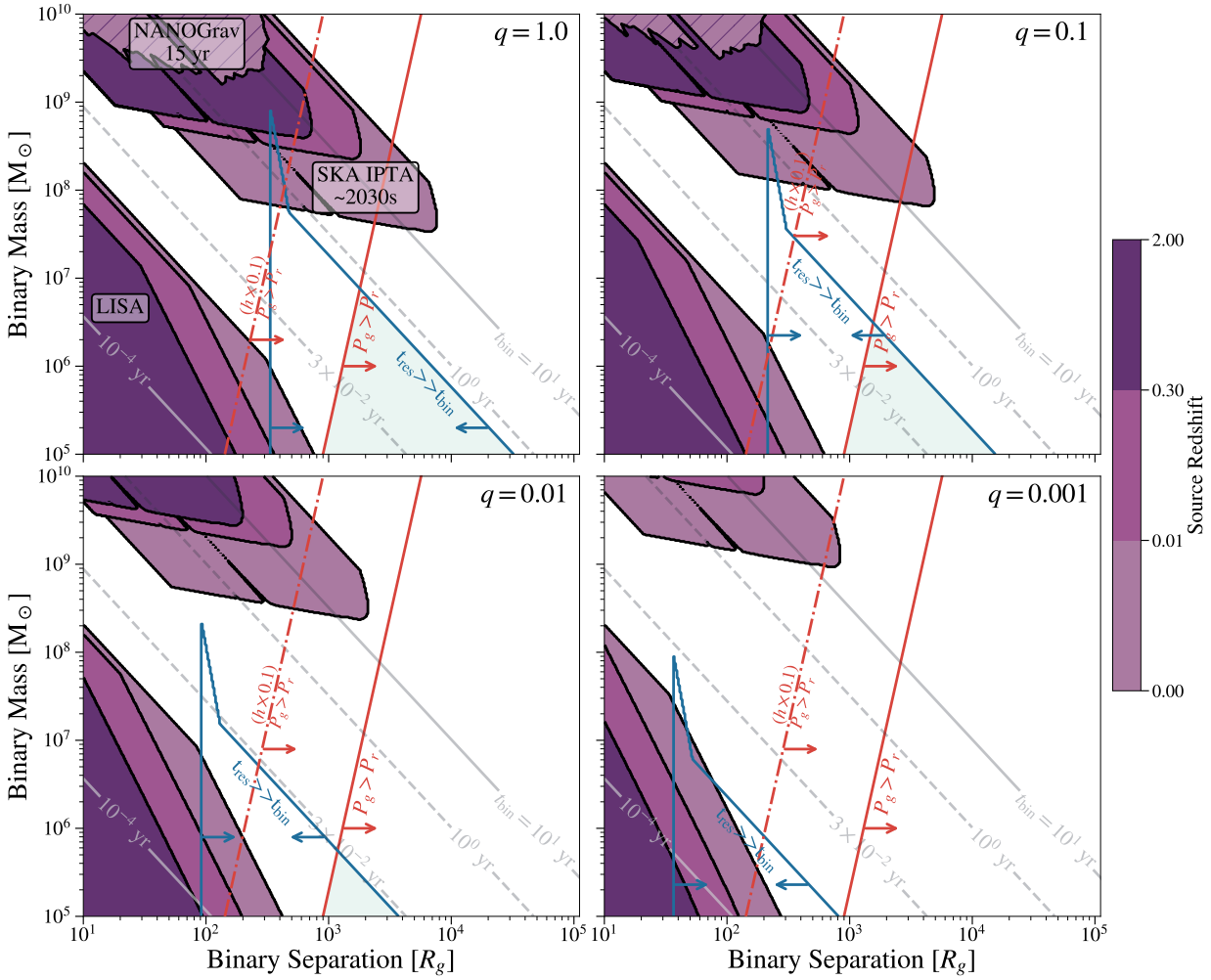


Figure 4.4: Illustration of all constraints as in Figure 4.3, but for the constant aspect-ratio model. Highlighted in soft green is the effective region of applicability of simulations which use this model in a gas-pressure-dominated setup with a stationary binary. Here, the pressure transition, indicated by the red line labeled "$P_g > P_r$," occurs further out, leaving no SMBHBs which meet all our constraints at a redshift beyond $z = 0.01$. The short viscous timescale resulting from the large $h = 0.1$ in the fiducial model also results in a much smaller range of $\{M, a\}$ where the binary is approximately stationary over typical simulation durations (this boundary being indicated by the blue contour labeled "$t_{\rm res} >> t_{\rm bin}$"). The span of $\{M, a\}$ to which gas-dominated, stationary binary simulations are applicable shrinks as q decreases, as the region where the binary is stationary moves inward into the radiation-dominated part of the disk. Note also that for the fiducial $h = 0.1$, $\alpha = 0.01$, a gap cannot be opened for $q \lesssim 0.005$.

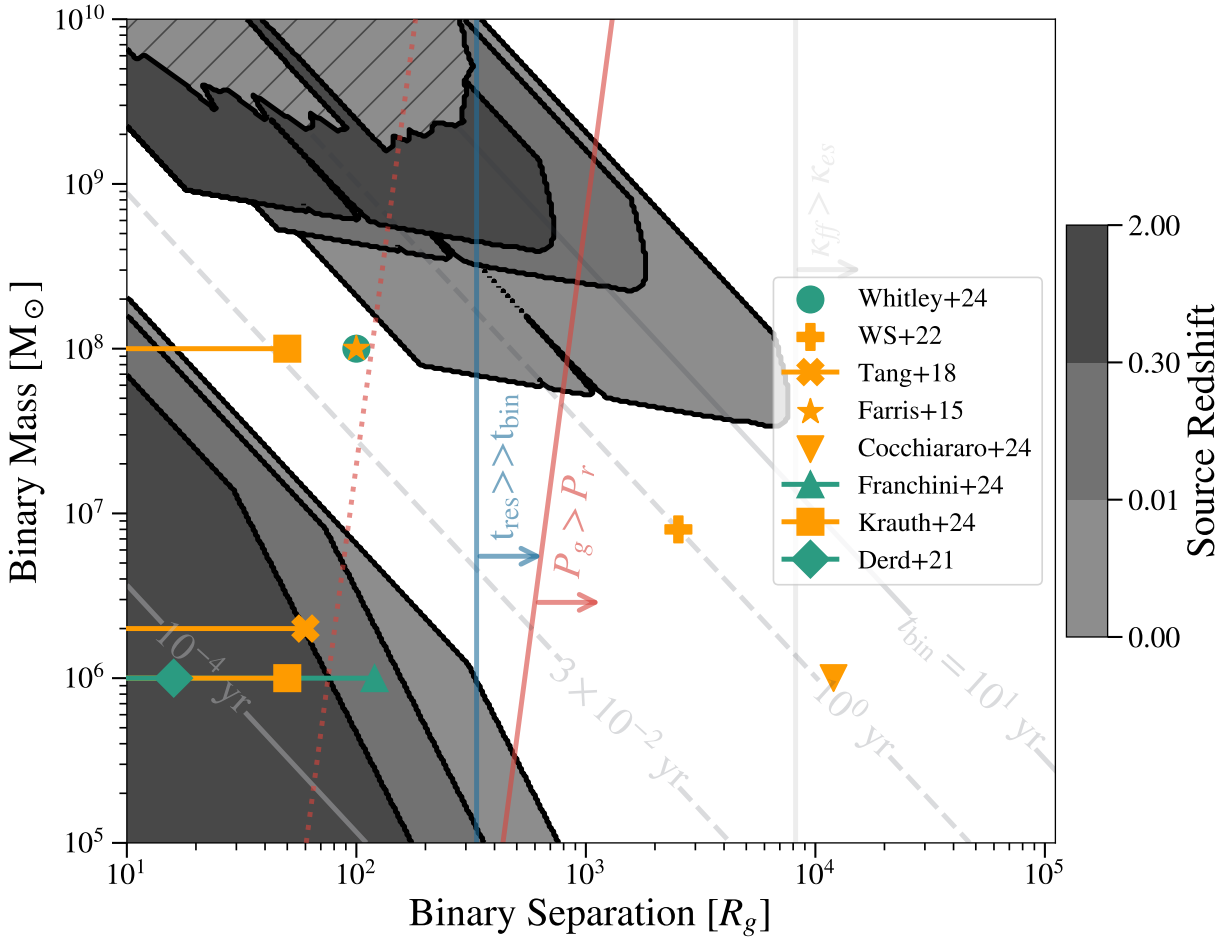


Figure 4.5: Sample of numerical studies which specify M and a overplotted on the $q = 1$ panel of Figure 4.3. Works which use an isothermal equation of state are plotted in teal, while those that modeled the thermal evolution are plotted in orange. Inspiraling simulations are represented by a symbol at the initial separation and a line going down towards merger. Note that a few of the works shown explored mass ratios below unity (namely, $q = 10^{-2}$ for Whitley et al. (2024), $q \leq 10^{-3}$ for Derdzinski et al. (2021), and $q = 0.1$ for Cocchiararo et al. (2024)). For these, the primary differences to bear in mind are that the inspiral threshold will occur at smaller separations, and the GW detection limits cover less space in both mass and separation. Of the works shown, only the inspiraling ones enter the GW-detectable space. None of the works shown include radiation pressure, though the majority are performed in the radiation-dominated regime.

their results. This does, however, limit the inferences that can be robustly made for that chosen rescaling.

We emphasize, in particular, that regardless of binary or disk modeling choices, none of these works includes the effects of radiation pressure (though some, like Whitley et al. (2024) and Westernacher-Schneider et al. (2022) approximate its effect by increasing the gas pressure). While there are GW-detectable systems in the physical regime probed by gas-dominated simulations, they occupy a fairly narrow range of the $\{M, q, a\}$ parameter space, limited to $q \gtrsim 10^{-2}$ and, for *LISA*, $10^5\ \mathrm{M}_\odot < M < 3 \times 10^5\ \mathrm{M}_\odot$ and $4 \times 10^2\ \mathrm{R_g} < a < 8 \times 10^2\ \mathrm{R_g}$ or, for IPTA, $4 \times 10^7\ \mathrm{M}_\odot < M < 4 \times 10^8\ \mathrm{M}_\odot$ and $10^3\ \mathrm{R_g} < a < 4 \times 10^3\ \mathrm{R_g}$, with GWs being detectable at $z = 0.3$ only for $q \sim 1$. The majority of GW-detectable systems are at small separations, in the radiation-dominated part of the disk and quickly migrating. Based on these results, future numerical studies of SMBHB systems will need to account for both radiation pressure and migration in order to make robust predictions of EM counterparts for future GW sources. Radiation-dominated disks are thermally unstable, and this instability manifests unique variability in the system (Ross et al., 2017; Habibi & Abbassi, 2019), which will result in potentially different variability signatures for SMBHBs in this regime than the signatures seen in the gas-dominated simulations performed to date. It should be noted that non-hydrodynamic sources of variability (e.g., Doppler boosting) should remain viable at all separations, though Tang et al. (2018) finds that this is sub-dominant to hydrodynamically-induced variability.

4.4.4 Caveats and Additional Considerations

We have considered here only circular binaries in regards to both GW detectability and migration timescales. Many works have investigated how eccentricity of the binary orbit affects the torques and accretion rates onto these systems (Westernacher-Schneider et al., 2022; Muñoz et al., 2019; Miranda et al., 2017) and how that eccentricity evolves over time (D'Orazio & Duffell, 2021; Siwek et al., 2024). In particular, D'Orazio & Duffell (2021) find that binaries with initial eccentricity $e \lesssim 0.1$ evolve towards $e = 0$, while those with $e > 0.1$ evolve towards $e \approx 0.4$. Further, they

find that the $e = 0$ binaries migrate outwards, while the $e = 0.4$ ones migrate inward, implying that binaries in the inspiral regime relevant to GW detection may be more likely to be on eccentric orbits than circular ones. This bias towards GW-detectable binaries having non-negligible eccentricity is similarly borne out in the analysis of inspiraling binaries from Siwek et al. (2024), who find that disk torques drive migrating binaries up to a peak of $e \sim 0.5$ before GW emission begins to circularize the binary as it approaches merger.

Another caveat is that the sensitivity of PTAs can be improved if the sky location of a candidate source is known a priori via, for example, the EM periodicity suggested by simulations. Thus, the actual population of SMBHBs with behavior like that observed in gas-dominated simulations and detectable by future PTA measurements may be larger than what is shown here.

We see throughout this analysis that the frequency gulf between PTAs and LISA is in the approximate middle of our "human-observable" range of orbital periods ($\sim$ 1 week to $\sim$ 1 year). This space covers a wide range of separations (10–10^3 R_g) for nearly all reasonable binary masses (10^6–10^9 $M_\odot$) and corresponds to a convenient cadence for various all-sky monitoring programs. The Rubin Observatory, Panoramic Survey Telescope and Rapid Response System (Pan-STARRS), Palomar Transient Factory (PTF), Zwicky Transient Facility (ZTF), Sloan Digital Sky Survey, and Catalina Real-time Transient Survey (CRTS) all have wide-sky coverage with an observing cadence of a few days to a few weeks, excellent for sampling the $\sim$month long periods in the GW frequency gap. A future GW observatory covering this frequency range would be ideal for expanding the population of EM-identified candidates that can be followed-up on with GW data but would require an impractically large ($\sim$AU-scale) interferometer.

4.5 Conclusions

We have examined several observational and modeling constraints regarding the SMBHBs embedded in a thin accretion disk. From these, we compared the subsets of the SMBHB $\{M, q, a\}$ parameter space which are GW-detectable and those whose EM variability can be expected to behave like that seen from the simulation literature, which has worked exclusively with gas-dominated

pressure models. We have also reviewed a subset of numerical works which specify a mass and separation for the binary and how those choices relate to our constraints. Our main findings can be summarized as follows:

1. For fiducial disk properties $\alpha = 0.01$, $\dot{m} = 0.1$, and $\varepsilon = 0.1$, few SMBHBs which behave like those in gas-dominated, steady-state orbital separation simulations will have an observable GW counterpart. Even with SKA incorporated into IPTA efforts, binaries with a periodic EM signal like that seen in such simulations will only be visible out to $z = 0.3$ in a narrow range of masses, and with orbital periods requiring prohibitively long time baselines ($\gtrsim 10$ yr), complicating finding such binaries via EM periodicity to begin with. However, at larger separations where each SMBH possesses its own broad line region, cross-correlation analysis of individual broad emission lines may be used to infer the presence of a SMBHB with much shorter time baselines (Dotti et al., 2023).

2. For lower accretion rates than our fiducial 10% of the Eddington rate, the pressure transition moves inward and so a broader population of binaries can be expected to behave as seen in gas-dominated simulations at these lower accretion rates. However, for systems inspiraling towards merger, it remains expected that the secondary will be in the radiation-dominated region for most or all of the inspiral. It would therefore be prudent for future works to determine how this radiation-dominated regime will affect the EM counterpart of systems as they approach merger, especially as such systems constitute the loudest and furthest GW-detectable sources.

3. The majority of the parameter space, regardless of disk parameters, is in the radiation-dominated regime, the GW inspiral regime, or both. While simulations have been done to characterize the EM signatures for the inspiral-to-merger phase (Tang et al., 2018), these have not yet been done while accounting for radiation pressure, due to the technical difficulty of incorporating radiation pressure in 2D and the computational expense of evolving these systems for the required timescales with full radiation hydrodynamics in 3D. Understanding

the EM counterparts of SMBHB systems most visible to GW detectors will require overcoming these challenges in order to self-consistently model the physics of radiation-dominated inner regions of AGN disks.

4.6 Acknowledgements

A.K. would like to acknowledge support provided by NASA through the NASA Hubble Fellowship grant #HST-HF2-51463.001-A awarded by the Space Telescope Science Institute, which is operated by the Association of Universities for Research in Astronomy, Incorporated, under NASA contract NAS5-26555.

CHAPTER 5

Conclusion

We are on the cusp of an exciting leap forward in our understanding of supermassive black hole binaries. With the recent detection of a gravitational wave background by PTAs and the approaching launch of LISA, we are approaching an era of direct detections of individual SMBHBs. Powerful new observatories, like the Vera Rubin Observatory, Roman Space Telescope, and ATHENA X-ray mission, will come online over the next decade, enabling deeper searches for SMBHBs and more robust study of the most promising candidates. Alongside these observational advancements, numerical simulations must continue to explore more sophisticated treatments of these systems in order to better guide the hunt for SMBHBs.

The work presented in this dissertation has focused on the electromagnetic signatures of low mass ratio binaries embedded in a thin disk, with a particular focus on high-energy periodic emission from shocks. I have also considered the regime of the SMBHB parameter space which is adequately probed by typical modeling choices used in the SMBHB simulation literature in comparison with the space accessible to photometric surveys and gravitational waves observatories. In this chapter, I summarize the findings of this work and discuss the future of similar work and the field more broadly.

5.1 Summary of Findings

This research has used numerical simulations, both with and without explicit thermal evolution, along with analytical calculations, to identify unique EM signatures for SMBHBs and to determine the observable space in which these predicted signatures are applicable. This has highlighted the importance of shocks as a source of binary-driven variability, that these shocks can be adequately monitored without the expense of thermal evolution, and that current simulations only probe a very narrow slice of the GW-observable SMBHB parameter space.

5.1.1 Simulation Predictions of EM Signatures from Supermassive Black Hole Binaries

To better characterize the time-varying emission of SMBHBs, it is useful to understand how the lightcurve changes as a function of wavelength, beyond what can be inferred from the proxy of accretion rate. In Chapter 2, we approached this by implementing a blackbody cooling scheme, tracking energy radiated away from the system via this scheme and the effective temperature of the gas radiating this energy. In this way, we were able to reconstruct the system's spectral energy distribution as a function of time, obtaining a lightcurve for any wavelength or waveband of interest. We found that there was significant X-ray variability driven by shocks, occurring when accretion streams feeding the secondary's minidisk would be periodically rejected and slam into the edge of the gap in the circumbinary disk. Additionally, these shocks resulted in a persistent hard X-ray presence in the continuum emission, similar to that seen in Farris et al. (2015).

In Chapter 3, we demonstrated that the shock-driven variability discovered in Chapter 2 can be recovered even with the locally isothermal equation of state commonly used in SMBHB simulations. We found, as was later seen in Dittmann & Ryan (2024), that the accretion rate is modulated on the binary orbital timescale for $q = 10^{-2}$, lower than the $q \sim 0.05$ cutoff for variability seen for thicker disk models (D'Orazio et al., 2016). Further, we found that the shock variability and accretion variability are correlated with one another, with the peaks in shock variability lagging peaks in accretion rate by about half an orbital period. As the accretion disk is bright in optical/UV bands and the shocks are expected to produce bright X-ray emission (Tang et al., 2018), we sug-

gest this multiwavelength correlated variability as a more robust signature of binary accretion than single-wavelength periodicity alone.

5.1.2 Applicability of Simulation Predictions to the Observable Parameter Space

The majority of SMBHB simulations have used a similar disk model: a constant aspect ratio $H/R = 0.1$, an α-viscosity prescription with $\alpha = 0.01$–0.1, and no contribution from radiation pressure. When deciding how to change this model for future efforts, it is necessary to first understand which systems the current model describes well (i.e., what systems can be expected to behave like the fiducial simulation model?). In Chapter 4, we considered a range of relevant observational and modelling constraints on the SMBHB parameter space, including sensitivity of GW observatories, disk-mediated migration rates, and the radius where a given disk will transition from being gas-dominated to radiation-dominated. We applied these constraints in the context of both the common constant H/R disk and the multi-zone SS73 disk to identify where existing predictions from gas-dominated simulations are applicable and what additional physics is most important to incorporate in future models to make predictions applicable to GW-detectable SMBHBs. We found that, for our fiducial disk parameters, there is only a very narrow range of binary $\{M, q, a, z\}$ which are GW-detectable and in the gas-dominated regime probed by existing simulations. The majority of GW-loud binaries are instead in the radiation-dominated zone, necessitating radiation hydrodynamics to make accurate predictions about the EM counterparts of these systems.

5.2 Future Directions

This thesis work found that shocks driven by accretion material flung into the gap/cavity edge by the binary are a significant source of periodic variability at high energies. This variability source should be further explored for a range of binary masses, mass ratios, and separations as well as different orbital eccentricities and disk properties in order to better characterize its significance. Given recent findings that SMBHBs are drawn to a critical eccentricity $e \sim 0.45$ (e.g., D'Orazio & Duffell, 2021), exploring how the signal changes at this eccentricity is especially interesting.

Particular focus should be paid to the correlation with accretion variability and whether the phase offset between the two is dependent on the binary parameters as, if this is the case, then this signature could help further constrain the parameters of a candidate binary beyond the period inferred from single-wavelength variability.

Observationally, candidate SMBHBs already identified via photometric periodicity can be further investigated for correlated X-ray/UV variability, particularly if future numerical work demonstrates that this signature is robust for a wide range of binary and disk parameters. For particularly promising candidates with appropriate periods, an observing program could be performed to collect simultaneous X-ray and UV data with, e.g., *Swift*.

In Chapter 4, we note that the exclusion of radiation pressure in SMBHB simulations limits their applicability to systems which are in the gas-dominated part of the disk. For fiducial disk conditions, the majority of GW-detectable binaries will be in the innermost radiation-dominated zone of the disk. The thermal instability for a radiation-dominated disk leads to distinct variable behavior from the gas-dominated case, but also renders 2D simulations intractable. Future 3D simulations with full radiation hydrodynamics are necessary to characterize the EM counterparts expected for binaries in the GW-detectable regime, though the computational expense of evolving these for the hundreds to thousands of orbits required to reach a steady state remains prohibitive.

5.2.1 Final Remarks

The recent evidence of a gravitational wave background found by PTAs marks the beginning of a new era for low-frequency gravitational wave detections. As new pulsars are discovered and added to the PTAs, existing pulsars are monitored for longer, and powerful radio observatories like the Square Kilometer Array come online, the signal-to-noise ratio of PTAs will continue to increase, leading to an eventual high-confidence detection of the GWB and possibly even of individual binaries in the coming years. Detecting binaries with GWs will enable follow-up EM observations which probe how these binaries interact with their environments. Characterizing the EM emission of GW-confirmed binaries will also inform future EM searches for binary candi-

dates. Inversely, incorporating the binary period and mass inferred from photometric periodicity can significantly improve detectability of that candidate with GWs (Liu & Vigeland, 2021). In the 2030s, with the advent of LISA, the detection of inspiralling and merging SMBHBs will provide new insights on this final phase of the SMBHB lifespan. While LISA's sky localization is poor, analysis by Mangiagli et al. (2022) finds that a handful of joint LISA-EM observations of the EM counterpart to SMBHB inspiral may nonetheless be possible over the course of the planned 4-year mission.

While PTAs and LISA are specifically focused on SMBHBs, new EM observatories coming online in the next decade will also play a role in multimessenger study of GW-detected binaries and in the continued search for EM-identified candidates. In particular, the Vera Rubin Observatory (VRO), expected to see first light in the next year, is expected to survey tens of millions of quasars (Xin & Haiman, 2021). With an observing cadence of a few days, VRO will be able to densely sample lightcurves for these millions of quasars, resulting in a substantially lower false positive rate compared to the Catalina Real-Time Transient Survey (Witt et al., 2022).

The future is bright for both EM and GW searches for SMBHBs. It is the responsibility of numerical work to provide accurate models of SMBHB behavior to better inform the observational search. In turn, confirmation and further study of real SMBHBs will help to constrain their formation, evolution, and accretion behavior, which informs future numerical work. The results presented in this dissertation provide insights for both of sides of this effort. My numerical work has identified a novel, multiwavelength, correlated EM signature which may be used to identify candidate SMBHBs or follow up on existing ones. And my analysis of the binary parameter space accurately modeled by existing numerical results emphasizes the importance of biting the radiation hydrodynamics bullet in order to characterize the EM counterparts to the SMBHB inspirals and mergers that will be detected in the decade to come.

APPENDICES

APPENDIX A

A.1 2D Pressureless Accretion

To test the accretion routine developed for this work, we devised a setup for pressureless accretion of gas onto a central point mass. In this, we have a central, accreting point mass embedded in a medium of uniform surface density Σ and of negligible temperature T. We use an isothermal equation of state to ensure that the temperature and, correspondingly, pressure remain negligible throughout the simulation. To determine success, we compare the results to the analytic accretion rate as a function of time, derived below.

Because the initial conditions are uniform and the only force acting on the gas is radial, the problem is at all times azimuthally symmetric, and we need only to consider the evolution in r. Then, because the gas at a given radius does not interact with the gas at any other radii, we can restrict ourselves further to considering the evolution of a ring of gas with radius r, width dr, and mass m.

In general, the accretion rate onto a point mass in a 2D medium is

$$\dot{M}(t) = 2\pi r_a \Sigma_a(t) v_a(t), \tag{A.1}$$

where r_a is the accretion radius of the point mass (i.e., the radius within which gas is being removed in the simulation), and $\Sigma_a(t)$ and $v_a(t)$ refer to the surface density and velocity of the gas at the accretion radius as a function of time.

The velocity is trivially solved for from the conservation of energy as

$$v_a(t) = \sqrt{2GM\left(\frac{1}{r_a} - \frac{1}{r_0(t)}\right)},$$

where M is the mass of the accretor and r_0 is the original radius of the gas ring currently at r_a. Restricting ourselves to the case where $r_a \ll r_0$ (i.e. to times where the gas currently being accreted started far from the accretor), this becomes

$$v_a = \sqrt{\frac{2GM}{r_a}}. \tag{A.2}$$

Next, we need to solve for the surface density at the accretion radius as a function of time, $\Sigma_a(t)$. From continuity, we know that for any infinitesimally thin ring of mass m_0 the total mass m_a of that ring when it collapses to r_a must obey

$$m_a = m_0,$$

and therefore

$$\Sigma_a = \Sigma_0 \left(\frac{r_0}{r_a}\right)\left(\frac{dr_0}{dr_a}\right).$$

Because the differential force of gravity on the gas at r_0 versus the gas at $r_0 + dr_0$, the ring will stretch as it moves inward, and so $dr_a \neq dr_0$. To compute their ratio, we must first solve for the radial position of a ring as a function of time. Starting from energy conservation, we have

$$\frac{v^2}{2} - \frac{GM}{r} = -\frac{GM}{r_0}.$$

Since velocity is only radial, $v = dr/dt$ and we get

$$\frac{dr}{dt} = -\sqrt{2GM}\sqrt{\frac{1}{r} - \frac{1}{r_0}}.$$

Integrating,

$$-\int_0^t \sqrt{2GM}dt = \int_{r_0}^r \left(\frac{1}{r} - \frac{1}{r_0}\right)^{-1/2} dr.$$

Making the substitution $\frac{r}{r_0} = \cos^2(\psi/2)$ and integrating, we obtain

$$\sqrt{2GM}t = \frac{r_0^{3/2}}{2}\left(\psi + \sin\psi\right),$$

which simplifies to

$$\sqrt{2GM}t = \frac{r_0^{3/2}}{2}\left(2\arccos\left(\sqrt{\frac{r}{r_0}}\right) + \sin\left(2\arccos\left(\sqrt{\frac{r}{r_0}}\right)\right)\right),$$

and we can rewrite as

$$\sqrt{2GM}t = r_0^{3/2}\left(\arccos\left(\sqrt{\frac{r}{r_0}}\right) + \sqrt{\frac{r}{r_0}}\sqrt{1 - \frac{r}{r_0}}\right).$$

For the case where $r \ll r_0$ (as will be the case at late times near the accretion radius), we can Taylor expand the arccos and the terms inside the radicals to third order in $\sqrt{r/r_0}$ and obtain

$$\sqrt{2GM}t = \frac{\pi}{2}r_0^{3/2} - \frac{2}{3}r^{3/2}.$$

Thus, for $r = r_a \ll r_0$, we have

$$r_0(t) = \left(\frac{4}{3\pi}r_a^{3/2} + \frac{2}{\pi}\sqrt{2GM}t\right)^{3/2}. \tag{A.3}$$

Inverting this, we obtain the time taken for a ring starting at r_0 to fall to r_a:

$$t_a = \sqrt{\frac{r_0^3}{2GM}}\left(\frac{\pi}{2} - \frac{2}{3}\left(\frac{r_a}{r_0}\right)^{3/2}\right). \tag{A.4}$$

Now, to find the relationship between dr_a and dr_0 for an infalling ring, we only need to know where a ring starting at $r_0 + dr_0$ will end up after falling for a time t_a. So, starting from Eq. (A.3),

$$(r_0 + dr_0)^{3/2} = \frac{4}{3\pi}(r_a + dr_a)^{3/2} + \frac{2}{\pi}\sqrt{2GM}t_a.$$

We then substitute Eq. (A.4) for t_a and Taylor expand the $r + dr$ terms, ultimately obtaining

$$\frac{dr_0}{dr_a} = \frac{4}{3\pi}\sqrt{\frac{r_a}{r_0}}. \tag{A.5}$$

Substituting Eq. (A.5) into our relation for Σ_a, we get

$$\Sigma_a(t) = \frac{4\Sigma_0}{3\pi}\sqrt{\frac{r_0(t)}{r_a}}. \tag{A.6}$$

Finally, we obtain the accretion rate as a function of time by substituting Eqs. (A.2) and (A.6) into Eq. (A.1) to get

$$\begin{aligned}\dot{M} &= 2\pi r_a \frac{4}{3\pi}\sqrt{\frac{r_0(t)}{r_a}}\sqrt{\frac{2GM}{r_a}} \\ &= \frac{8}{3}\sqrt{2GM}\sqrt{r_0(t)}.\end{aligned}$$

We now substitute in Eq. (A.3) for $r_0(t)$, neglecting the r_a term as being negligible compared to the time-dependent term at late times, and obtain our final relation for $\dot{M}(t)$ to be

$$\dot{M} = \frac{16}{3}\pi^{-1/3}(GM)^{2/3}t^{1/3}. \tag{A.7}$$

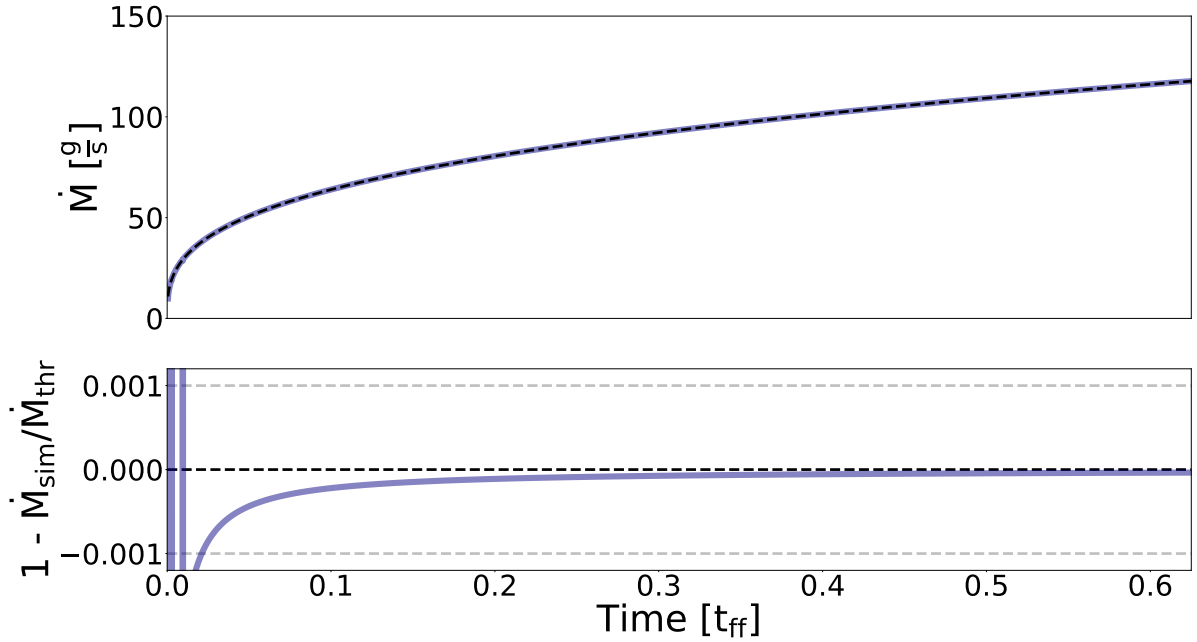


Figure A.1: *Top*: Accretion rate as a function of time. The solid purple line shows the simulation accretion rate, while the dashed black line shows the analytic profile from Eq. A.7. Time is presented in units of free-fall time from the outer boundary. *Bottom*: Residual of the accretion rate as a function of time.

In Figure A.1 we show the ratio of our simulated accretion rate to the theoretical rate predicted by Eq. (A.7). The deviations at early times are due to the assumption of $r_a \ll r_0$ not yet holding true and we run for sufficiently short times to avoid effects from the outer boundary of the simulation at late times. In the valid regime, where $r_a \ll r_0$ (corresponding to $t \gtrsim 0.1 t_{ff}$ in Figure A.1), we see that the simulated accretion rate matches the analytic solution to well within 0.1%.

A.2 Cooling of a Uniform Gas

To test our cooling routine based on the Townsend (2009) exact integration scheme (Section 2.3.1.5), we examine the temperature evolution of a gas with uniform initial surface density, Σ, uniform initial temperature, T_i, zero velocity, and no central point mass. In this way, there is no gas flow during the test, and so the only effect on the temperature will be from the radiative cooling routine.

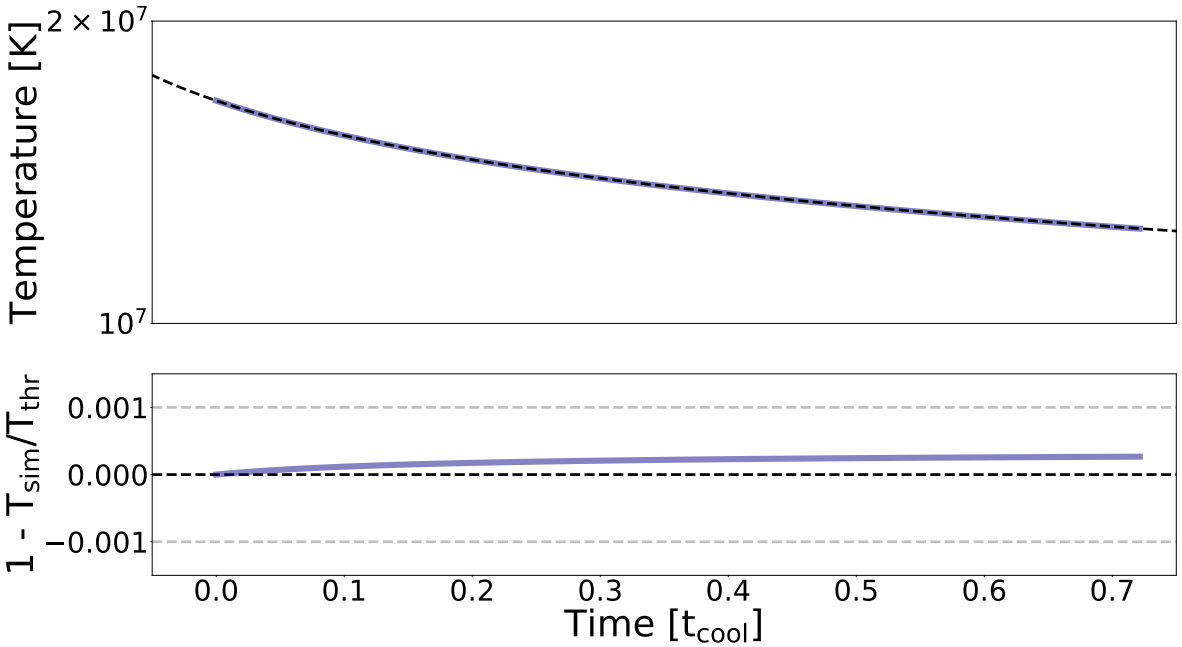


Figure A.2: *Top*: Average gas temperature as a function of time. The solid purple line shows the simulation temperature, while the dashed line shows the analytic solution from Eq. A.9. Time is presented in units of cooling time for the initial temperature. *Bottom*: Residual of the temperature as a function of time.

We explore the highest-temperature branch of the cooling routine, where

$$\Lambda(T) = 6.92 \times 10^{-35} \left(\frac{T}{1\,\mathrm{K}} \right)^{6.43} \mathrm{erg\,cm^{-2}\,s^{-1}}. \tag{A.8}$$

The analytic solution for the temperature evolution in this regime is then

$$T_f = T_i \left(1 + 5.43 \frac{t}{t_{\mathrm{cool}}} \right)^{-0.18}, \tag{A.9}$$

where $t_{\mathrm{cool}} = e_{\mathrm{int}}/\Lambda(T_i)$, with e_{int} being the internal energy of the gas per unit area.

In our test, we start with $T_i = 1.67 \times 10^7$ K and $\Sigma = 5 \times 10^6$ g cm^{-2} and evolve the simulation for several cooling times. Figure A.2 shows the comparison between the simulation output and the analytic solution. The two agree to well within 0.1%. Importantly, this agreement is maintained over a range of physical times much longer than our binary simulations are run for in the regime with the most rapid cooling.

APPENDIX B

B.1 Derivation of Disk Model used for Chapter 2

The motivation behind the disk model used in this work is to have a model which is both consistent with the equations describing a steady disk as well as intuitively tunable in regards to where gas and radiation pressure dominate in the disk. For this, we start, as indicated, from the equations for a steady disk, as presented in Frank et al. (2002):

$$\left.\begin{array}{l}
\text{a. } \rho = \Sigma/H; \\
\text{b. } H = c_s \Omega_K; \\
\text{c. } c_s^2 = P/\rho; \\
\text{d. } P = \dfrac{\rho k_B T_c}{\mu m_p} + \dfrac{4\sigma}{3c} T_c^4; \\
\text{e. } \dfrac{4\sigma T_c^4}{3\tau} = \dfrac{3GM\dot{M}}{8\pi R^3}\left[1 - \left(\dfrac{2R_g}{R}\right)^{1/2}\right]; \\
\text{f. } \tau = \Sigma \kappa_{\mathrm{R}}(\rho, T_c) = \tau(\Sigma, \rho, T_c); \\
\text{g. } \nu\Sigma = \dfrac{\dot{M}}{3\pi}\left[1 - \left(\dfrac{2R_g}{R}\right)^{1/2}\right]; \\
\text{h. } \nu = \nu(\rho, T_c, \Sigma, \alpha, ...),
\end{array}\right\}, \tag{B.1}$$

The symbols used throughout these equations are all defined in §3.3.2 of the main text.

For convenience, we introduce the convention $f \equiv [1-(2R_g/R)^{1/2}]$. We also take that our disk's kinematic viscosity is represented by a conventional α-viscosity, of the form

$$\nu = \alpha c_s H. \tag{B.2}$$

Finally, we introduce a parameterization of the scale height H, separating the contributions from gas and radiation pressures:

$$H^2 \equiv H_g^2 + H_r^2, \tag{B.3}$$

where

$$\begin{aligned} H_g^2 &\equiv \frac{P_g}{\rho\Omega_K^2}, \\ H_r^2 &\equiv \frac{P_r}{\rho\Omega_K^2}. \end{aligned} \tag{B.4}$$

and

$$\begin{aligned} P_g &= \frac{\rho k T_c}{\mu m_p}, \\ P_r &= \frac{4\sigma}{3c} T_c^4. \end{aligned} \tag{B.5}$$

Then, for H_r, we have

$$H_r^2 = \frac{4\sigma}{3c} T_c^4 \rho^{-1} \Omega_K^{-2}. \tag{B.6}$$

Then, combining this with equations (B.1e), (B.1f), and (B.1a), we obtain

$$\begin{aligned} H_r^2 &= \frac{3}{8\pi c} \kappa_{\rm R} \dot{M} H f \\ &= hH, \end{aligned} \tag{B.7}$$

where, for convenience, we have defined

$$h \equiv 3\kappa_{\rm R}\dot{M} f/(8\pi c). \tag{B.8}$$

We note here that far from the central object, where $R \gg 2R_g$, $f \approx 1$ and so, for $\kappa_{\rm R} =$ constant,

as is chosen for this work, h also goes to a constant. Further, when radiation pressure dominates, $H \approx H_r \Rightarrow H_r \approx h$. This combination of facts allows h to be interpreted as a kind of "minimum scale height" of the disk, whose value is set by the accretion rate $\dot{M}$.

Squaring both sides of equation (B.7) and recalling our definition of H in equation (B.3),

$$H_r^4 = h^2 \left(H_g^2 + H_r^2\right). \tag{B.9}$$

The only positive-valued solution for H_r from this is

$$H_r^2 = \frac{h^2}{2}\left(1 + \sqrt{1 + 4h^{-2}H_g^2}\right). \tag{B.10}$$

Following convention, we choose to parameterize H_g as a powerlaw in R,

$$H_g \equiv h\left(\frac{R}{R_c}\right)^k. \tag{B.11}$$

Since $h \approx$ constant at large R, which is where gas pressure dominates, this expression effectively prescribes H_g as a powerlaw of slope k. R_c sets the radius at which $H_g = h$. Since $H_r \approx h$ in the radiation-dominated region, R_c then determines the approximate radius where the disk transitions from radiation-dominated to gas-dominated.

Taking this expression for H_g, H_r now becomes

$$H_r^2 = \frac{h^2}{2}\left(1 + \sqrt{1 + 4\left(\frac{R}{R_c}\right)^{2k}}\right), \tag{B.12}$$

and for the total scaleheight H we obtain

$$H^2 = h^2 d\left(\frac{R}{R_c}\right), \tag{B.13}$$

where we define

$$d\left(\frac{R}{R_c}\right) \equiv \left[\left(\frac{R}{R_c}\right)^{2k} + \frac{1}{2}\left(1+\sqrt{1+4\left(\frac{R}{R_c}\right)^{2k}}\right)\right] \tag{B.14}$$

From here, we are ready to solve for the properties of our disk. We start with surface density by combining equation (B.2) with equations (B.1b) and (B.1g) to get

$$\Sigma = \frac{1}{3\pi}\alpha^{-1}\Omega_K^{-1}H^{-2}\dot{M}f. \tag{B.15}$$

We can likewise obtain an expression for the midplane temperature by combining equations (B.1e) and (B.1g),

$$T_c^4 = \frac{9G}{32\pi\sigma}M\dot{M}R^{-3}\kappa \mathrm{R}\Sigma f. \tag{B.16}$$

Then, substituting in our expression for Σ from equation (B.15),

$$T_c^4 = \frac{3G}{32\pi^2\sigma}\alpha^{-1}\kappa_{\mathrm{R}}M\dot{M}\Omega_K^{-1}H^{-2}f^2. \tag{B.17}$$

We obtain the sound speed from combining equation (B.13) with equation (B.1b),

$$c_s = \frac{3}{8\pi c}\kappa_{\mathrm{R}}\dot{M}\Omega_K d\left(\frac{R}{R_c}\right)f. \tag{B.18}$$

Finally, we choose, for convention, to recast equations (B.8), (B.15), (B.17), and (B.18) in terms of $r \equiv R/R_g$, $m \equiv M/M_\odot$, and $\dot{m} \equiv \dot{M}/\dot{M}_{\mathrm{Edd}}$. $R_g \equiv GM/c^2$ is the gravitational radius of the central object, $M_\odot$ is the mass of the Sun, and $\dot{M}_{\mathrm{Edd}} \equiv 4\pi GMm_p/(\eta\sigma_T c)$ is the Eddington accretion rate of a pure hydrogen gas onto the central object with an accretion efficiency η. Taking these definitions and also that $\Omega_K \equiv \sqrt{GM/R^3}$, we obtain

$$h \equiv \frac{3}{2}\frac{GM_\odot}{\eta c^2}m\dot{m}f, \tag{B.19}$$

$$\Sigma(r) = \frac{16}{27}\frac{m_p}{\sigma_T}\eta\alpha^{-1}\dot{m}^{-1}r^{\frac{3}{2}}\left(1-\sqrt{\frac{2}{r}}\right)^{-1}d\left(\frac{r}{r_c}\right)^{-1}, \tag{B.20}$$

$$T_c^4(r) = \frac{2c^5}{3\sigma G M_\odot} \kappa_{\rm R}^{-1} \alpha^{-1} m^{-1} r^{-3/2} d \left(\frac{r}{r_c}\right)^{-1}, \tag{B.21}$$

$$c_s(r) = \frac{3}{2} c \eta^{-1} \dot{m} r^{-3/2} \left(1 - \sqrt{\frac{2}{r}}\right)^2 d \left(\frac{r}{r_c}\right)^{1/2}, \tag{B.22}$$

where $r_c \equiv R_c/R_g$. Equations (B.19), (B.20), and (B.22) are then, respectively, the same as equations (3.5), (3.7), and (3.8) presented in the main body of this work.

APPENDIX C

C.1 An Alternative View of Our Constraints

In this appendix we present a different perspective on the constraints in Figures 4.3 and 4.4, plotted as mass ratio vs separation for a given binary mass rather than mass vs separation for a given mass ratio.

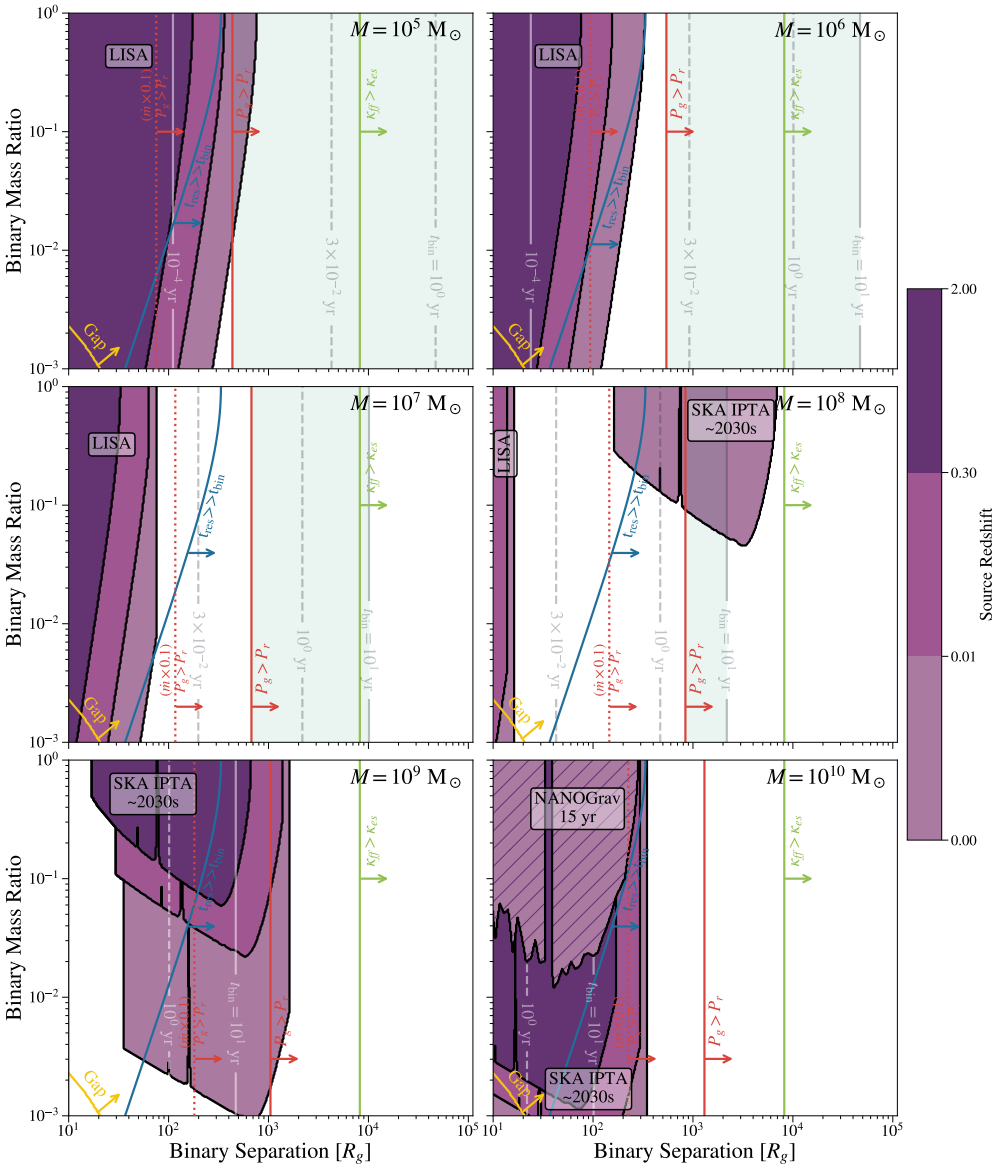


Figure C.1: The same data as in Figure 4.3, but plotted as mass ratio vs separation for example masses rather than mass vs separation for example mass ratios. The soft green highlights the region of the space which meets our criteria (i.e., the region to which gas-dominated simulations with stationary orbits are applicable). The filled purple contours show the redshift at which a given combination of binary $\{M, q, a\}$ is detectable by GW detectors. The hatched contour (visible only for $M = 10^{10}$ M$_\odot$) shows the sensitivity for the recent NANOGrav 15-year dataset at a redshift of $z = 0.01$. The red line (labeled "$P_g > P_r$") indicates the transition from radiation to gas-dominated pressure for our fiducial disk parameters, with the dotted red line showing where this transition occurs for $\dot{m} = 0.01$, which produces a more generous constraint on the applicable domain. The green line (labeled "$\kappa_{\rm ff} \gg \kappa_{\rm es}$") shows where the opacity transitions from being electron scattering-dominated to free-free absorption-dominated. The blue curve (labeled "$t_{\rm res} >> t_{\rm bin}$") marks where the binary will inspiral by $> 1\%$ of its initial separation in 10^3 orbits. The yellow line (labeled "Gap") indicates where in the disk a gap can be opened, with only very low q and low a failing to open a gap for our fiducial disk parameters. Finally, in grey, we show the binary orbital timescale for 10 years, 1 year, 2 weeks, and 1 hour, encompassing a range of reasonable monitoring cadences.

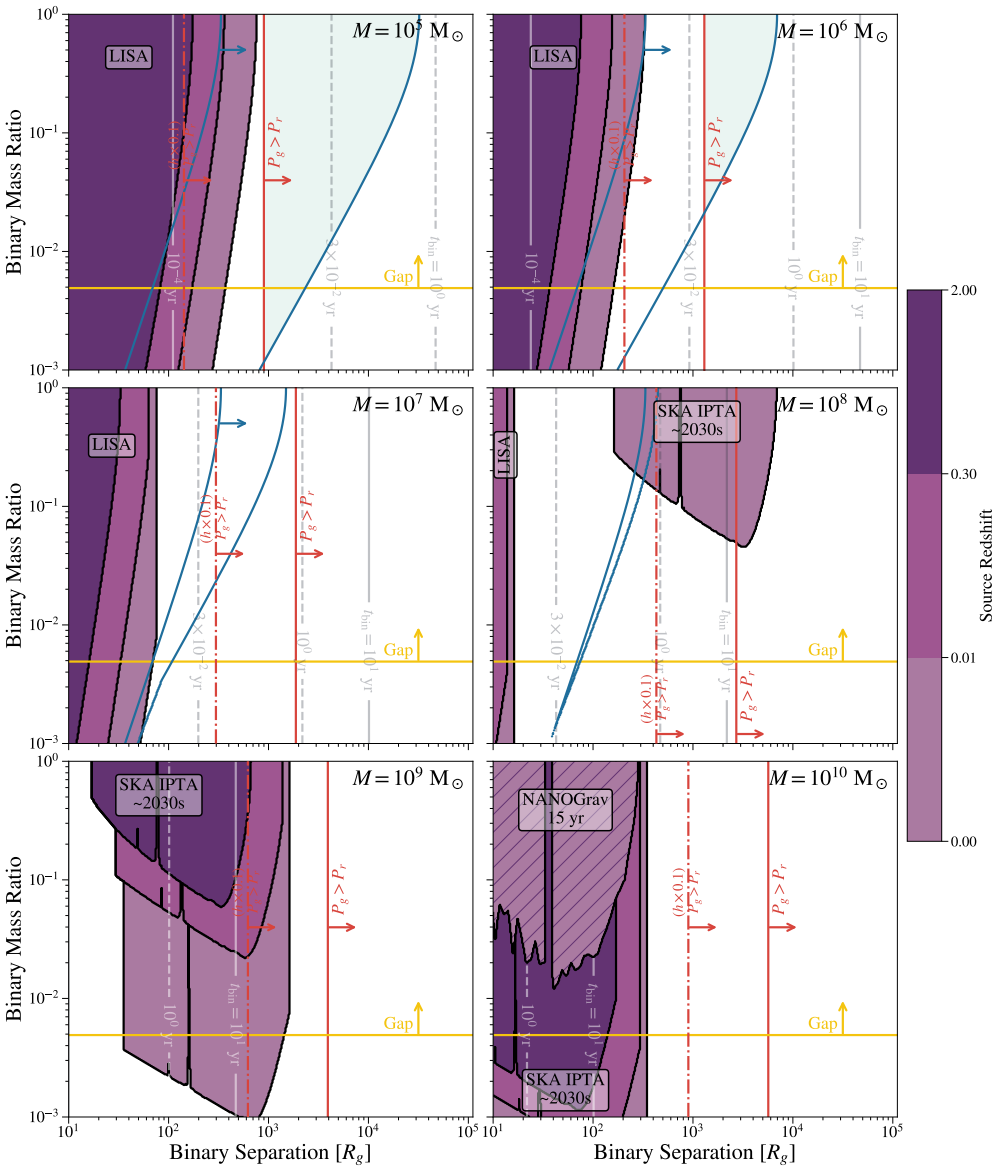


Figure C.2: The same data as in Figure 4.3, but plotted as mass ratio vs separation for example masses rather than mass vs separation for example mass ratios. The soft green highlights the region of the parameter space to which gas-dominated, stationary orbit simulations with a $h = 0.1$ disk are applicable. The filled purple contours show the redshift at which a given combination of binary $\{M, q, a\}$ is detectable by GW detectors. The hatched contour (visible only for $M = 10^{10}$ M$_\odot$) shows the sensitivity for the recent NANOGrav 15-year dataset at a redshift of $z = 0.01$. The red line (labeled "$P_g > P_r$") indicates the transition from radiation to gas-dominated pressure for the fiducial $h = 0.1$ disk model and occurs at larger radii than in the SS73-like disk model. The dash-dotted red line shows the location of the pressure transition for $h = 0.01$ instead. The blue curves (labeled "$t_{\rm res} >> t_{\rm bin}$") marks where the binary will inspiral by $> 1\%$ of its initial separation in 10^3 orbits, with the inner curve corresponding to gravitational wave inspiral and the outer curve corresponding to secondary-dominated migration, with only a narrow band of $\{q, a\}$ between the two where the binary meets our criterion for being stationary. The yellow line (labeled "Gap") indicates where in the disk a gap can be opened, with all $q \gtrsim 5 \times 10^{-3}$ being able to open a gap at any radius in the $h = 0.1$ disk. In grey, we show the binary orbital timescale for 10 years, 1 year, 2 weeks, and 1 hour, encompassing a range of reasonable monitoring cadences.

BIBLIOGRAPHY

BIBLIOGRAPHY

Afzal, A., Agazie, G., Anumarlapudi, A., et al. 2023, *ApJ*, 951, L11

Agazie, G., Anumarlapudi, A., Archibald, A. M., et al. 2023a, *ApJ*, 951, L50

—. 2023b, *ApJ*, 952, L37

—. 2023c, *ApJ*, 951, L8

Agazie, G., Alam, M. F., Anumarlapudi, A., et al. 2023d, *ApJ*, 951, L9

Amaro-Seoane, P., Audley, H., Babak, S., et al. 2017, arXiv e-prints, arXiv:1702.00786

Amaro-Seoane, P., Andrews, J., Arca Sedda, M., et al. 2023, Living Reviews in Relativity, 26, 2

Anglés-Alcázar, D., Davé, R., Faucher-Giguère, C.-A., Özel, F., & Hopkins, P. F. 2017, *MNRAS*, 464, 2840

Antoniadis, J., Arumugam, P., Arumugam, S., et al. 2023a, The second data release from the European Pulsar Timing Array IV. Search for continuous gravitational wave signals, arXiv:2306.16226

—. 2023b, The second data release from the European Pulsar Timing Array: V. Implications for massive black holes, dark matter and the early Universe, arXiv:2306.16227

Arca-Sedda, M., & Gualandris, A. 2018, *MNRAS*, 477, 4423

Arzoumanian, Z., Baker, P. T., Blecha, L., et al. 2023, arXiv e-prints, arXiv:2301.03608

Avramov, B., Berczik, P., Meiron, Y., Acharya, A., & Just, A. 2021, *A&A*, 649, A41

Bansal, K., Taylor, G. B., Peck, A. B., Zavala, R. T., & Romani, R. W. 2017, The Astrophysical Journal, 843, 14

Barnes, J. E., & Hernquist, L. 1996, *ApJ*, 471, 115

Barnes, J. E., & Hernquist, L. E. 1991, *ApJ*, 370, L65

Begelman, M. C., Blandford, R. D., & Rees, M. J. 1980, *Nature*, 287, 307

Bellovary, J., Volonteri, M., Governato, F., et al. 2011, *ApJ*, 742, 13

Benítez-Llambay, P., & Masset, F. S. 2016, *ApJS*, 223, 11

Blecha, L., Loeb, A., & Narayan, R. 2013, *MNRAS*, 429, 2594

Bortolas, E., Mapelli, M., & Spera, M. 2018, *MNRAS*, 474, 1054

Bowen, D. B., Mewes, V., Campanelli, M., et al. 2018, *ApJ*, 853, L17

Caproni, A., Abraham, Z., & Monteiro, H. 2013, *MNRAS*, 428, 280

Charisi, M., Bartos, I., Haiman, Z., et al. 2016, *MNRAS*, 463, 2145

Charisi, M., Taylor, S. R., Runnoe, J., Bogdanovic, T., & Trump, J. R. 2022, *MNRAS*, 510, 5929

Chen, Y.-C., Liu, X., Liao, W.-T., et al. 2020, *MNRAS*, 499, 2245

Chen, Y.-J., Zhai, S., Liu, J.-R., et al. 2024, *MNRAS*, 527, 12154

Cocchiararo, F., Franchini, A., Lupi, A., & Sesana, A. 2024, arXiv e-prints, arXiv:2402.05175

Combi, L., Lopez Armengol, F. G., Campanelli, M., et al. 2022, *ApJ*, 928, 187

Comerford, J. M., Gerke, B. F., Stern, D., et al. 2012, *ApJ*, 753, 42

Crida, A., Morbidelli, A., & Masset, F. 2006, *Icarus*, 181, 587

Cutler, C., Hiscock, W. A., & Larson, S. L. 2003, *Phys. Rev. D*, 67, 024015

d'Ascoli, S., Noble, S. C., Bowen, D. B., et al. 2018, *ApJ*, 865, 140

de Val-Borro, M., Edgar, R. G., Artymowicz, P., et al. 2006, *MNRAS*, 370, 529

Dempsey, A. M., Lee, W.-K., & Lithwick, Y. 2020, *ApJ*, 891, 108

Dempsey, A. M., Muñoz, D. J., & Lithwick, Y. 2021, *ApJ*, 918, L36

Derdzinski, A., D'Orazio, D., Duffell, P., Haiman, Z., & MacFadyen, A. 2021, *MNRAS*, 501, 3540

Dittmann, A. J., & Ryan, G. 2021, *ApJ*, 921, 71

—. 2022, *MNRAS*, 513, 6158

—. 2024, *ApJ*, 967, 12

Doan, A., Eracleous, M., Runnoe, J. C., et al. 2020, *MNRAS*, 491, 1104

D'Orazio, D. J., & Charisi, M. 2023, arXiv e-prints, arXiv:2310.16896

D'Orazio, D. J., & Duffell, P. C. 2021, *ApJ*, 914, L21

D'Orazio, D. J., Haiman, Z., Duffell, P., MacFadyen, A., & Farris, B. 2016, *MNRAS*, 459, 2379

D'Orazio, D. J., Haiman, Z., & MacFadyen, A. 2013, *MNRAS*, 436, 2997

D'Orazio, D. J., Haiman, Z., & Schiminovich, D. 2015, *Nature*, 525, 351

Dotti, M., Colpi, M., Haardt, F., & Mayer, L. 2007, *MNRAS*, 379, 956

Dotti, M., Rigamonti, F., Rinaldi, S., et al. 2023, *A&A*, 680, A69

Duffell, P. C. 2015, *ApJ*, 807, L11

—. 2020, *ApJ*, 889, 16

Duffell, P. C., D'Orazio, D., Derdzinski, A., et al. 2020, *ApJ*, 901, 25

Duffell, P. C., & MacFadyen, A. I. 2013, *ApJ*, 769, 41

EPTA Collaboration, InPTA Collaboration, Antoniadis, J., et al. 2023, *A&A*, 678, A50

Eracleous, M., Boroson, T. A., Halpern, J. P., & Liu, J. 2012, The Astrophysical Journal Supplement Series, 201, 23

Eracleous, M., Halpern, J. P., M. Gilbert, A., Newman, J. A., & Filippenko, A. V. 1997, *ApJ*, 490, 216

Escala, A., Larson, R. B., Coppi, P. S., & Mardones, D. 2004, *ApJ*, 607, 765

Farris, B. D., Duffell, P., MacFadyen, A. I., & Haiman, Z. 2014, *ApJ*, 783, 134

—. 2015, *MNRAS*, 446, L36

Foord, A., Gültekin, K., Nevin, R., et al. 2020, *ApJ*, 892, 29

Foord, A., Gültekin, K., Runnoe, J. C., & Koss, M. J. 2021, *ApJ*, 907, 71

Foord, A., Gültekin, K., Reynolds, M. T., et al. 2019, The Astrophysical Journal, 877, 17

Fragione, G., & Capuzzo-Dolcetta, R. 2016, *MNRAS*, 458, 2596

Fragione, G., Ginsburg, I., & Kocsis, B. 2018a, *ApJ*, 856, 92

Fragione, G., Leigh, N. W. C., Ginsburg, I., & Kocsis, B. 2018b, *ApJ*, 867, 119

Franchini, A., Lupi, A., Sesana, A., & Haiman, Z. 2023, *MNRAS*, 522, 1569

Frank, J., King, A., & Raine, D. J. 2002, Accretion Power in Astrophysics: Third Edition (Cambridge University Press), 398

Gaskell, C. M. 1996, *ApJ*, 464, L107

Goldreich, P., & Tremaine, S. 1980, *ApJ*, 241, 425

Graham, M. J., Djorgovski, S. G., Stern, D., et al. 2015a, *Nature*, 518, 74

—. 2015b, *MNRAS*, 453, 1562

Gültekin, K., & Miller, J. M. 2012, *ApJ*, 761, 90

Gutiérrez, E. M., Combi, L., Noble, S. C., et al. 2022, *ApJ*, 928, 137

Habibi, A., & Abbassi, S. 2019, *ApJ*, 887, 256

Haiman, Z., Kocsis, B., & Menou, K. 2009a, *ApJ*, 700, 1952

—. 2009b, *ApJ*, 700, 1952

Häring, N., & Rix, H.-W. 2004, *ApJ*, 604, L89

Harris, C. J., & Gültekin, K. 2024, *MNRAS*, 528, 1

Heggie, D. C. 1975, *MNRAS*, 173, 729

Hellings, R. W., & Downs, G. S. 1983, *ApJ*, 265, L39

Hickox, R. C., Mullaney, J. R., Alexander, D. M., et al. 2014, *ApJ*, 782, 9

Hobbs, G., Archibald, A., Arzoumanian, Z., et al. 2010, Classical and Quantum Gravity, 27, 084013

Hopkins, P. F., Hernquist, L., Cox, T. J., et al. 2005, *ApJ*, 630, 705

Hu, B. X., D'Orazio, D. J., Haiman, Z., et al. 2020, *MNRAS*, 495, 4061

Jahnke, K., & Macciò, A. V. 2011, *ApJ*, 734, 92

Jenet, F., Finn, L. S., Lazio, J., et al. 2009, arXiv e-prints, arXiv:0909.1058

Jiang, Y.-F., & Blaes, O. 2020, The Astrophysical Journal, 900, 25

Jiang, Y.-F., Stone, J. M., & Davis, S. W. 2013, The Astrophysical Journal, 778, 65

Johnson, B. M., & Gammie, C. F. 2003, *ApJ*, 597, 131

Ju, W., Greene, J. E., Rafikov, R. R., Bickerton, S. J., & Badenes, C. 2013, *ApJ*, 777, 44

Kaiser, A. R., & McWilliams, S. T. 2021, Classical and Quantum Gravity, 38, 055009

Kelley, L. Z. 2021, *MNRAS*, 500, 4065

Khan, F. M., Berentzen, I., Berczik, P., et al. 2012a, *ApJ*, 756, 30

Khan, F. M., Preto, M., Berczik, P., et al. 2012b, *ApJ*, 749, 147

Kippenhahn, R., & Weigert, A. 1990, Stellar Structure and Evolution (Springer Berlin, Heidelberg)

Kley, W., & Dirksen, G. 2006, *A&A*, 447, 369

Kocevski, D. D., Brightman, M., Nandra, K., et al. 2015, *ApJ*, 814, 104

Kocsis, B., Haiman, Z., & Loeb, A. 2012a, *MNRAS*, 427, 2680

—. 2012b, *MNRAS*, 427, 2680

Komossa, S., Burwitz, V., Hasinger, G., et al. 2003, The Astrophysical Journal, 582, L15

Kormendy, J., & Bender, R. 2009, *ApJ*, 691, L142

Kormendy, J., & Ho, L. C. 2013, *ARA&A*, 51, 511

Kramer, M., & Champion, D. J. 2013, Classical and Quantum Gravity, 30, 224009

Krolik, J. H. 1999, Active Galactic Nuclei: From the Central Black Hole to the Galactic Environment, Vol. 60 (Princeton University Press)

Lai, D., & Muñoz, D. J. 2023, *ARA&A*, 61, 517

Lee, K. J. 2016, in Astronomical Society of the Pacific Conference Series, Vol. 502, Frontiers in Radio Astronomy and FAST Early Sciences Symposium 2015, ed. L. Qain & D. Li, 19

Lehmer, B. D., Alexander, D. M., Bauer, F. E., et al. 2010, *ApJ*, 724, 559

Lin, D. N. C., & Papaloizou, J. 1986, *ApJ*, 309, 846

Liska, M., Hesp, C., Tchekhovskoy, A., et al. 2018, *MNRAS*, 474, L81

Liu, J., Eracleous, M., & Halpern, J. P. 2016, *ApJ*, 817, 42

Liu, T., & Vigeland, S. J. 2021, *ApJ*, 921, 178

Liu, T., Gezari, S., Heinis, S., et al. 2015, *ApJ*, 803, L16

Liu, T., Gezari, S., Ayers, M., et al. 2019, *ApJ*, 884, 36

Liu, T., Koss, M., Blecha, L., et al. 2020, *ApJ*, 896, 122

Liu, X., Guo, H., Shen, Y., Greene, J. E., & Strauss, M. A. 2018, *ApJ*, 862, 29

Lobanov, A. P., & Zensus, J. A. 2001, Science, 294, 128

Lotz, J. M., Jonsson, P., Cox, T. J., et al. 2011, *ApJ*, 742, 103

MacFadyen, A. I., & Milosavljević, M. 2008, *ApJ*, 672, 83

Magorrian, J., Tremaine, S., Richstone, D., et al. 1998, *AJ*, 115, 2285

Mangiagli, A., Caprini, C., Volonteri, M., et al. 2022, *Phys. Rev. D*, 106, 103017

Marconi, A., & Hunt, L. K. 2003, *ApJ*, 589, L21

Masset, F. 2000, *A&AS*, 141, 165

Masset, F. S. 2002, *A&A*, 387, 605

McKernan, B., Ford, K. E. S., Lyra, W., & Perets, H. B. 2012, *MNRAS*, 425, 460

Merritt, D., Milosavljević, M., Favata, M., Hughes, S. A., & Holz, D. E. 2004, *ApJ*, 607, L9

Merritt, D., & Poon, M. Y. 2004, *ApJ*, 606, 788

Milosavljević, M., & Merritt, D. 2003, *ApJ*, 596, 860

Miranda, R., Muñoz, D. J., & Lai, D. 2017, *MNRAS*, 466, 1170

Moody, M. S. L., Shi, J.-M., & Stone, J. M. 2019, *ApJ*, 875, 66

Morganti, R. 2017, Frontiers in Astronomy and Space Sciences, 4, 42

Muñoz, D. J., & Lai, D. 2016, *ApJ*, 827, 43

Muñoz, D. J., Miranda, R., & Lai, D. 2019, *ApJ*, 871, 84

Nelson, R. P., Papaloizou, J. C. B., Masset, F., & Kley, W. 2000, *MNRAS*, 318, 18

Noble, S. C., Mundim, B. C., Nakano, H., et al. 2012, *ApJ*, 755, 51

Perets, H. B., Hopman, C., & Alexander, T. 2007, *ApJ*, 656, 709

Peters, P. C. 1964, Physical Review, 136, 1224

Peters, P. C., & Mathews, J. 1963, Physical Review, 131, 435

Pringle, J. E. 1991, *MNRAS*, 248, 754

Ragusa, E., Lodato, G., & Price, D. J. 2016, *MNRAS*, 460, 1243

Rasskazov, A., Fragione, G., Leigh, N. W. C., et al. 2019, *ApJ*, 878, 17

Reardon, D. J., Zic, A., Shannon, R. M., et al. 2023a, *ApJ*, 951, L6

—. 2023b, *ApJ*, 951, L7

Richstone, D., Ajhar, E. A., Bender, R., et al. 1998, *Nature*, 395, A14

Rodriguez, C., Taylor, G. B., Zavala, R. T., et al. 2006, *ApJ*, 646, 49

Rodriguez, C., Taylor, G. B., Zavala, R. T., Pihlström, Y. M., & Peck, A. B. 2009, *ApJ*, 697, 37

Roedig, C., Krolik, J. H., & Miller, M. C. 2014, *ApJ*, 785, 115

Ross, J., Latter, H. N., & Tehranchi, M. 2017, *MNRAS*, 468, 2401

Runnoe, J. C., Eracleous, M., Pennell, A., et al. 2017, *MNRAS*, 468, 1683

Ryu, T., Perna, R., Haiman, Z., Ostriker, J. P., & Stone, N. C. 2018, *MNRAS*, 473, 3410

Saade, L., Stern, D., Brightman, M., et al. 2023, in American Astronomical Society Meeting Abstracts, Vol. 241, American Astronomical Society Meeting Abstracts, 177.31

Saade, M. L., Stern, D., Brightman, M., et al. 2020, *ApJ*, 900, 148

Sanchez, N. N., Bellovary, J. M., Holley-Bockelmann, K., et al. 2018, *ApJ*, 860, 20

Sesana, A., Haiman, Z., Kocsis, B., & Kelley, L. Z. 2018, *ApJ*, 856, 42

Sesana, A., Roedig, C., Reynolds, M. T., & Dotti, M. 2012, *MNRAS*, 420, 860

Sesana, A., Vecchio, A., & Colacino, C. N. 2008, *MNRAS*, 390, 192

Shakura, N. I., & Sunyaev, R. A. 1973, *A&A*, 24, 337

Shen, Y., Liu, X., Loeb, A., & Tremaine, S. 2013, *ApJ*, 775, 49

Shen, Y., & Loeb, A. 2010, *ApJ*, 725, 249

Siwek, M., Kelley, L. Z., & Hernquist, L. 2024, arXiv e-prints, arXiv:2403.08871

Siwek, M., Weinberger, R., Muñoz, D. J., & Hernquist, L. 2023, *MNRAS*, 518, 5059

Sobral, D., Stroe, A., Dawson, W. A., et al. 2015, *MNRAS*, 450, 630

Stone, J. M., & Norman, M. L. 1992, *ApJS*, 80, 753

Syer, D., & Clarke, C. J. 1995, *MNRAS*, 277, 758

Takahashi, R. 2017, *ApJ*, 835, 103

Tanaka, T., Menou, K., & Haiman, Z. 2012, *MNRAS*, 420, 705

Tang, Y., Haiman, Z., & MacFadyen, A. 2018, *MNRAS*, 476, 2249

Tang, Y., MacFadyen, A., & Haiman, Z. 2017, *MNRAS*, 469, 4258

Teyssandier, J., & Ogilvie, G. I. 2016, *MNRAS*, 458, 3221

—. 2017, *MNRAS*, 467, 4577

Thomas, J., Ma, C.-P., McConnell, N. J., et al. 2016, *Nature*, 532, 340

Tiede, C., Zrake, J., MacFadyen, A., & Haiman, Z. 2020, *ApJ*, 900, 43

—. 2022, *ApJ*, 932, 24

Toomre, A. 1964, *ApJ*, 139, 1217

Townsend, R. H. D. 2009, *ApJS*, 181, 391

Tremblay, S. E., Taylor, G. B., Ortiz, A. A., et al. 2016, Monthly Notices of the Royal Astronomical Society, 459, 820

Trump, J. R., Impey, C. D., Kelly, B. C., et al. 2011, *ApJ*, 733, 60

Valtonen, M. J., Lehto, H. J., Nilsson, K., et al. 2008, *Nature*, 452, 851

Valtonen, M. J., Mikkola, S., Merritt, D., et al. 2010, *ApJ*, 709, 725

Vaughan, S., Uttley, P., Markowitz, A. G., et al. 2016, *MNRAS*, 461, 3145

Volonteri, M., Haardt, F., & Madau, P. 2003, *ApJ*, 582, 559

Von Neumann, J., & Richtmyer, R. D. 1950, Journal of Applied Physics, 21, 232

Wang, H.-Y., Bai, X.-N., & Lai, D. 2023, *ApJ*, 943, 175

Wang, L., Greene, J. E., Ju, W., et al. 2017, *ApJ*, 834, 129

Westernacher-Schneider, J. R., Zrake, J., MacFadyen, A., & Haiman, Z. 2022, *Phys. Rev. D*, 106, 103010

Weston, M. E., McIntosh, D. H., Brodwin, M., et al. 2017, *MNRAS*, 464, 3882

Whitley, K., Kuznetsova, A., Gültekin, K., & Ruszkowski, M. 2024, *MNRAS*, 527, 6569

Witt, C. A., Charisi, M., Taylor, S. R., & Burke-Spolaor, S. 2022, *ApJ*, 936, 89

Wolf, C., Wisotzki, L., Borch, A., et al. 2003, *A&A*, 408, 499

Xin, C., & Haiman, Z. 2021, *MNRAS*, 506, 2408

Xu, H., Chen, S., Guo, Y., et al. 2023, Research in Astronomy and Astrophysics, 23, 075024

Zhu, Z., Nelson, R. P., Hartmann, L., Espaillat, C., & Calvet, N. 2011, *ApJ*, 729, 47

Zrake, J., Tiede, C., MacFadyen, A., & Haiman, Z. 2021, *ApJ*, 909, L13